10-17-2011 12:00 AM

Three-Dimensional Modeling of Electrostatic Precipitator Using Hybrid Finite Element - Flux Corrected Transport Technique

Niloofar Farnoosh
The University of Western Ontario

Supervisor
Kazimierz Adamiak
The University of Western Ontario Joint Supervisor
G. S. Peter Castle
The University of Western Ontario

Graduate Program in Electrical and Computer Engineering
A thesis submitted in partial fulfillment of the requirements for the degree in Doctor of Philosophy

THREE-DIMENSIONAL MODELING OF ELECTROSTATIC PRECIPITATOR USING HYBRID FINITE ELEMENT - FLUX CORRECTED TRANSPORT TECHNIQUE

(Spine title: 3-D Modeling of ESP Using Hybrid FE - FCT Technique)

(Thesis format: Monograph)

By

Niloofar Farnoosh

Graduate Program in Engineering Science
Department of Electrical and Computer Engineering

A thesis submitted in partial fulfillment
of the requirements for the degree of
Doctor of Philosophy

The School of Graduate and Postdoctoral Studies
The University of Western Ontario
London, Ontario, Canada

THE UNIVERSITY OF WESTERN ONTARIO
School of Graduate and Postdoctoral Studies

CERTIFICATE OF EXAMINATION

Co Supervisors	Examiners
Dr. Kazimierz Adamiak	Dr. Cedric Briens
Dr. G.S. Peter Castle	Dr. William D. Greason
	Dr. Glenn Harvel
	Dr. Jayshri Sabarinathan

The thesis by

Niloofar Farnoosh

entitled:

Three-Dimensional Modeling of Electrostatic Precipitator Using Hybrid Finite Element – Flux Corrected Transport Technique

is accepted in partial fulfillment of the
requirements for the degree of
Doctor of Philosophy

Date	Chair of the Thesis Examination Board

ABSTRACT

This thesis presents the results of a three-dimensional simulation of the entire precipitation process inside a single-electrode one-stage electrostatic precipitator (ESP). The model was designed to predict the motion of ions, gas and solid particles. The precipitator consists of two parallel grounded collecting plates with a corona electrode mounted at the center, parallel to the plates and excited with a high dc voltage. The complex mutual interaction between the three coexisting phenomena of electrostatic field, fluid dynamics and the particulate transport, which affect the ESP process, were taken into account in all the simulations.

The electrostatic field and ionic space charge density due to corona discharge were computed by numerically solving Poisson and current continuity equations, using a hybrid Finite Element (FEM) - Flux Corrected Transport (FCT) method. The detailed numerical approach and simulation procedure is discussed and applied throughout the thesis. Calculations of the gas flow were carried out by solving the Reynolds-averaged Navier-Stokes equations using the commercial FLUENT 6.2 software, which is based on the Finite Volume Method (FVM). The turbulence effect was included by using the k-ε model included in FLUENT. An additional source term was added to the gas flow equation to include the effect of the electric field, obtained by solving a coupled system of the electric field and charge transport equations, using the User-Defined-Function (UDF) feature of FLUENT. The particle phase was simulated using a Lagrangian-type Discrete Random Walk (DRW) model, where a large number of particles charged by combined field and diffusion charging mechanisms was traced with their motion affected by electrostatic and aerodynamic forces in turbulent flow using the Discrete Phase Model (DPM) and programming UDFs in FLUENT.

The airflow patterns under the influence of electrohydrodynamic (EHD) secondary flow and external flows, particle charging and deposition along the channel, and ESP performance in removal of submicron particulates were compared for smooth and spiked discharge electrode configurations in the parallel plate precipitator assuming various particle concentrations at the inlet. Finally, a laboratory scale wire-cylinder ESP to collect conductive submicron diesel particles was modeled. The influence of different inlet gas velocities and excitation voltages on the particle migration velocity and precipitation performance were

investigated. In some cases, the simulation results were compared with the existing experimental data published in literature.

Keywords: Electrostatic precipitator, corona discharge, electrohydrodynamics, numerical simulation, spiked corona electrode, submicron particle collection, particle charging, particle transport and deposition, particle charge-to-mass ratio, poly-dispersed particles, diesel exhaust particulates, wire-cylindrical ESP, precipitation performance, particle migration velocity.

ACKNOWLEDGEMENTS

I am appreciably grateful to Prof. K. Adamiak, my co-advisor, for his endless support and academic guidance that helped me to achieve my research goals. I would also like to express my deepest appreciation to Prof G.S.P. Castle, my advisor, for his instructive advices and also his support and encouragement during this research. I could not have made it through my studies without their encouragement and guidance. I could not have asked for more from them and they will always be my advisors. I gratefully acknowledge Dr. J. S. Chang and P. Atten for their kind consultation and helpful comments; I wish to thank my other thesis committee members: Dr. C. Briens, Dr. W. D. Greason, Dr. G. Harvel and Dr. J. Sabarinathan. I also would like to acknowledge the Natural Sciences and Engineering Research Council of Canada (NSERC) for providing grants to this study and the Shared Hierarchical Academic Research Computing Network (SHARCNET: www.sharcnet.ca) and Compute/Calcul Canada for providing facilities to make this work possible. I would like to thank Mr. B. Saunders and Mr. T. Hunt for their help with the Linux operating system and the FLUENT software. I also want to thank my officemates N. Toljic and R. Hossain for their assistance and friendship who made my life enjoyable.

Finally, I am grateful to my very kind husband, Ehsan, for his unconditional love and unending support. Special thanks are extended to my lovely family in Iran, my dear mother Nasrin, my dear father Mohammad, my beautiful sister Leila, and my wonderful brothers Ali and Amir.

TABLE OF CONTENTS

LIST OF FIGURES

LIST OF TABLES

NOMENCLATURE

Symbol	Description	Units
A_c	Effective collecting area	[m^2]
A_{face}	Area of cell face	[m^2]
a_1, a_2, a_3	Model constants	
b_1, b_2, b_3	Model constants	
c_0, c^*	Particle mass flow rate reference value	[kg/s]
$C_{1\varepsilon}, C_{2\varepsilon}, C_\mu$	Model constants	
C_c	Cunningham slip correction factor	
C_D	Drag coefficient	
D	Ion diffusion coefficient	[m^2/s]
D_e	Deutsch number	
$D_{Accumulation}$	Increasing rate of particle accumulation depth	[m/s]
d_p	Particle diameter	[m]
$\vec{E}$	Electric field	[V/m]
E_p	Peek' corona onset field	[V/m]
$\vec{E}_{ps}$	Pseudo-homogeneous electric field strength	[V/m]
$\vec{E}_{CE}$	Electric field vector near the collecting wall	[V/m]
Ehd	Electrohydrodynamic (EHD) number	
e	Electron charge (1.6×10^{-19})	[C]
e_{norm}	Model constant	
$\vec{F}$	Force field vector	[N/m^3]

F_D	Drag force coefficient	[1/s]
$\vec{F}_s$	Viscosity force	[N]
$\vec{F}_x$	External acceleration (force/unit particle mass)	[m/s^2]
$\vec{g}$	Gravitational acceleration	[m/s^2]
I	Turbulence intensity	
I_0	Corona discharge current	[A]
$\vec{J}$	Current density vector	[A/m^2]
K	Mobility of ions at actual conditions	[m^2/V.s]
K_0	Mobility of ions at atmospheric conditions	[m^2/V.s]
K_n	Knudsen number	
K_p	Particle mean mobility	[m^2/V.s]
k	Turbulence kinetic energy	[J]
k_B	Boltzmann's coefficient (1.38066×10^{-23} J/K)	[J/K]
L	Channel length	[m]
$\dot{m}_p$	Particle mass flow rate	[kg/s]
$M_{in}(d_p)$	Total mass of each particle size at the inlet	[kg]
$M_{out}(d_p)$	Total mass of each particle size at the inlet	[kg]
M_{in}	Total masses of all particle sizes at the inlet	[kg]
M_{out}	Total masses of all particle sizes at the outlet	[kg]
m_P	Particle mass	[kg]
P	Actual pressure	[Pa]
P_0	Atmospheric pressure (1.013×10^5 Pa)	[Pa]
Q	Exhaust gas flow rate	[m^3/s]

Q_P	Particle charge	[C]
Q_s	Saturation charge	[C]
$R_{Accumulation}$	Particle accumulation rate	[kg/m^2.s]
Re	Reynolds number	
R_{NE}	Distance between corona electrode and collecting surface	[m]
r_0	Radius of corona wire	[m]
r_1	Tube radius	[m]
s	Surface area of sphere	[m^2]
S	Actual surface area of the particle	[m^2]
S_{Mx}	Mass source term of x-momentum	[kg]
S_{My}	Mass source term of y-momentum	[kg]
S_{Mz}	Mass source terms of z-momentum	[kg]
SCA	Specific collection area	[m^2.s/m^3]
T_0	Atmospheric temperature (300 K)	[K]
T	Actual temperature	[K]
t	Time	[s]
u_0	Initial velocity of exhaust gas at inlet	[m/s]
$\vec{u}$	Gas velocity vector	[m/s]
$\vec{u}_P$	Particles velocity	[m/s]
$\overline{u}_i$	Mean velocity component	[m/s]
u'_i	Fluctuating velocity component	[m/s]
U	Mean velocity magnitude of the flow	[m/s]
α	Model constant	
β	Empirical coefficient	

δ	Model constant	
Φ	Electric potential	[V/m]
Φ_o	Electric potential on corona electrode	[V/m]
ϕ	Scalar	
ε	Turbulence dissipation rate	[W]
ε_0	Permittivity of vacuum/air	[F/m]
ε_r	Particle dielectric constant	
ρ_i	Ionic space charge density	[C/m^3]
ρ_f	Gas density	[kg/m^3]
ρ_p	Particle density	[kg/m^3]
ρ_0	Ionic charge density on the corona electrode surface	[C/m^3]
ρ_{DPM}	Particle charge density	[C/m^3]
μ	Airflow viscosity	[kg/m.s]
μ_t	Turbulent (or eddy) viscosity	[kg/m.s]
σ	Gas accommodation	
σ_ε, σ_k	Model constants	
λ	Molecular mean free path at actual conditions	[m]
λ_0	Molecular mean free path at atmospheric conditions	[m]
χ	Shape factor	
τ_q	Charging time constant	[s]
η_f	Grade or fractional efficiency	
η_t	Total mass collection efficiency	
ϖ_{th}	Theoretical migration velocity	[m/s]

ϖ_e	Effective migration velocity	[m/s]

ABBREVIATIONS

ac	Alternating Current
BEM	Boundary Element Method
CSM	Charge Simulation Method
CFD	Computational Fluid Dynamic
DBD	Dielectric Discharge Barrier
DCM	Donor Cell Method
dc	Direct Current
DNS	Direct Numerical Simulation
DOC	Diesel Oxidation Catalyst
DPF	Diesel Particulate Filter
DPM	Discrete Phase Model
DRW	Discrete Random Walk
EHD	Electrohydrodynamic
ESP	Electrostatic Precipitator
FCT	Flux Corrected Transport
FDTD	Finite Difference Time Domain
FEM	Finite Element Method
FVM	Finite Volume Method
LDV	Laser Doppler Velocimetry
MoC	Method of Characteristics
NPR	Nonthermal Plasma Reactor
PIV	Particle Image Velocimetry
RANS	Reynolds-averaged Navier-Stokes

Re	Reynolds number
RMS	Root Mean Square
SIMPLE	Semi-Implicit Method for Pressure Linked Equations
SOF	Soluble Organic Fraction
SOR	Successive Over Relaxation
UDF	User Defined Function
wESP	Wet Electrostatic Precipitator

1. INTRODUCTION AND OBJECTIVES

1.1 Introduction

Electrostatic precipitation (ESP) has been an important industrial technology since the early 1900s and can be regarded as the major air pollution control device in industrial applications such as purifying the flue gases from coal burning or cement production plants and diesel engine generators. In this device, the particles are charged by the ionic bombardment in the precipitator channel, transported towards the collecting plates by the electric forces and deposited on them. The electrostatic forces exerted on the ionic space charge by the electric field (Coulomb forces) induce the secondary electrohydrodynamic (EHD) flow, or the ionic wind, which increases the flow turbulence in the channel. The airflow drag forces and EHD flow also affect the particle trajectories, making them even more difficult to predict. Therefore, the complex coupled phenomena between the electric field, turbulent flow field, and particle charging and motion must be taken into account for the full analysis of ESPs [1,2].

Although most of the basic phenomena related to particle collection in an ESP are well understood, extensive numerical and experimental investigations are still being carried out on many detailed aspects of ESP, such as electrostatics fields, fluid dynamics, charging mechanism and particle dynamics.

1.2 Research objectives

1.2.1 Developing a reliable numerical algorithm to evaluate the electrical characteristics inside an ESP

Numerous studies have been devoted to the numerical modeling of the complex and coupled physical phenomena involved in the precipitation process but none of them could exactly model the entire process [3-6]. Numerical analysis has been widely preferred due to the high cost of experimental set up. Detailed, reliable and complex three-dimensional numerical modelling of the electric and flow field is still a challenge for the full scale ESP geometry; therefore, mostly simplified ESP channel geometries have been assumed in theoretical, numerical or experimental ESP studies.

For modeling the corona discharge in ESPs, many authors considered a quite simplistic model assuming uniform charge distribution along the smooth discharge electrode [7,8]. Although positive corona discharge creates a uniform sheath around the electrode, in the case of negative corona discharge discrete spots, called tufts, are generated along the electrode resulting in a non-uniform charge distribution [9,10].

In this phase of the project, a hybrid Finite Element (FEM)-Flux Corrected Transport (FCT) method was proposed to obtain electrical characteristics, including the distributions of the electric field, the electric potential and the ionic space charge density inside a one-stage single electrode ESP, assuming positive or negative corona discharge along the corona electrode. The Navier-Stokes equations for airflow were solved using the commercial FLUENT software, based on Finite Volume Method (FVM), with the aid of User-Defined-Functions (UDFs) to obtain the airflow patterns modified by EHD secondary flow produced by the corona discharge.

1.2.2 Investigating 3-D EHD flow and its effect on ESP performance

The secondary EHD flow is generated due to momentum transfer from moving charged species (ions and particles) to neutral gas molecules. The flow interaction between EHD secondary flow and primary flow is quite different for negative and positive corona leading to different patterns in flow structure [9-13]. In addition to the primary flow and electric field, the EHD flow pattern also depends on the particle properties such as particle size and concentration [7, 8, 14, 15]. Because of the complex stochastic nature of this flow, many contradictory conclusions on its influence on particle collection efficiency are reported in literature. Some researchers believe that the particle collection efficiency could be significantly improved if the EHD flows were eliminated [16]. In 2000, Soldati showed that the superposition of EHD flows onto the turbulent channel flow significantly modifies the turbulent structure in the wall region resulting in drag reduction, which changes the local behavior of particles to be collected by an ESP [17]. He also pointed out that EHD flow not only contributes to re-entrainment of particles to the central region of the channel, but also to sweeping the particles to the collecting walls, thus having negligible influence on the overall collection efficiency.

In this thesis, once the ionic charge distribution and electric field distributions were obtained from the numerical simulations, the 3-D corona induced EHD secondary flow patterns were obtained for different corona discharge electrode configurations, assuming uniform corona discharge on smooth wire electrode or non-uniform corona discharge in spiked flat electrode. The effects of different electrode geometries, inlet velocities and excitation voltages on EHD flow patterns and consequently, particle trajectories and precipitation performance were also investigated.

1.2.3 Investigating particle concentration effect on ESP performance

Many authors used mathematical and experimental techniques to investigate the effect of various particle concentrations on EHD flow patterns, corona discharge current, particle trajectory and deposition in the ESP channel for different ESP configurations [18-20]. In 2009, Adamiak and Atten examined this effect on a single wire-plate ESP and demonstrated that the flow pattern is modified by the secondary EHD flow which strongly depends on the particle concentration [21].

In this phase of the project, the influence of various particle concentrations on precipitator performance was numerically evaluated for different corona electrode geometries in the ESP assuming mono-dispersed and poly-disperse particle distributions and the results were compared with the experimental data presented in [20]. It was shown that by increasing the particle concentration at the inlet, the corona discharge current is suppressed resulting in electrostatic force reduction on the particles, thus decreasing the precipitation performance.

1.2.4 Investigating the effect of discharge electrode geometry on EHD flow patterns and ESP performance in removal of fine particles

The particle mass collection efficiency of modern industrial wire-plate ESPs is of the order of 99%. However, due to changes in particle emission standards, improving the collection of sub-micron to micron diameter particles is still necessary and is a challenging problem.

A good understanding of the complex mechanisms involved in the precipitation process and different parameters affecting particle deposition such as particle size, charge-to-mass ratio, migration velocity, electrical parameters and operating conditions, are crucial to obtain the best design for achieving the required collection efficiency [22,23]. Experimental determination of these characteristics is usually expensive in terms of both time and money, and numerical simulations of this process begin to dominate. Among numerous papers on ESP, only some deal with using 3-D computational methods for modeling the electrostatic process with real geometry of discharge electrodes.

Discharge electrode design has also been a prominent factor in submicron particle removal. The rigid type discharge electrodes with spikes parallel to the collecting electrodes have been investigated by few authors. In [24], D. Brocilo *et al.* estimated the electric field and ion density distribution in a spike electrode precipitator and investigated the effect of smooth and spiked electrode geometry on removal of submicron particles. J. Podlinski *et al.* [25,26] have shown that in a spiked electrode geometry, the negative corona discharge is more efficient than positive corona discharge for collecting submicron particles by injecting higher amount of ionic charges to the channel.

In this phase of the project, ESPs with different corona discharge electrode geometries were simulated including smooth wire and spiked flat electrodes with spikes alternatively located on both sides of the electrode or located only on one side of the electrode either on upstream or downstream direction of the channel. The effect of discharge electrode geometry on EHD flow patterns and precipitation performance was evaluated and in some cases the results were compared with the existing experimental data. It was shown that the discharge electrode with spikes on two sides is more effective for collecting submicron particles in the range of 0.25-1.5 μm.

1.2.5 Modeling a wire-cylinder ESP for collecting submicron diesel particulates

For an equivalent mechanical power, diesel engines are energetically more efficient than gasoline engines. However, diesel exhaust particulates are considered one of the largest sources for particulate emissions in urban areas. These particles are composed of a carbonaceous solid core and toxic organic compounds on their surfaces adsorbed during the combustion process, which is hazardous for human health and the environment. With the aid of advanced technologies, the particle mass emission can be effectively reduced in modern diesel engines. However, the number of ultrafine particles (diameter below 100 nm) emitted, is increased. These can penetrate lung tissues more deeply and have greater toxicity than larger particles. In recent years, special environmental concerns are directed towards controlling the emission of ultrafine particles.

A search for an effective control of diesel particulate emissions has been a topic of interest for decades. Several techniques have been proposed for reducing diesel exhaust emissions, namely engine modification, fuel additives, alternative fuels, and after-treatment systems. Nevertheless, the first three techniques cannot effectively reduce diesel particulate emissions down to a level in compliance with standards being increasingly stringent. The after-treatment systems are of particular interest because they can achieve satisfactory removal efficiency of the diesel pollutants. Currently, the after-treatment technologies are restricted to diesel oxidation catalysts (DOCs), diesel particulate filters (DPFs), and nonthermal plasma reactors (NPRs), such as ESPs and dielectric discharge barriers (DBDs).

In this phase of the project, a laboratory scale wire-tube ESP used in Fuji Heavy Industries Ltd. was simulated and the precipitation performance for the effective control of diesel emissions was evaluated. The ESP has been subjected to the following investigations:

- Development of the particle collection model for a more effective prediction of the ESP collection efficiency as a function of particle size,
- Effects of engine loads and gas residence time on collection efficiency of ESP,
- Different channel length effect on precipitation performance,
- Different excitation voltage and inlet velocity effect on particle migration velocity,
- Comparison of the measured particle collection efficiency with the model predictions obtained from the developed model.

2. LITERATURE REVIEW

2.1 Numerical modeling of electric corona discharge in ESP

During the last several decades, many efforts have been made to achieve a better understanding of all important phenomena involved in the precipitation process, and many numerical techniques have been proposed in the literature for solving the governing equations. Some authors focused their studies on two-dimensional analysis of electrical conditions only, considering the electrical forces as a primary mechanism affecting the particle trajectories [14, 15]. Various numerical techniques have been used: FEM-Method of Characteristics (MoC) [3, 6], FEM-Boundary Element (BEM)-MoC [8], FEM-Charge Simulation (CSM) [4], FEM-Donor Cell (DCM) [27] and Finite Difference (FDM)-MoC [28]. These methodologies were applied to obtain the electric field and charge density distributions, and *V-I* characteristics of corona discharge in a 2-D ESP model. Only a few authors focused on 3-D analysis of corona discharge in ESPs [9,10,29,30]. In most cases the results were compared with the related experimental data from the literature. However, memory requirements, computation speed and accuracy of the results were quite different for each numerical technique. Moreover, the so-called single species corona model was commonly accepted, where the ionization reactions and ionization layer were neglected and steady flow of a single dominant ion was assumed. While this substantially simplified calculations, it required additional information about the amount of generated ions. The most common approaches relied either on the experimental value of the total corona current, or on the semi-empirical Peek's law.

2.2 EHD secondary flow and its effect on precipitation performance - Numerical modeling and experimental studies

Various 2-D numerical techniques were used for predicting the EHD flow patterns assuming two air flow models: laminar and turbulent. In 2007, Chun *et al.* [7] obtained a 2-D EHD flow pattern for the Chen-Kim k-ε turbulent flow model in a wire-plate ESP using an algorithm they referred to as SIMPLEST, along with CFD software. In 2008, Zhao and Adamiak used a 2-D MoC-FEM-BEM hybrid numerical algorithm along with FLUENT software to generate a complete air flow regime map for different EHD and Reynolds (Re) numbers in a wire-plate ESP considering the laminar air flow model [8]. They identified at least eight different flow patterns possible for different external flow and wire voltage levels. Similar studies were also performed to obtain EHD flow patterns in multi-wire ESPs. Kallio and Stock [14] implemented a 2-D FEM-FDM algorithm for modeling a multi-wire ESP to obtain EHD flow patterns assuming the *k-ε* turbulent flow model. The numerical results were verified experimentally using Laser Doppler Velocimetry (LDV). In 2002, a 2-D FEM-FVM numerical method along with a perturbation analysis of 2-D Euler equations was performed by Schmid *et al.* for modeling a multi corona wire ESP model [15]. The influence of different flow models: turbulent (*k-ε* and Reynolds stress-model) and non-turbulent (Euler and laminar) were investigated. A detailed review of important mechanisms leading to formation of the secondary flows was also demonstrated.

Due to deficiencies of the 2-D approaches in the accurate modeling of a finite length corona wire and 3-D characteristics of the EHD flow patterns, some authors tried to develop 3-D computational algorithms for modeling the ESP problems, considering different corona electrode configurations. In 1996 Davidson *et al.* [29] applied a 3-D FEM-MoC technique to obtain electrical conditions inside an ESP, including current density distribution and electric fields in point-to-plane and barbed plate-to–plane ESP. A reasonably exact model for computing the charge distribution on the corona electrode surface was assumed and it was based on Peek's formula. Although these numerical results had a good accuracy, the authors never tried to investigate the EHD flow pattern generated in the same configuration.

Different model complexities have been reported in the literature for investigating the EHD effects in an ESP. The geometry of the discharge electrodes plays a significant role on determining the electrical and aerodynamic characteristics of the system. The vast majority of the published studies considered the simplified case of a homogeneous discharge along smooth wire electrodes and only in a few publications were more complicated electrode configurations assumed, such as tuft or spiked-type corona electrode [9,18], barbed plate [29] and barbed wire-electrodes [31]. In these cases the corona discharge is localized at some points along the corona wire and the charge density distribution near the corona electrode is strongly non-uniform. In practical applications, in negative corona discharge isolated tufts with unstable intensity and location are generated along the corona electrode. Commercial electrodes, such as barbed wire electrodes, plane strip electrodes and studded tube electrodes, are conventionally designed to predetermine the location of tufts and to achieve steady equally spaced corona tufts. The gas flow, electrical conditions and particle transport become essentially 3-D in these configurations.

The numerical study of Yamamoto and his co-workers related to multiple-tuft wire discharges indicated that each tuft point creates a pair of donut shaped rings of airflow [9], which are more organized in a laminar flow than in a turbulent one [10]. They also pointed out that a transition from the well organized spiral motion to the complete mixing regime depends on the tuft and wire-to-plate spacing. The tuft-corona discharge also substantially increases the turbulence level. It was shown [9] that by increasing the applied voltage the number of tufts along the wire increases, they become more stable and more uniformly distributed. In [10], a 3-D FDM numerical technique (SIMPLEST algorithm) was used for modeling a multi-wire ESP. In this model, point corona electrodes were assumed to take into account the effect of negative corona discharge, which forms tufts. Using a simplistic corona model, 3-D EHD flow and electric patterns (distribution of airflow and electrostatic parameters) were obtained for both turbulent and laminar flow models. They also implemented finite difference approximation using the successive-over-relaxation (SOR) method for modeling spike electrodes in a multi-wire industrial ESP configuration to obtain 3-D EHD flow patterns considering the turbulent flow model [30]. In their model the spikes were alternatively located along the corona wire and pointed towards the ground planes. They reported a zig-zag motion generated in the direction of the main flow, which changed to spiral rings for the higher applied voltages. According to these simulations, the secondary flow distribution without the external gas flow consists of a pair of long-elliptic and circulatory cells between spiked points along the wire, which changes to a pair of long-elliptic spiral flows in the direction of the gas flow between ground planes after adding the primary flow into the model. An experimental set-up was previously employed by the same authors in [18] for demonstrating particle trajectories and investigating the effect of particle concentration on the *V-I* characteristic curve in a spiked electrode discharge electrode and convex-concave-type collecting electrode.

Many visual observations and velocity measurements devices, including LDV, Particle Image Velocimetry (PIV) and hot wire anemometers were used by many authors to experimentally visualize the flow patterns and measure the velocities of the EHD flows [14, 32- 37]. In [38], Larsen and Christensen examined the EHD flow pattern in a small scale barbed-wire precipitator using LDV measurements. According to these results, each discharge point along the corona wire creates a pair of highly structured recirculation vortices and the barb spacing determines the EHD flow structure. Davidson and McKinney [39] used hot-film anemometry measurements to characterize the EHD flow in a barbed plate-to-plate precipitator. They proposed the barbed plate electrode as a useful design which effectively reduces the scale of corona induced EHD flow and thus decreases particle mixing. However, greater turbulence was generated in this precipitator than in a conventional wire-plate precipitator. More recently, 3-D PIV measurements were carried out by Mizeraczyk *et al.* to study the EHD flow patterns and particle trajectories in various ESP configurations assuming different channel widths [40], corona electrode orientations [41] and smooth plate or flocking plane collecting electrodes (two stainless-steel plane meshes covered with nylon flocks) with the corona wire electrode located along the gas flow, where the lower flow velocity near the flocking plane electrodes prevented the re-entrainment of the deposited particles and increased the collection efficiency of fine particles up to 94% [42]. In [25], they investigated the secondary EHD flow and particle collection efficiency for submicron dust particles (0.25-1.5 μm) in a spike-plate ESP under negative and positive dc voltage using 3-D PIV measurements. Their experimental results demonstrated a complex turbulent flow with a structure depending on the applied voltage level and the position of measuring plane with respect to the spike tips. They concluded that the flow in the spike-plate ESP has a strong 3-D variation. Velocity measurements showed that the turbulence intensity, generated when a negative voltage is applied to the corona wire, is higher than for the case of positive voltage. However, no comprehensive investigations for EHD secondary flow field in ESPs with spike discharge electrode could be found in literature.

Some processes occurring in an ESP are not yet fully understood, particularly those concerning the turbulent EHD flow effect on particle transport and deposition and has been debated in the past. Many contradictory conclusions are reported due to the very complex nature of this flow. Some believe that the collection efficiency could be improved if the EHD flows were eliminated [16]. Contrary to that, Soldati concluded that the EHD flow have negligible influence on the overall collection efficiency [17].

2.3 Particle charging, motion and collection efficiency in ESPs - Numerical modeling and experimental studies

One of the main concerns in numerical modeling is also how to model the particle charging process. A. Mizuno [43] confirmed that for particles greater than 2 μm field charging is dominant and for particles less than 0.2 μm diffusion charging becomes more important. In [44], H. Lei *et al.* proved that the movement of particles with sizes in the range of 0.5 to 5 μm are very sensitive to the gas turbulence and both diffusion and field charging, which makes the particle trajectory and charging much more complicated. Recently, Z. Long and Q. Yao compared the accuracy and computational time for various particle charging models including field charging, diffusion charging and combined field-diffusion theories [45]. They evaluated the accuracy of nine particle charging models based on the existing experimental results in the same condition and concluded that the Lawless field-diffusion combined model [46] is the best choice for numerical modeling of particle dynamics in ESPs.

The effect of turbulence on particle motion in precipitators was investigated by many authors, who used various analysis techniques; the two main ones were the Eulerian approach and the Lagrangian, or particle-tracking, approach. Even though some investigators used the Eulerian approach to predict the ESP operation [47,48], others believed that this calculation method has some deficiencies when it is applied to a single-stage ESP, because the charge acquired on a particle in a non-uniform electric field is determined by the actual, not mean, path the particle traverses. In 2000, Soldati [17] used Direct Numerical Simulation (DNS) to analyze the effects of EHD flow and turbulence on 2-D pre-charged particle transport and collection efficiency in a multi-wire ESP. Using a Lagrangian approach, the particle collection efficiency for particles of different sizes was compared in two cases: with and without EHD flow. According to his investigations, EHD flow has negligible influence on the overall particle collection and on particle deposition at the walls. Schmid and Vogel developed a model in which a Lagrangian continuous random walk model was compared with the Eulerian approach for a number of test cases; the strong coupling between the fluid flow and the electric field was extensively examined [49]. Schmid pointed out that even though the Lagrangian particle tracking is still superior in terms of physical modeling of EHD particulate flows, the Eulerian approach may lead to reasonable results with substantially reduced numerical effort [50]. In [19], Skodras *et al.* made a similar comparison between the two approaches, Eulerian and Lagrangian, showing that the Lagrangian approach is superior, and confirmed the significant turbulence effect on the electric field. In their study, particle trajectories and collection efficiency were computed in a multi–wire ESP using 2-D commercial fluid dynamics software considering a turbulent flow model. Effects of particle diameter, inlet velocity and applied voltage on particle collection efficiency were investigated. Goo and Lee applied the Lagrangian particle tracking method coupled with the 2-D Monte-Carlo method for simulating particle motion in turbulent flow fields [51]. Afterwards, Lei *et al.* used the same technique to simulate particle charging and motion in a 3-D multi-wire ESP model. Turbulent particle charging and tracing for a range of particle diameters were computed using a Lagrangian approach. As a result, 2-D EHD flow patterns were demonstrated for the turbulent flow model. The variation of different forces acting on particles of different sizes along their trajectories was investigated in detail as well, concluding that the electric field and drag forces are the key forces in ESP. The authors pointed out that the 3-D numerical simulation is necessary not only to investigate the EHD flow, but also to evaluate different types of forces on the particle's movement.

Some authors used different experimental techniques to demonstrate particle motion and deposition in ESPs. Mizeraczyk and his collaborators used 2-D PIV measurements to investigate the effect of various dust concentrations on EHD flow patterns for a laminar flow model in a multi–wire ESP [20]. The results of 3-D PIV measurements of EHD flow patterns in a narrow wire-duct ESP for two wire positions: longitudinal and transverse-to-flow were investigated. The particle collection efficiency for a range of particle diameters, and negative and positive applied voltages in ESP with spike-type electrode were also presented by the same authors in [25, 41]. According to their visualizations, the flow patterns in both ESPs (with longitudinal or transverse wire electrode) are very complicated and the particle trajectories in the narrow ESP exhibit a strongly 3-D character due to the narrow cross section of the ESP duct. These experimental results also confirmed the very well known fact that decreasing the particle diameter and applied voltage results in decreasing particle collection efficiency.

In addition to the mono-dispersed particle analysis, some authors investigated trajectories and collection of poly-dispersed particles in ESP. In 1998, Lu and Haung proposed a sectional model approximating the continuous particle size distribution to study the performance of a wire-plate precipitator for collecting poly-dispersed particles. The continuous evolution of particle size distribution along the precipitator and its effect on the ESP performance were quantitatively determined. The model performance was validated by comparing its predictions with the existing experimental data in literature [52]. Kim and Lee designed and built a laboratory-scale eight wire single-stage ESP operating in a wind tunnel for simulating poly-dispersed aerosols [53]. They pointed out that the size distribution of most poly-dispersed aerosols is very close to the lognormal distribution. Later, the same authors developed a modified moment-lognormal model to predict the continuous change of particle size distribution for considering the flow convection, electrostatic force and particle diffusion process in a wire-plate ESP [54]. Their proposed model could predict both the overall mass and number efficiencies of poly-dispersed particles without computing the fractional efficiency of each size regime. The effects of lognormal particle size distribution parameters such as the geometric mean particle radius and standard deviation on the ESP performance were examined and quantitatively determined.

Recently, poly-dispersed particle transport in ESP has also been studied experimentally. In [55], Nobregal *et al.* evaluated the performance of a wire-plate ESP in the removal of particles with a wide range of diameters and investigated the effect of channel width on precipitator performance. Improvement in particle removal for wider precipitators, but also larger energy consumption, has been shown. In [56], Ivancsy and Suda considered a special case of poly-dispersed dust load particles, with the same diameter and different relative permittivities. Mizeraczyk and his collaborators carried out PIV measurements to obtain the dust-particle flow velocity patterns for various densities of submicron dust, in which the particle size distribution had a maximum at a particle diameter of 0.4 μm [20]. According to their results, increasing the dust density not only significantly modifies the mean flow pattern (which is the effect of EHD secondary flow), but also increases the flow turbulence in the downstream ESP region and decreases the average discharge current.

Particle charge effect on precipitation performance is investigated by a few authors. In [57], Choi and Fletcher predicted the particle motion in a typical industrial precipitator by employing a novel particle charging process and Lagrangian approach. They pointed out that the collection efficiency of an ESP can be over-predicted when particle space charge effect is ignored. They also proved that small particles have more contribution to the particle space charge and electric field distortion since they provide larger value of the total surface area at a specific mass flow rate and stay in the region closer to the discharge wires for a longer time than larger particles. A few articles were reported in the literature, in which the strong coupling between the motion of ions, gas, particles and particle space charge density effect on corona discharge were considered [19,21]. In 2009, Adamiak and Atten implemented a 2-D FEM-MoC numerical method along with FLUENT software to simulate the gas flow and particle trajectories of submicron particles in a single-wire ESP [21]. The effect of particle concentration on gas flow streamlines, particle distribution pattern and current-voltage characteristics was also investigated. A full coupling between electric field, space charge and flow fields was assumed in their study and both corona discharge and particles charge influence on generating the secondary EHD flow were taken into account. They concluded that the flow pattern is modified by the secondary EHD flow, which strongly depends on the particle concentration.

2.4 Submicron particle collection using ESPs – Numerical modeling and experimental studies

ESPs are widely employed as particulate control devices for collecting fly ash emissions in different industrial processes, in which the overall mass based collection efficiencies should exceed 99%. However, for very small particles the collection efficiency of conventional ESPs is as low as 70%-80% due to the decreasing charge carried by particles of smaller size.

Increasing the collection efficiency of submicron particles in 0.1-1 μm range is a challenging problem due to the low charging rate and low migration velocity of these particles. Conventional ESPs cannot effectively collect the fine particles, but some methods are proposed by different authors to improve the collection efficiency of such particles. Applying ac corona discharge or dielectric barrier discharge (DBD) before a precipitator have been proposed by many authors to enhance particle agglomeration and improve the collection efficiency [58,59]. In 2009, B. Dramane *et al*. experimentally examined the ionic wind and high voltage power supply waveform effects on collection efficiency of submicron particles with mean size of about 0.3 μm inside a DC-ESP with positive or negative dc coronas and DBD-ESP with ac dielectric barrier discharge using a PIV method [60,61]. They concluded that the highest collection efficiency is obtained with the negative dc corona and at frequencies less than 30 Hz, and that the existence of DBD in the channel is as effective as the positive dc corona. They also demonstrated that the optimum distribution of ionic wind in time and space improves the submicron collection efficiency. In 2010, J. Zhu *et al*. developed a bipolar pre-charger to the inlet duct of an ESP, which effectively induced particle agglomeration and improved the collection efficiency to 95%-98% for all particle sizes [62]. In [63], J.-H. Kim *et al*. used a water electrospray prior to the ESP to produce charged fine droplets for improving particle charging and agglomeration. Using bag filters [64], a cyclone [65] or scrubber technology [66] are other techniques used to improve the submicron collection efficiency. Some others suggested smooth or spiked electrode geometries in narrow ESP channel. A. Niewulis *at al.* in [41,67,68] analyzed the EHD flow pattern in a narrow wire-plate ESP with either longitudinal or transverse wire electrode and evaluated the collection efficiency of submicron particles in the range of 0.25-1.5 μm ,where approximately 99% of them were of diameter below 1 μm, using 3-D PIV measurements. They proved the complex and 3-D character of particle flow in both cases. Contrary to the case of ESP with transverse wire electrode, they showed that in ESP with longitudinal wire electrode the spiral vortices generated along and across the ESP duct spread out along the channel and don't block the main flow resulting in lower pressure drop and smoother flow in the duct. In [68], authors proved that the ESP with longitudinal wire electrode energized with negative voltage has higher collection efficiency in removal of submicron particles due to higher discharge current and also proposed flocking plate electrodes to reduce re-entrainment of the fine particles deposited on the collecting plates. They also carried out some investigations to study the EHD flow field generated by different configurations of the electrode using PIV. In [25,26], they set up an experiment for the spike-plate type ESPs and investigated the secondary flow patterns effect on particle collection efficiency for submicron particles.

2.5 Diesel particle collection using ESPs – Numerical modeling and experimental studies

Removal of diesel exhaust particulates, with diameters typically less than 1 μm, has been a subject of interest and a big challenge during the past decades. These fine particles are very toxic and hazardous for the human respiratory system and are one of the main causes of air pollution in urban areas. Due to stricter regulations concerning air pollution control, more detailed investigations are needed to evaluate the collecting process and to propose improved designs for industrial applications.

Optimization of the engine combustion process using alternative fuels or special fuel additives and installing after-treatment systems, such as catalytic converters, wet scrubbers, cyclones, bag filters, DPFs and ESPs are among the conventional methods utilized during the past to reduce diesel particulate emissions. Although DPF has high removal efficiency, it still has many problems such as high pressure drop, high energy consumption and maintenance costs, durability and insufficient collection efficiency for nano-particles. On the other hand, ESPs are widely applied to control particulates in industrial applications proven to be more cost effective and capable of trapping nano-particles agglomerated to larger particles. Higher collection efficiency, lower pressure drop, low energy consumption and operating over a wide range of gas temperature have made ESPs reliable particulate control devices.

ESPs have been used by many authors to control diesel exhaust emissions [69-71]. Several authors have also worked on the electrostatic agglomeration of aerosols emitted by diesel engines [72-74] by moving their size distribution towards larger diameters (several micrometres at least).

Due to the low electrical resistivity of diesel particulates, they lose their charge as soon as they arrive at the collecting plates, and can easily re-enter the ESP channel resulting in a great decrease in particle removal efficiency. To overcome this problem, A. Mizuno and his co-workers proposed an electrostatic flocking technique, which increases the surface area on collecting electrodes and suppresses the re-entrainment of collected particles [75]. They also proposed that the gradient force produced at the tip of flocking fibers accelerates fine particles agglomeration and suppress the particle re-entrainment into the channel. In [76], the authors installed a dust pocket consisting of a metal mesh backed with a barrier discharge electrode downstream of the collecting electrode to suppress abnormal re-entrainment for conductive diesel particles. Their experimental results indicated that conductive particles touching the mesh of the dust pocket are pulled into the high electric field region, and are oxidized by the barrier discharge. However, a problem with this ESP was an abnormal amount of dust re-entrainment. The agglomerated particles repeated jump downstream and were emitted outside the ESP. In [77], the authors suggested an ESP-DPF combined system to obtain higher collection efficiency for diesel particulates, where the number density of particles measured in downstream of the combined system was 98 % less compared with that of DPF only. In addition, they confirmed that the increase in the pressure drop of the DPF is smaller due to agglomeration.

Wire-tube ESPs, where a thin wire is placed in the center of the tube and held at high voltage are proposed by some authors to capture ultra fine particles and diesel particulates [77-81]. Saiyasitpanich *et al.* [70,71] performed experiments to examine the performance of a tubular single-stage wet electrostatic precipitator (wESP) in the removal of diesel particulate matter. In wESP, the charged particles are collected on the wet collecting surfaces continuously irrigated with a water-film layer. This method is very advantageous in collecting ultrafine particles comparing with dry ESPs avoiding particle re-entrainment to the system and causes particle growth and agglomeration by cooling the system [82]. Moderate energy consumption, low maintenance requirements, simplicity in operation, no back pressure, and no interference with diesel engine operations are mentioned as some advantages offered by wESP. They evaluated the ESP performance for different operational control parameters including applied voltage, gas residence time, engine load, etc. Their results proved that the total diesel particulate number concentrations in the untreated diesel exhaust are in the order of $\sim 10^8/cm^3$ at all engine loads with mean particle sizes in the range of 20 and 40 nm. They showed that the precipitator performance degrades from 86% at 0 kW engine load to 67% at 75 kW engine load principally due to a decrease in gas residence time and an increase in particle concentration. The ESP performance at 75 kW engine load was increased up to 96% by creating a four times increase of the gas residence time in the channel. It was also proved that by increasing the corona power, the removal efficiency of particles was increased. In addition, they found that the ESP collection efficiency versus particle size have a minimum between 20-50 nm, but at optimal wESP operating conditions it is possible to remove 90% of the all particle sizes. The measured collection efficiencies were significantly higher than the predicted values based on the well-known Deutsch equation [83].

The secondary EHD flow generated in a circular tube by electric body forces has also been a subject of interest of many authors. R. B. Lakeh and M. Molki [84] pointed out that the eccentricity of the electrode is an important parameter and dramatically changes the flow field. They demonstrated that symmetric wire-tube geometry does not generate a secondary flow in circular cross sections and proved that the gas flow, responsible for thermal enhancements in circular tubes often reported in the published literature, is induced only when there is a slight asymmetry in the position of the electrode.

3. THEORETICAL FUNDAMENTALS AND MATHEMATICAL MODEL OF AN ESPs

3.1 Introduction

In order to investigate the fundamental phenomena affecting the ESP process, a basic configuration of the single-stage ESP with two grounded, parallel and flat electrodes, used as collection plates, and a cylindrical high-voltage wire, suspended in the mid-plane of the duct, is often considered. In this model, the particles are electrically charged in the non-uniform ionized electric field, move in combined electro- and hydrodynamic fields and are separated from the gas under the influence of electrostatic forces. Accurate evaluation of fluid mechanics and particle transport parameters, including EHD flow interaction with the turbulent flow field and turbulent particle transport, is necessary to optimize precipitator operation.

The detailed 3-D hybrid FEM-FCT numerical approach, implemented throughout the entire thesis, is explained for modeling the steady state corona discharge to obtain electrical characteristics inside a simple parallel plate channel containing a single corona wire. The whole simulation procedure and algorithm to accurately predict the electrostatic field, EHD flow, particle charging and turbulent motion, and their mutual interaction in a single wire-plate ESP model is discussed. The developed model is useful to gain insight into the particle collection phenomena that take place inside an ESP.

3.2 Mathematical Model of a Single-Stage ESP

A simple model of a typical wire-duct ESP is considered as shown in Figure 3.1. It consists of two mechanical components: two parallel plates creating the deposition channel (collecting plates) and a thin wire electrode placed at the center and parallel to the plates (corona wire). Two vertical side plates are electrically insulating and provide mechanical support for the other elements. A 3-D computation model is considered in Cartesian coordinates with $-0.25<x<0.25$ (m), $-0.05<y<0.05$ (m) and $-0.05<z<0.05$ (m) as the dimensions of the duct. The collecting plates are 0.1 m apart and the corona wire with a diameter of 1 mm is mounted along the z axis. The main gas flows in the positive x direction. This ESP configuration represents a single element of a typical multi-stage system.

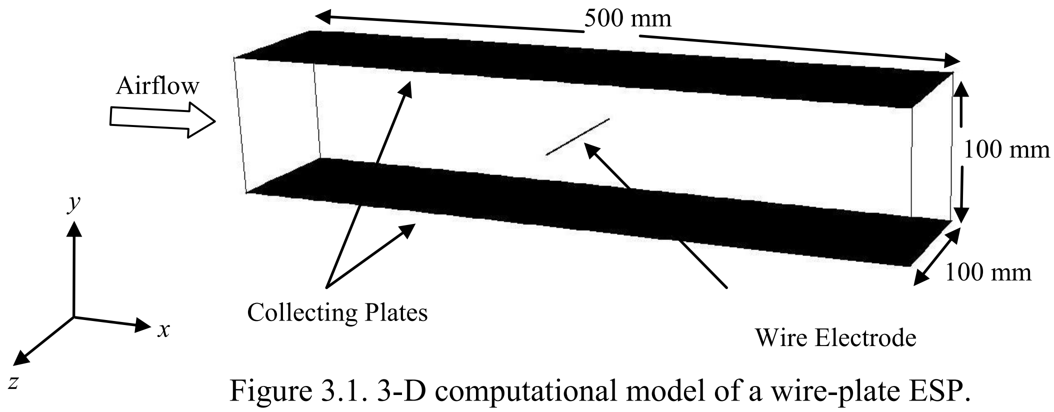

Figure 3.1. 3-D computational model of a wire-plate ESP.

The phenomena occurring during the precipitation process are extremely complex, mainly due to three fields being present at the same time: fluid flow, electrostatic and particle motion. The three existing fields and their mutual coupling are shown in Figure 3.2 [14]. The solid and dashed lines represent the strong and weak coupling between the two fields respectively. The computational model of the ESP should include the corona discharge, the gas flow and particle charging and transport. By applying a sufficiently high voltage to the corona wire, having a small radius of curvature, and keeping the collecting plates at a ground potential, a uniform corona takes place along the wire and the ions drift towards the collecting plates. These ions adhere to particles entrained with the airflow through the channel. As a result of electrostatic and air drag forces on the particles, they move towards the collecting plates and are deposited on them.

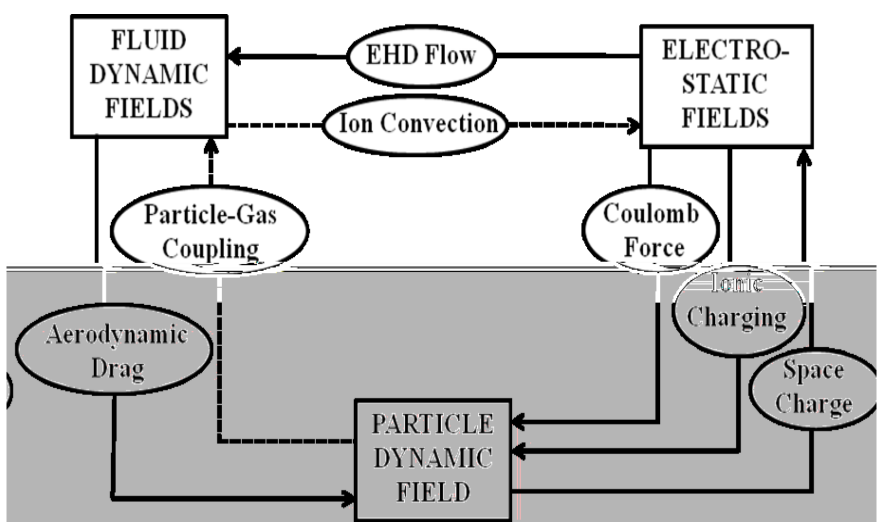

Figure 3.2. Fields interactions inside ESPs.

3.3 Theoretical Fundamentals

3.3.1 Corona discharge

Once corona discharge takes place in the ESP channel, the electric charges generated from the thin ionization layer surrounding the corona wire form a space charge in the drift zone. The electric field is thus governed by Poisson's equation:

$$\nabla^2 \Phi = -\frac{\rho_i}{\varepsilon_0}$$
$$\vec{E} = -\nabla \Phi \qquad (3\text{-}1)$$

where Φ is the scalar electric potential, ρ_i - the space charge density, $\vec{E}$ - the electric field intensity and ε_0 - the electric permittivity of the ambient gas.

The ionic charges are accelerated by the Coulomb force and move towards the ground plates. The drifting charges create an electric current with a density defined as:

$$\vec{J} = \rho_i (K\vec{E} + \vec{u}) - D\nabla\rho_i \qquad (3\text{-}2)$$

$$K = K_0 \times \frac{P_0}{P} \times \frac{T}{T_0} \qquad (3\text{-}3)$$

where $\vec{J}$ is the current density, D - the ions diffusion coefficient and $\vec{u}$ - the gas velocity, that may include both the EHD flow and the external airflow, T and P - the actual temperature and pressure of the air and T_0 (300 K) and P_0 (1.013×10^5 Pa) - the atmospheric temperature and pressure, K and K_0 - the mobility of ions at atmospheric and actual conditions, respectively.

The three terms on the right hand side of Eq. (3-2) are drift, convection and diffusion currents, respectively. Since the drift velocity of ions is usually about two orders of magnitude faster than the typical velocity of the gas flow, the convective component in the ionic current density can be neglected and the electric field computation is independent of the flow field, so:

$$\vec{J} = K\rho_i\vec{E} - D\nabla\rho_i \tag{3-4}$$

Under steady-state conditions, the current density must satisfy the charge conservation equation:

$$\nabla \cdot J = 0 \rightarrow \nabla \cdot (K\rho_i\vec{E} - D\nabla\rho_i) = 0 \tag{3-5}$$

3.3.2 Eulerian approach for the continuous phase (airflow)

The initial, and perhaps the most crucial step, in the study of aerosol deposition in the ESP is the flow field characterization. Proper representation of the primary flow is necessary for adequate prediction of particle deposition.

The ambient gas is considered an incompressible Newtonian fluid due to the small pressure drop across the ESP channel; thus having constant density and viscosity. Also, the flow is steady and turbulent assuming the *k-ε* model [85]. Under these assumptions, the airflow has to satisfy the continuity and the Navier–Stokes equations.

The Navier–Stokes equations are strictly a statement of the Newton's second law of motion (momentum equation), which states that the rate of change of momentum equals the sum of forces on the fluid particle [86].

$$\begin{aligned}
\frac{\partial(\rho_f\vec{u})}{\partial t} + \nabla\cdot(\rho_f u\vec{u}) &= -\frac{\partial P}{\partial x} + \nabla.(\mu\nabla\vec{u}) + S_{Mx} \\
\frac{\partial(\rho_f\vec{u})}{\partial t} + \nabla\cdot(\rho_f u\vec{u}) &= -\frac{\partial P}{\partial y} + \nabla.(\mu\nabla\vec{u}) + S_{My} \\
\frac{\partial(\rho_f\vec{u})}{\partial t} + \nabla\cdot(\rho_f u\vec{u}) &= -\frac{\partial P}{\partial z} + \nabla.(\mu\nabla\vec{u}) + S_{Mz}
\end{aligned} \tag{3-6}$$

where S_{Mx}, S_{My} *and* S_{Mz} *are* the source terms of *x*-momentum, *y*-momentum and *z*-momentum equations respectively, ρ_f - the gas density and μ – the gas viscosity.

Taking into account the assumption of an incompressible flow of a Newtonian fluid with constant density and viscosity, and negligible heat transfer, the Navier–Stokes equations are simplified in this form:

$$\rho_f[\frac{\partial \vec{u}}{\partial t} + \vec{u} \cdot \nabla \vec{u}] = -\nabla P + \mu \nabla^2 \vec{u} + \vec{F} \tag{3-7}$$

where $\vec{F}$ represents the external body forces on the gas molecules (force per unit volume), in this case equal to the Coulomb force $\vec{F} = \rho_i \vec{E}$, which is responsible for the corona generated EHD secondary flow (ionic wind).

If temperature effects are neglected, the only other equation (apart from initial boundary conditions) needed is the mass conservation or continuity equation, given in its most general form as:

$$\frac{\partial \rho_f}{\partial t} + \nabla \cdot (\rho_f \vec{u}) = 0 \tag{3-8}$$

Under the incompressible flow assumption, density is constant and the equation will simplify to:

$$\nabla \cdot \vec{u} = 0 \tag{3-9}$$

For laminar flow fields, these basic governing equations for the conservation of the mass and momentum are sufficient, while additional transport equations need to be solved when the flow is turbulent.

3.3.2.1 Turbulent model

The modeling procedure involves computing the flow Reynolds number (Re) to determine if turbulence modeling is necessary. If the Reynolds number based on the characteristic length of the channel and the existing external gas flow is above a critical value then the fluid flow is considered as turbulent. The presence of non-uniformly distributed Coulomb force increases the turbulence intensity of the flow and introduces further instability. The exact time dependent solutions of the Navier-Stokes equations in complex geometries for turbulent flows, which can represent the smallest scales of the motions, are unlikely to be achievable in the near future [87]. The Reynolds-averaging is one of the alternative methods that can be employed to render the Navier-Stokes equations tractable, so that the small scale turbulent fluctuations do not have to be directly simulated. In this case, additional terms need to be introduced into the governing equations in order to obtain a solution.

In Reynolds averaging, the solution variables in the instantaneous (exact) Navier-Stokes equations are decomposed into the mean (ensemble–averaged or time–averaged) and fluctuating components. For the velocity components:

$$u_i = \overline{u}_i + u'_i \tag{3-10}$$

where $\overline{u}_i$ and u'_i are the mean and fluctuating velocity components, respectively. The subscript "*i*" represents each dimensional component of the velocity, for example, it indicates *x*, *y*, *z* for 3-D Cartesian system.

Likewise for other scalar quantities:

$$\phi = \overline{\phi} + \phi' \tag{3-11}$$

where ϕ denotes a scalar, such as pressure, energy, or species concentration.

Substituting Eq. (3-10) into the instantaneous continuity and momentum equations, and taking a time (or ensemble) average (and dropping the overbar on the mean velocity, $\overline{u}$) yields the ensemble-averaged equations. They can be written in Cartesian tensor form using the Einstein summation convention as:

$$\begin{gathered} \frac{\partial u_i}{\partial x_i} = 0 \\ \frac{\partial}{\partial t}(\rho_f u_i) + \frac{\partial}{\partial x_i}(\rho_f u_i u_j) = -\frac{\partial P}{\partial x_i} + \frac{\partial}{\partial x_j}[\mu(\frac{\partial u_i}{\partial x_j} + \frac{\partial u_j}{\partial x_i} - \frac{2}{3}\delta_{ij}\frac{\partial u_i}{\partial x_i})] + \frac{\partial}{\partial x_j}(-\rho_f \overline{u'_i u'_j}) + f_i \end{gathered} \tag{3-12}$$

which are called Reynolds-averaged Navier-Stokes (RANS) equations. Additional terms, Reynolds stresses, $-\rho_f \overline{u'_i u'_j}$, now appear as a result of the averaging, representing the effects of turbulence and must be modeled to close Eq. (3-12). A common method employs the Boussinesq hypothesis [87] to relate the Reynold stresses to the mean velocity gradients:

$$- \rho_f \overline{u'_i u'_j} = \mu_t \left(\frac{\partial u_i}{\partial x_j} + \frac{\partial u_j}{\partial x_i} \right) - \frac{2}{3} \left(\rho_f k + \mu_t \frac{\partial u_i}{\partial x_i} \right) \delta_{ij} \tag{3-13}$$

3.3.2.2 Standard *k-ε* turbulent model

In this model, two additional transport equations (for the turbulence kinetic energy, *k*, and the turbulence dissipation rate, *ε*)

$$\frac{\partial}{\partial t}(\rho_f k) + \frac{\partial}{\partial x_i}(\rho_f k u_i) = \frac{\partial}{\partial x_j}\left[\left(\mu + \frac{\mu_t}{\sigma_k}\right)\frac{\partial k}{\partial x_j}\right] - \rho_f \overline{u'_i u'_j}\frac{\partial u_j}{\partial x_i} - \rho_f \varepsilon \tag{3-14}$$

and

$$\frac{\partial}{\partial t}(\rho_f \varepsilon) + \frac{\partial}{\partial x_i}(\rho_f \varepsilon u_i) = \frac{\partial}{\partial x_j}\left[\left(\mu + \frac{\mu_t}{\sigma_\varepsilon}\right)\frac{\partial \varepsilon}{\partial x_j}\right] + C_{1\varepsilon}\frac{\varepsilon}{k}\left(-\rho_f \overline{u'_i u'_j}\frac{\partial u_j}{\partial x_i}\right) \tag{3-15}$$

are solved, and the turbulent (or eddy) viscosity μ_t is computed as a function of *k* and *ε* using the following expression:

$$\mu_t = \rho_f C_\mu \frac{k^2}{\varepsilon} \tag{3-16}$$

where model constants $C_{1\varepsilon}$, $C_{2\varepsilon}$, C_μ, σ_k, and σ_ε have the following default values [87]:

$C_{1\varepsilon} = 1.44$, $C_{2\varepsilon} = 1.92$, $C_\mu = 0.09$, $\sigma_k = 1.0$, and $\sigma_\varepsilon = 1.3$.

3.3.2.3 Turbulence intensity

The Turbulence intensity, *I*, often referred to as turbulence level, is defined as the ratio of the root mean square (RMS) of the turbulent velocity fluctuations, u', to the mean flow velocity, *U*, as:

$$I = \frac{u'}{U} = \sqrt{\frac{2}{3}k} \Big/ U, \qquad U = \sqrt{u_x^2 + u_y^2 + u_z^2} \tag{3-17}$$

Two-thirds the turbulence kinetic energy (k) assumes isotropic turbulence and corresponds to averaging the three fluctuating components ($u' = \sqrt{\frac{1}{3}(u'^2_x + u'^2_y + u'^2_z)} = \sqrt{\frac{2}{3}k}$).

The conservation equations and assumptions presented in this section can be found in any standard gas dynamics, compressible fluid flow, or viscous flow textbooks [88].

3.3.3 Lagrangian approach for the dispersed phase (particle)

In the aerosol-laden gas flow (two-phase) problem in an ESP, the Eulerian model describes gas (continuous phase) behavior while the particle phase (dispersed phase) is simulated based on the Lagrangian approach, where the trajectories of a large number of individual particles are traced with their motion affected by the gas flow and electrostatic forces.

3.3.3.1 Particle motion equations

In general, particles are subjected to the combined effects of gravitational and the electrostatic body forces, as well as the aerodynamic forces due to interaction between the gas and particles along their trajectory. This force balance equates the particle inertia with the forces acting on the particle and can be written as:

$$\frac{d\vec{u}_{p,i}}{dt} = \vec{F}_D(\vec{u}_i - \vec{u}_{p,i}) + \frac{\vec{g}_i(\rho_P - \rho_f)}{\rho_P} + \vec{F}_x \tag{3-18}$$

where

$$\frac{dx_i}{dt} = u_i \qquad ; \qquad i = x, y, z \tag{3-19}$$

where ρ_P and $\vec{u}_{P,i}$ denote the density and velocity of particles, respectively and $\vec{g}_i$ - gravitational acceleration acting in vertical direction, which causes the particle to descend in the gas. $\vec{F}_x$ corresponds to the external acceleration (force/unit particle mass) exerted on the particles that, in this study, is the electrostatic force:

$$\vec{F}_x = \frac{\vec{E} Q_P}{m_p} \tag{3-20}$$

where Q_P and m_P denote the electric charge and mass of the particle respectively. $F_D(\vec{u}_i - \vec{u}_{p,i})$ is the drag force per unit particle mass due to the relative velocity of the particle and the fluid, defined as:

$$F_D = \frac{18\mu}{\rho_P d_p^2} \frac{C_D \operatorname{Re}}{24} \tag{3-21}$$

where d_p is the particle diameter and Re is the relative Reynolds number:

$$\operatorname{Re} \equiv \frac{\rho_f d_p \left| \vec{u}_{p,i} - \vec{u}_i \right|}{\mu} \tag{3-22}$$

The drag coefficient, C_D, can be taken from either:

$$C_D = a_1 + \frac{a_2}{\operatorname{Re}} + \frac{a_3}{\operatorname{Re}^2} \tag{3-23}$$

where a_1, a_2 and a_3 are constants that apply for smooth spherical particles over several ranges of Re given by Morsi and Alexander [89] or

$$\begin{aligned}
C_D &= \frac{24}{\operatorname{Re}}(1 + b_1 \operatorname{Re}^{b_2}) + \frac{b_3 \operatorname{Re}}{b_4 + \operatorname{Re}} \\
b_1 &= \exp(2.3288 - 6.4551\chi + 2.4486\chi^2) \\
b_2 &= 0.0964 + 0.5565\chi \\
b_3 &= \exp(4.905 - 13.8944\chi + 18.4222\chi^2 - 10.2599\chi^3) \\
b_4 &= \exp(1.4681 + 12.2584\chi - 20.7322\chi^2 + 15.8855\chi^3)
\end{aligned} \tag{3-24}$$

which is taken from Haider and Levenspiel [90].

The shape factor, χ, is defined as

$$\chi = \frac{s}{S} \tag{3-25}$$

where s is the surface area of a sphere having the same volume as the particle, and S is the actual surface area of the particle. The Reynolds number, Re, is computed with the diameter of a sphere having the same volume.

For sub-micron particles, a different form of Stokes' drag law is needed [91]. In this case, F_D is defined as:

$$F_D = \frac{18\mu}{\rho_p d_p^2}\frac{1}{C_c(\lambda)} \tag{3-26}$$

For dry air at atmospheric conditions, C_c is the Cunningham slip correction factor to Stokes' drag law and is computed from:

$$C_c(\lambda) = 1 + K_n[1.257 + 0.4\exp(-\frac{1.1}{K_n})], \qquad K_n = \frac{2\lambda}{d_p} \tag{3-27}$$

where K_n - the Knudsen number, λ is the molecular mean free path, the average distance traveled by a gas molecule between collisions with other molecules, at actual conditions [92]. The molecular mean free path is defined in terms of Boltzmann's coefficient ($k_B = 1.38066 \times 10^{-23}$ J/K) and σ - gas accommodation coefficient [93] as:

$$\lambda = \frac{k_B T}{\sqrt{2}\pi\sigma^2 P} \qquad \frac{\lambda}{\lambda_0} = \frac{\mu}{\mu_0} \times \sqrt{\frac{T}{T_0}} \times \frac{P_0}{P} \qquad [m] \tag{3-28}$$

where λ_0 ($6.609 \times 10^{-8}\ m$) is the molecular mean free path at atmospheric conditions (T_0, P_0).

In this thesis, the gravitational forces and Brownian forces are neglected, but electrical and air drag forces are considered as the two main forces acting on the particles [44]. Turbulent particle dispersion is also considered for stochastic tracking of particles in turbulent flow by activating DRW model in FLUENT. It has been shown [94] that particle diffusion is generally dominated by turbulence dispersion in an isotropic flow field and the Brownian diffusion has no significant effects on the particle response statistics. However, the effect of Brownian diffusion could become important near the wall. The Brownian forces in FLUENT is intended only for non-turbulent models. As a result, the particle trajectories deflect towards the ground plate; a smaller particle size usually leads to a smaller deflection level. In this study, the particles which touch the collecting plates are assumed to be removed from the computational model.

3.3.3.2 Particle charging equations

In this analysis, inert particles are injected into the continuous phase (airflow) from a pre-defined surface (Inlet) of the ESP channel. The injected particles are assumed to be spherical and electrically neutral, moving with a uniform initial velocity equal to the gas velocity. The particles acquire some charges as they pass through the ESP channel due to exposure to the ion flux in the electrostatic field. These particles are simultaneously charged by two mechanisms: field charging (ionic bombardment) and diffusion charging [46], then move towards the collection plates under the Coulomb force and are eventually deposited on them. The field charging occurs when the actual particle charge Q_p is smaller than the saturation charge Q_s, given by the formula:

$$Q_s = \frac{3\varepsilon_r}{\varepsilon_r + 2}\pi\varepsilon_0 d_p^2 \left|\vec{E}\right| \tag{3-29}$$

where ε_r is the dielectric constant of the particle.

Diffusion charging can occur if Q_p is above the saturation level. The overall charging rate is given by the following formulae [21]:

$$\frac{dQ_p}{dt} = \begin{cases} \frac{Q_s}{\tau_q}\left(1 - \frac{Q_p}{Q_s}\right)^2 + \frac{2\pi\alpha\rho_i K k_B T d_p}{e} & Q_p < Q_s \\ \frac{\alpha}{4\tau_q}(Q_p - Q_s)\exp\left(\frac{e(Q_s - Q_p)}{2\pi\varepsilon_0 k_B T d_p}\right) & Q_p > Q_s \end{cases} \tag{3-30}$$

where

$$\alpha = \begin{cases} 1 & e_{norm} < 0.525 \\ \dfrac{1}{(e_{norm} + 0.457)^{0.575}} & e_{norm} > 0.525 \end{cases} \tag{3-31}$$

$$e_{norm} = \frac{ed_p}{2k_B T} |\vec{E}|; \qquad \tau_q = \frac{4\varepsilon_0}{K\rho_i}$$

τ_q is the charging time constant and e – the electronic charge (1.6×10^{-19} C).

Therefore, the charging level is dependent on the size and shape of a particle, the unipolar ion density, the particle residence time and the electric field intensity. The particle charge at any instant of time can be calculated by integrating the charging rate with time along the real particle trajectory.

The particle charging process and the particle motion are mutually coupled. The particle charge increases when the particle moves into an area of higher electric field. However, large particle charge affects the particle trajectory due to an increased electrostatic force.

In the case of dilute particle concentration at the inlet, the particle space charge density effect on corona discharge can be ignored. However, a large concentration of particles increases the particle charge density, which subsequently changes the electrical potential and the ion charge density distribution. Therefore, for high particle concentrations at the inlet the effect of particulate space charge has been included in the calculation of the electric field and the current density distribution, by considering two space charge components in the Poisson equation, Eq. (3-1); gaseous ions (ρ_i), and the charged particles (ρ_{DPM}), which do not have the same spatial distribution [21]. Therefore, the Poisson equation should be modified as:

$$\nabla^2 \Phi = -\frac{\rho_i + \rho_{DPM}}{\varepsilon_0} \tag{3-32}$$

Furthermore, the presence of a high concentration of charged particles in the ESP channel contributes to the generation of EHD flow in Eq. (3-7), where $\vec{F} = (\rho_i + \rho_{DPM})\vec{E}$, modifying the airflow pattern as well. These flow patterns are not symmetric with respect to the vertical plane crossing the corona wire: upstream of the corona wire the particles are not fully charged yet, so in this region the electrical body force is much smaller than in the downstream region, where the particles are fully charged and much stronger EHD flow can be expected. The mathematical model presented in this thesis takes into account the strong coupling between all these phenomena to accurately predict the particle motion in the precipitators.

3.3.3.3 Particle migration velocity

For practical work, it seems to be more reasonable to use an analytical solution that describes charging processes continuously from small to larger particle sizes. The particle charging model introduced by Cochet [95] for predicting charge on each particle is shown in Eq. (3-33). The model assumes that each particle size attain an equivalent maximum amount of charge, Q_p, for a charging time equal to infinity.

$$Q_p(d_p) = \pi\varepsilon_0 d_p^2 [(1+K_n)^2 + \frac{2}{1+K_n}\frac{\varepsilon_r - 1}{\varepsilon_r + 2}]\left|\vec{E}_{ps}\right| \tag{3-33}$$

where $\left|\vec{E}_{ps}\right|$ is the pseudo-homogeneous electric field strength calculated from the formula:

$$\left|\vec{E}_{ps}\right| = \frac{\Phi_0}{R_{NE}} \tag{3-34}$$

where Φ_0 - the applied voltage to corona electrode and R_{NE} - the distance between corona electrode and collecting surface. However, the $\left|\vec{E}_{ps}\right|$ represents only a rough estimate of the real value, because it characterizes the electric field only for parallel plate electrodes, while in practice, the electric field is usually generated between wire and plate, or wire and tube.

The first theoretical performance model for particle collection inside the precipitator has been suggested by Deutsch [96]. Eq. (3-35) shows the grade or fractional efficiency, η_f, normally referred to as the original Deutsch equation.

$$\eta_f(d_p) = 1 - \frac{M_{out}(d_p)}{M_{in}(d_p)} = 1 - \exp(-D_e), \qquad D_e = \mathrm{SCA}\ \varpi_{th}, \qquad \mathrm{SCA} = \frac{A_c}{Q} \tag{3-35}$$

where D_e is the Deutsch number, SCA – the specific collection area, A_c - the effective collecting area, Q - the exhaust gas flow rate, ϖ_{th} – the theoretical migration velocity and

$M_{in}(d_p)$ and $M_{out}(d_p)$ are the total mass of each particle size at the inlet and outlet of the ESP channel.

As it can be seen from Eq. (3-35), the collection efficiency improves with increasing the specific collection area (SCA). An increase in SCA can be achieved either by increasing the residence time of the particles in the electric field (increasing the length of the channel or reducing the gas velocity) or by reducing the channel width, which results in a shorter distance a particle has to travel to reach the collecting electrode. The theoretical migration velocity is obtained by balancing the drag force with the electrostatic force (Coulomb force) acting on the particle and can be expressed as:

$$\varpi_{th} = \frac{C_c(\lambda) Q_p(d_p)}{3\pi\mu d_p}\left|\vec{E}_{CE}\right| \tag{3-36}$$

$$\varpi_{th} = k_p(d_p)\left|\vec{E}_{CE}\right| \qquad , K_p = \frac{C_c(\lambda) Q_p(d_p)}{3\pi\mu d_p} \tag{3-37}$$

$$\varpi_{th} = \left|\vec{F}_s\right|\frac{C_c(\lambda)}{3\pi\mu d_p}, \qquad \left|\vec{F}_s\right| = \left|\vec{E}_{CE}\right| \times Q_p(d_p) = \frac{3\pi\mu d_p \varpi_{th}}{C_c} \tag{3-38}$$

where K_p is the particle mean mobility, $\left|\vec{E}_{CE}\right|$ - the electric field strength near the collecting wall and $\vec{F}_s$ - viscosity force.

The original Deutsch Eq. (3-35) is widely used in ESP design because of its simplicity. However, in practice the non-idealized phenomena such as corona current suppression due to very high inlet dust loading, intermittent sparkover, turbulent diffusion, and gas channelling usually occur and tend to reduce the predicted particle collection efficiency. Therefore, in most cases, the original Deutsch model does not give good agreement between theory and experiment. To account for those non-idealized phenomena, the theoretical migration velocity is replaced by the global drift velocity the so-called the effective migration velocity (ϖ_e) to include all the particle transport-related aspects not explicitly recognized in the original Deutsch model [97,98]. The effective migration velocity is a critical parameter which depends on numerous factors such as: the magnitude and wave form of the applied voltage, the mean gas velocity, the size distribution of particles [23], the geometry of the ionization electrode [22], the gas temperature and relative humidity, the characteristic scales of ESP, etc. [99-101]. This parameter can normally only be obtained from pilot studies or from previous experience with similar ESP application.

Therefore, the total mass collection efficiency, η_t, can be obtained from the following formula:

$$\eta_t = 1 - \exp(-\frac{\varpi_e A_c}{Q}), \qquad \eta_t = 1 - \frac{M_{out}}{M_{in}}, \qquad \varpi_e = \beta\omega_{th} \tag{3-39}$$

where M_{in} and M_{out} are the total masses of all particle sizes at the inlet and outlet of the ESP channel, ϖ_e – the effective migration velocity and β is an empirical coefficient required for the actual ESP design. This equation can be used to estimate the total mass removal of mono-disperse and also polydisperse particles inside the ESP when ϖ_e is known.

For the wire – cylindrical tube geometry η_t can be obtained from the following formula:

$$\eta_t = 1 - \exp(\frac{-\varpi_e A}{Q}) = 1 - \exp(\frac{-2\varpi_e L}{u_0 r_1}) \tag{3-40}$$

$$\varpi_e = -\frac{Q}{A}\ln(1-\eta_t) = -\frac{u_0 r_1}{2}[\ln(1-\eta_t)]$$

where L is the tube length, r_1 – the tube radius, u_0 – initial velocity of exhaust gas at inlet.

However, many authors [70,71,102-104], have reported a considerably higher measured fractional efficiency of fine particles than the calculated ones from Deutsch equation. Peukert and Wadenpohl [102] concluded that the Deutsch model in combination with Cochet 's law are not able to describe the particle collection efficiency correctly. Some factors, including particle motion calculations in inhomogeneous distribution of the electric field in the ESP channel and higher amount of charge carried by particles than those assumed by Cochet's model, were mentioned as possible reasons leading to higher collection efficiency. Since axial symmetric cylindrical ESP geometry was considered, the electrical wind effect was not mentioned as a possible factor in predicting higher collection efficiency in these cases.

3.3.4 Boundary conditions

The boundary conditions for the potential are straightforward: a given dc potential of Φ_0 at the corona electrode and zero at the ground planes (Dirichlet boundary conditions). However, formulation of proper boundary conditions for the space charge density is not so easy and some form of the injection law has to be assumed. The Katpzov hypothesis is adopted throughout Chapters 4 and 6, where a smooth corona wire electrode with uniform charge on its surface is assumed. This suggests that the electric field increases proportionally to the voltage below the corona onset, but will preserve its value after the corona is initiated. Peek's formula is used to determine the threshold strength of electric field for the corona onset at the corona electrode [105,106]. For cylindrical geometry, Peek's formula has the following form [107]:

$$E_p = 3.1 \times 10^{-6} \times \delta \times \left(1 + \frac{0.0308}{\sqrt{r_0 \delta}}\right) \quad , \quad \delta = \frac{T_0}{T} \times \frac{P}{P_0} \tag{3-41}$$

where r_0 is the radius of corona wire.

This approach provides an indirect boundary condition for the space charge density. The value of space charge density on the corona electrode surface is iterated until the corona electrode electric field is sufficiently close to Peek's value. However, for tufts or spiked corona electrodes where the ionic charge density on the electrode surface is non uniform and corona is initiated only from the tips of the spikes (Chapter 5), this formula is not valid. In this case, the experimental measured corona discharge current reported in literature has been used as a reference value in evaluating charge density on the corona electrode surface. The iterations are stopped when the calculated corona current is approximately equal to the experimental value.

The boundary conditions for the airflow are also straightforward: the two collecting plates, two insulating plates and wire surface act as stationary walls, where all components of the velocity vector vanish. The outside boundary of the domain is defined as velocity inlet and outflow. Since the computational domain is open in this area, the air is free to flow in both directions.

The boundary conditions for particle phase simulation are as follows. The trap boundary condition was set for the collecting plates, which terminates the trajectory calculation when the particle strikes the wall. Reflect boundary condition on the wire and insulating plates' surfaces rebounds particle off the boundary upon contact depending of the coefficient of restitution. A normal or tangential coefficient of restitution equal to unity implies that the particle retains all of its normal or tangential momentum after the rebound (an elastic collision). The converse holds for a setting of zero for the coefficient of restitution, inelastic collision. An elastic collision has been considered throughout the entire thesis. Escape boundary condition is assumed at the inlet and outlet boundaries, where the particle trajectories are terminated and particles exit from the computational domain. Table 3.1 summarizes the boundary conditions for the proposed model in Figure 3.1.

3.4 Iterative loops and calculation procedure

The first step in using FLUENT is to create the solid geometry of the system under investigation and to generate the mesh for the computational domain. Here, the pre-processor GAMBIT 2.2, part of the FLUENT family of software, has been used for this purpose. Then, the generated mesh is imported into the FLUENT solver.

The Poisson and current continuity equations, Eq. (3-1) and Eq. (3-5), with two unknown distributions: potential Φ and space charge density ρ_i, are the two governing equations describing the corona discharge model. These equations are solved using the proposed 3-D hybrid FEM-FCT numerical technique. In [108,109] the FEM-FCT method was used to simulate a 2-D streamer corona. A complete description of the FEM-FCT method can be found in [110].

The entire algorithm to obtain the electrical characteristics inside the ESP channel consists of two iterative loops, the inner loop for calculating the electric field and the space charge density in the precipitation channel, and the outer loop for calculating the charge density on the corona electrode surface. In summary, the iterative procedure includes the following steps:

1. Set an initial guess for the space charge density ($\rho_i \neq 0$) everywhere within the domain.

2. Make an initial guess for the space charge density on the corona wire surface (ρ_0).

3. Solve Eq. (3-1) for Φ using FLUENT.

4. Solve the conservation of current, Eq. (3-5), for the space charge density using FEM-FCT.

5. Return to step 3 until the solution becomes self-consistent.

6. Update the charge density on the surface of the wire by comparing the actual electric field intensity with Peek's value in case of smooth corona electrode, or by comparing the calculated corona discharge current with the experimental value in the case of tuft or spiked electrode.

7. Rescale the space charge density within the domain considering the new charge density on the corona wire surface.

8. Return to step 3 and repeat the procedures until the average electric field magnitude on the wire surface is sufficiently close to Peek's value, or the calculated discharge current is approximately equal to the experimental values.

The next step is solving the continuous phase (airflow) governed by time-averaged Navier-Stokes equation. In the whole thesis, the airflow is assumed to be incompressible and turbulent, and the momentum and mass conservation equations, Eq. (3-7) and Eq. (3-9), are solved in the CFD FLUENT 6.2 software using FVM method. This program is based on the pressure-correction method and uses the SIMPLE (Semi-Implicit Method for Pressure Linked Equations) algorithm [111]. The second order upwind differencing scheme is implemented for solving conservation of mass and momentum equations. The *k-ε* turbulent model with turbulence intensity between 5-10% is usually assumed (A turbulence intensity of 1% or less is generally considered low and turbulence intensities greater than 10% are considered high). The *k*-ε turbulence models in FLUENT yielded results of the continuous phase turbulence phenomena. The *k-ε* model used in this project adopts this hypothesis. The obtained electric field and space charge density distributions are used for calculating the electric body force, $\vec{F} = \rho_i \vec{E}$ in Eq. (3-7), responsible for generating EHD secondary flow in the ESP channel, are entered into every single volume cell of the discretized FLUENT model using the corresponding UDFs. The solution of the airflow equations provides the hydrodynamic conditions for the calculation of particle motion. Silky and Hound clusters in Sharcnet computing network were chosen to do the simulations for this part which are suitable for very large memory applications. The total computational time was approximately 2-3 days in Hound and almost 4-6 days in Silky depending on the total number of nodes and elements in the computational models with different discharge electrode geometries. Silky operating system is SUSE Enterprise 10 with 128 cores, processor: Itanium2 @ 1.6 GHz, memory (RAM): 256 GB and local storage: 2000.0 GB. Number of cores and memory devoted for each job are determined by server once jobs are submitted in this cluster. Hound cluster operation system is CentOS 5.4 with 496 cores, processor: Xeon @ 2.66 GHz and local storage: 6500.0 GB. In this cluster, user can determine the amount of memory required for each job in submission time. Maximum 8 GB memory (RAM) was devoted for simulations in this thesis.

Once the continuous phase (airflow) is calculated, particles are introduced in the system through the inlet boundary by including the DPM in the calculations to get the particle trajectories and deposition. The Lagrangian DPM in FLUENT solves the dispersed phase by tracking a large number of particles. Although this method needs a larger memory and computing time in comparison with the Eulerian method, it accurately models the particle transport and calculates the particle charging history along the trajectory. The Lagrangian model employs the solved Eulerian equations for the fluid phase and then integrates the force balance on the particle through Lagrangian equation of motion for the dispersed phase, Eq. (3-18), tracking individual particles through the flow field. The stochastic tracking, Discrete Random Walk (DRW) model, includes the effect of instantaneous turbulent velocity fluctuations on the particle trajectories via stochastic methods. Particle charging equations, Eq. (3-30) and Eq. (3-31), are numerically solved inside the corresponding UDF in FLUENT. This part of simulations was carried out using a computer with 32-bit operating system, processor: Intel (R) Core (TM) 2 Duo CPU, E6850 @ 3.0 GHz and memory (RAM): 4 GB. The discrete phase formulation contains the assumption that the second phase is sufficiently dilute that particle-particle interactions and the effects of the particle volume fraction on the gas phase are negligible. These issues imply that the discrete phase must be present at a low volume fraction, usually less than 10-12%. Thus, a one-way coupled model assumes that particle motion is influenced by the continuous gas phase, but the gas phase is unaffected by the presence of the particles. However, in the case of high particle concentration at inlet, the particulate space charge effect has also been considered in the calculation of electric field and charge density distribution, Eq. (3-32), and thus electrostatic body forces on air molecules generating EHD secondary flow in the channel. Therefore, a two-way coupling between particle and airflow phases should be considered. The procedure for analysis of the whole precipitation process can be summarized as follows:

1. Evaluate the electric potential and ionic space charge distribution in the whole channel by solving the Poisson and current continuity equations using the hybrid FEM-FCT technique.
2. Solve the gas-phase flow with the effect of electrostatic body forces, calculated using UDFs, in FLUENT.
3. Determine the coupled motion and space charge equations of particulate phase using DPM in FLUENT.
4. Return to Step 1, adding the particulate charge density to Poisson and current continuity equations to calculate the new ionic charge density and electric potential distributions in the channel, and adding particle space charge effect to calculate new electrostatic body forces in Step 2, *i. e.* $\vec{F} = (\rho_i + \rho_{DPM})\vec{E}$.
5. Stop the iterations when the average electric field magnitude on the wire surface is sufficiently close to Peek's value or the calculated corona discharge current agrees with the experimental measurements.

The flowchart of the simulation procedure is also demonstrated in Figure 3.3.

Table 3.1. Boundary conditions for 3-D analysis of processes in ESP.

Surfaces	**Air Flow**	**Electric potential**	**Space charge density**	**Particle**
Inlet (x = -0.25 m)	Velocity Inlet $u_x = u_0, u_y = 0, u_z = 0$	$\frac{\partial \Phi}{\partial n} = 0$	$\frac{\partial \rho_i}{\partial n} = 0$	Escape
Outlet (x = +0.25 m)	Outflow Pressure = 0	$\frac{\partial \Phi}{\partial n} = 0$	$\frac{\partial \rho_i}{\partial n} = 0$	Escape
Collecting electrodes (y = -0.05 m ; y = +0.05 m)	Stationary Walls $u_x = 0, u_y = 0, u_z = 0$	$\Phi = 0$	$\frac{\partial \rho_i}{\partial n} = 0$	Trap
Insulating side walls (z = -0.05 m ; z = +0.05 m)	Stationary Walls $u_x = 0, u_y = 0, u_z = 0$	$\frac{\partial \Phi}{\partial n} = 0$	$\frac{\partial \rho_i}{\partial n} = 0$	Reflect
Wire (discharge electrode) $(\sqrt{(x^2 + y^2)} = 0.5\ \text{mm})$	Stationary Walls $u_x = 0, u_y = 0, u_z = 0$	$\Phi = \Phi_0$	$\rho = \rho_0$	Reflect

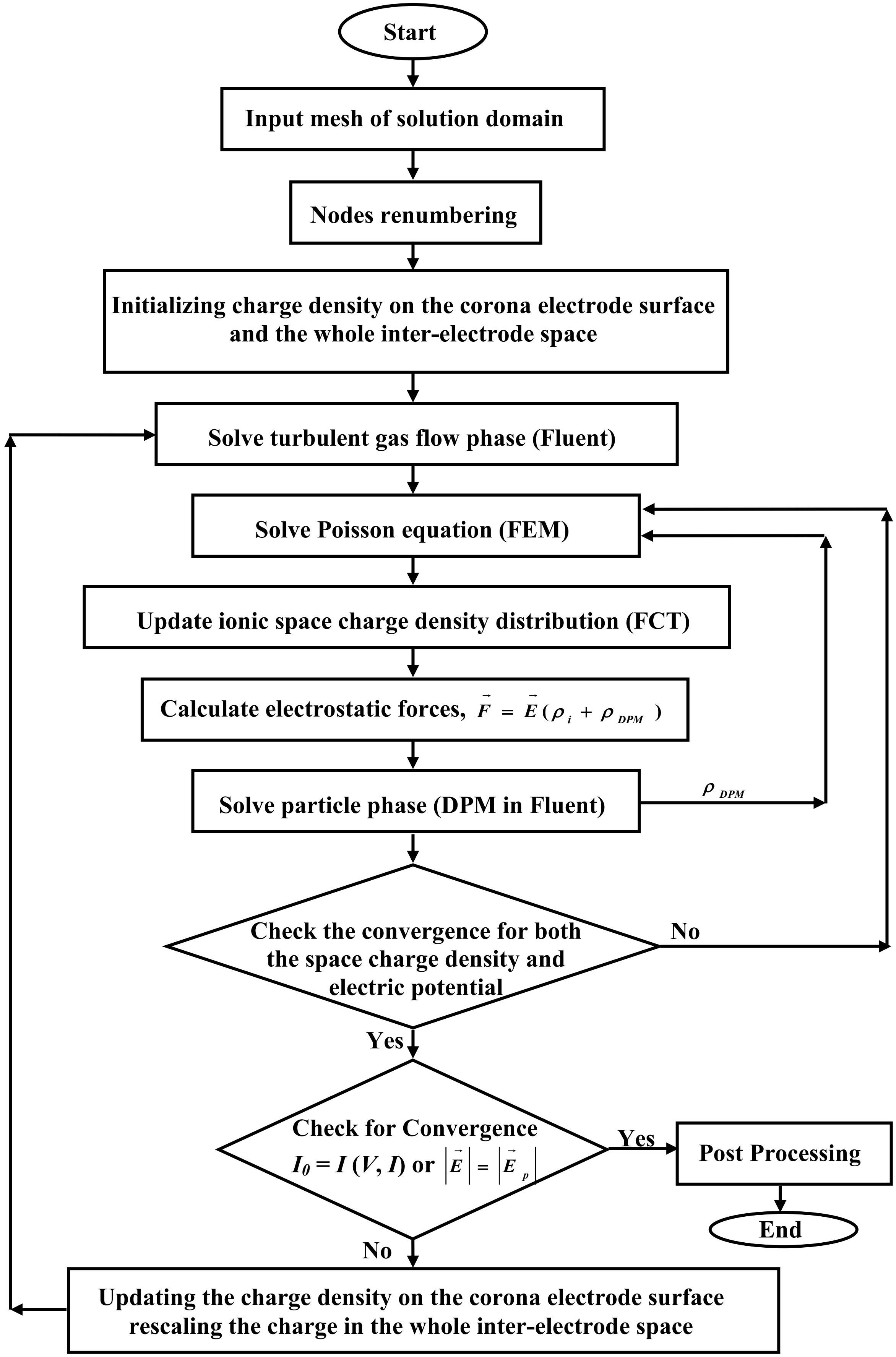

Figure 3.3. Flow chart of simulation procedure

4. A SINGLE-STAGE WIRE-PLATE ESP MODELING

4.1 Introduction

In this chapter, the results of the numerical simulation of a simple one-stage single wire-plate ESP are discussed. The simulation procedure described in Chapter 3 has been implemented to solve the governing equations describing the motion of ions, gas, solid particles and the effect of particle space charge. Uniform corona current distribution along the wire, i.e. positive corona discharge, has been assumed and the calculations involved the evaluation of the electrostatic fields, space charge density in the inter-electrode space, the build-up of charge on the particles and resulting electrical forces. A number of subroutines were written, compiled and linked with the commercial FLUENT software. The airflow equations were solved inside FLUENT using FVM and the turbulence effect was included by using the k-ε model. The Lagrangian random walk approach was used to determine particle motion, as affected by EHD flows and turbulence effects. This part was performed with the aid of DPM module in FLUENT. The model took into account the particle space charge density effect on the ionic charge density distribution and the complete mutual interaction mechanisms between the three coexisting fields of gas flow, particle trajectories and electrostatic field.

The performance of the discussed ESP in the removal of particulates and the effect of different particle concentration on the gas flow pattern and corona discharge current have been evaluated for both mono-dispersed and poly-dispersed particles with lognormal particle size distribution. Selected results of the simulation are presented showing the particle trajectories inside the ESP under the influence of both aerodynamic and electrostatic forces.

4.2 Model description

The 3-D computation model of a simple wire-duct ESP used in this chapter is shown in Figure 3.1. The computational domain was discretized using the commercial software GAMBIT. Since fine discretization is essential for good accuracy and smoothness of the solution, the whole domain was discretized into 148615 tetrahedral elements and 28520 nodes with a very non-uniform density; the elements in the vicinity of the thin corona wire are much smaller than in other places especially very close to the collecting plates. A +30 kV dc voltage was applied to the corona wire assuming uniform discharge along the electrode. The operating gas is ambient air (density ρ_f = 1.255 [kg/m^3] and viscosity μ = 1.7894e-5 [kg/m.s]), while the particles are assumed to be spherical with relative permittivity, ε_r, equal to 3.0 and mass density, ρ_p, equal to 998.2 [kg/m^3] with shape remaining unchanged during their motion. Neutral particles were injected in the *x* direction between the collecting plates at the precipitator entrance with the same initial velocity as the gas stream (1 m/s) and they are charged as they move through the channel and cross the ionic space charge zone. Collision and coagulation between particles were also neglected.

4.3 Simulation results and discussions

4.3.1 Electrical characteristics

Although there is a small coupling between the space charge density and air flow velocity due to charge convection term in Eq. (3-2), this effect is ignored here as it is essentially negligible. Thus, for any airflow velocity, the potential and the corresponding space charge density distributions in the symmetry plane (z = 0) for the +30 kV applied voltage are shown in Figure 4.1 and Figure 4.2. It can be seen that the potential contours in the vicinity of the corona wire are dense with circular shape, producing very high and practically constant electric field around the wire, and sparser with elliptical shape when moving towards the ends of the ESP channel (Figure 4.1).

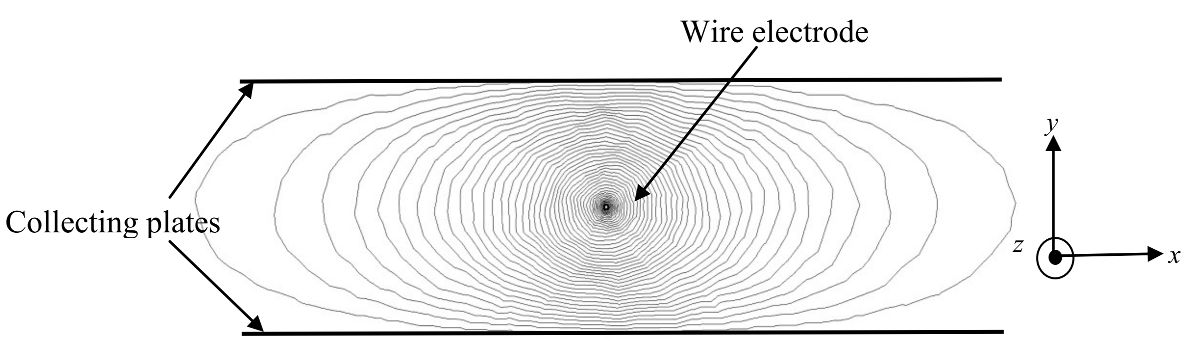

Figure 4.1. Distribution of equipotential lines in the symmetry plane of ESP (corona wire voltage is +30 kV, voltage increment 1.2 kV).

Similarly, the space charge density contours are shown in Figure 4.2. The maximum value of 187 μC/m^3 is located close to the surface of the corona wire and then the charge density rapidly decreases moving away from the wire electrode surface. Since the highest space charge density is concentrated in the area close to the corona wire, it is here where the dust particles very quickly attain most of their charge and experience the strongest Coulomb force, acting towards the grounded collecting plates. When the particle charge is neglected, the total discharge current of $I_0 \approx 108$ μA, corresponding to the charge density of 187.0 μC/m^3 on the corona electrode surface, is obtained, which is in a good agreement with the experimental data [21].

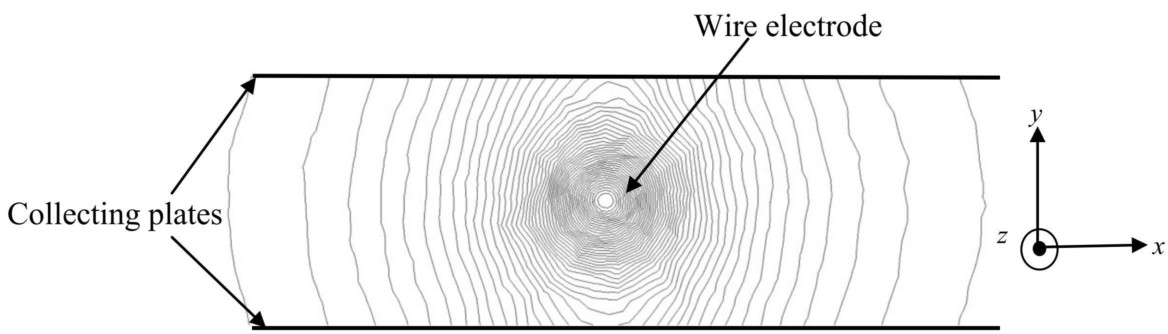

Figure 4.2. Lines of equal space charge density in the symmetry plane of ESP (corona wire voltage equal to +30 kV, maximum space charge density 187.0 μC/m^3, increment 7.65 μC/m^3).

4.3.2 3-D EHD flow patterns under different inlet air velocities

The effect of EHD flow, generated by the corona discharge, on the main air flow in the symmetry plane $z = 0$ is shown in Figure 4.3a - Figure 4.3f for both front and side views. The inlet velocity varies from 0 to 1.0 m/s, and the results show that the EHD flow modifies the main gas flow and makes the whole flow pattern rather complex.

Without any main gas flow (Figure 4.3a), four fully developed symmetrical large vortices can be seen around the wire. When the inlet velocity is increased to 0.1 m/s (Figure 4.3b) the two vortices in the upstream area of channel become smaller and the two other vortices in the downstream area of the channel are stretched in the main gas flow direction. Increasing the inlet velocity to 0.2 m/s (Figure 4.3c), two of the four vortices in the downstream area of the channel are stretched even more in the main flow direction and

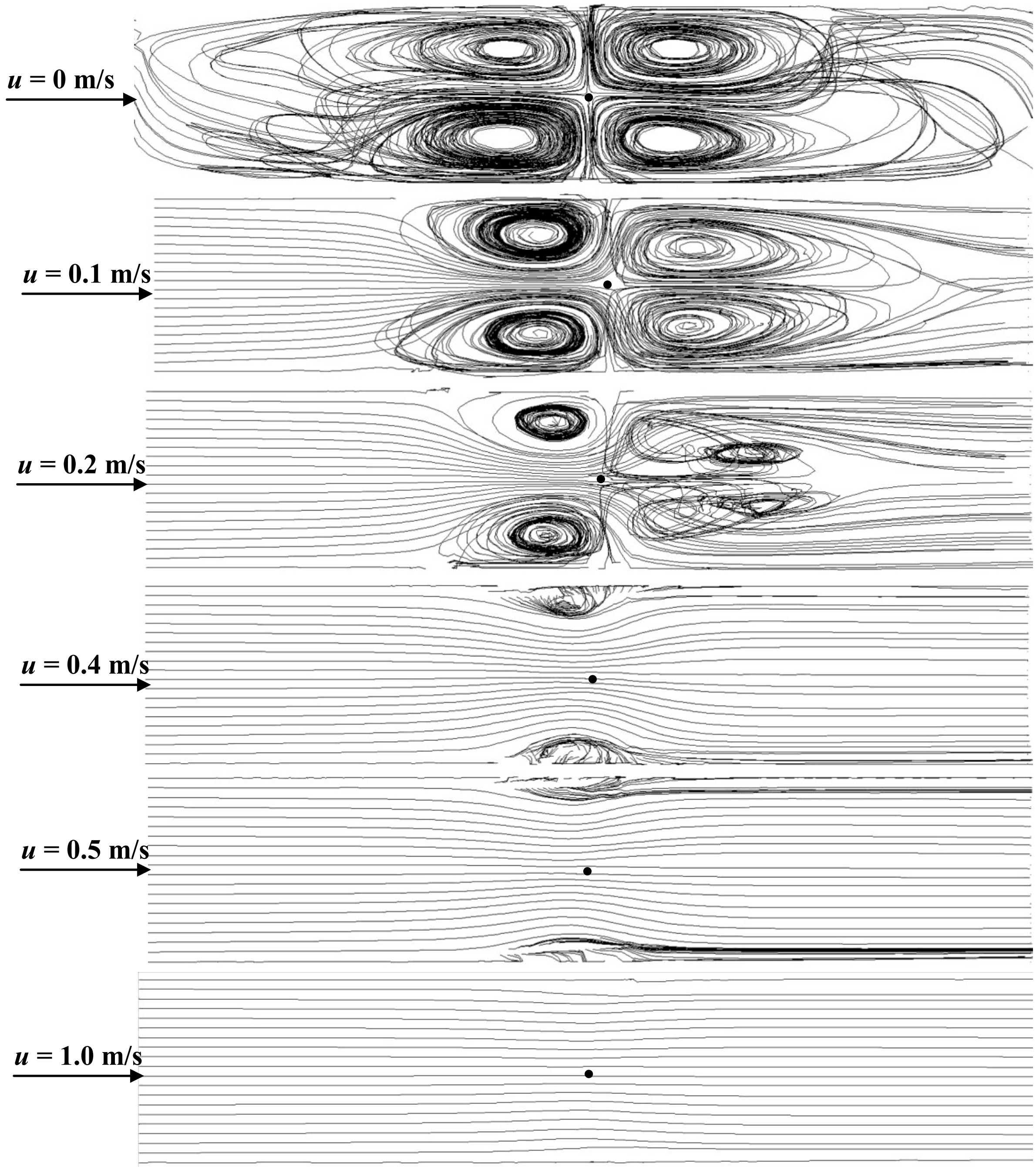

Figure 4.3. Airflow streamlines originated in symmetry plane $z = 0$ for different inlet velocities.

become much weaker. By increasing the inlet velocity to 0.4 m/s (Figure 4.3d) two small vortices appear close to the collecting plates and with further increase of inlet velocity to 0.5 m/s (Figure 4.3e), these two vertices near the collecting plates get even smaller. When the inlet velocity is increased to 1.0 m/s (Figure 4.3f), the effect of EHD flow becomes negligible and the main airflow pattern, which the central part of the channel is practically uniform, dominates.

4.3.3 Particle charging, trajectories and deposition

In this analysis the particle trajectories and particle collection efficiency for various particle sizes (1, 5, 10 and 50 μm diameter) were computed, assuming the turbulent air flow model with turbulent intensity of 5% at the inlet. A total of 400 stochastic neutral particles streams corresponding to 1.4e11, 1.1e9, 1.4e8 and 1.1e6 number of particles per second for each particle size were released respectively from the inlet surface with their initial velocity equal to main airflow velocity (1.0 m/s). The particles are charged by corona bombardment as they move through the channel and are exposed to electrostatic and mechanical forces, resulting in different trajectories. Particle trajectories were calculated with the aid of DPM option in FLUENT along with the corresponding UDFs to compute the electrostatic and mechanical forces acting on the particles. Consequently, some particles are deposited on the collecting plates and some escape from the outlet. The operating parameters are summarized in Table 4.1.

Table 4.1. Operating parameters of the ESP model and particle characteristics

Gas and particles velocity at inlet	1.0 [m/s]
Electric potential at wire	+30 [kV]
Particle diameter	1,5,10,50 [μm]
Total particles mass flow rate	0.0006 [kg/s](= 6 [gr/m^3] concentration)

Due to the very small particle concentration the particle space charge was assumed to be negligible. Therefore, the particle interaction with the airflow and electrostatic fields was not considered. Figure 4.4a shows trajectories of the 50 μm diameter particles. Each particle trajectory in a steady flow calculation represents a "stream" of many particles that flow along the same path. The particles obtain electric charge as they move through the channel and most of them are seen to be trapped in the vicinity of corona wire on the collecting plates. Particle accumulation rates on the collecting plates were computed in the corresponding UDF as the particle stream strikes the surface of collecting plates using the following formula:

$$R_{\text{Accumulation}} = \sum_{p=1}^{N_{particles}} \frac{\dot{m}_p}{A_{face}} \tag{4-1}$$

where $\dot{m}_p$ is the particle stream mass flow rate, A_{face} is the area of cell face at the collecting plates. The rate of increase in the depth of particle accumulation on the collecting plates was obtained by simply dividing the accumulation rate by the particle mass density in Eq. (4-2) and the result is shown in Figure 4.4b.

$$D_{Accumulation} = \frac{R_{Accumulation}}{\rho_p} \tag{4-2}$$

The brightest points in Figure 4.4b indicate that the largest particle accumulation is located on the collection plate slightly upstream from the wire electrode. The deposited particles on the collecting plates have different charge to mass ratios as shown in the histogram in Figure 4.4c. In this case, about 35% of the deposited particles have charge to mass ratio between 0.6-0.8 [mC/kg] and less than 5% of the deposited particles have either very large or very small values. Therefore, very few particles with small charge to mass ratios are deposited on the collecting plates at the beginning of the channel and very few with large value of charge to mass ratios are deposited in the vicinity of corona wire on the collecting plates. On the other hand, Figure 4.4d clarifies the relation between the average charge to mass ratio and the ultimate position of deposited particles in the *x* direction on the collecting plates. Due to the symmetry of the problem since the effect of the gravitational forces on the particles is negligible, only the upper surface of the collecting planes is considered in this Figure. Figure 4.4d shows percentage of captured particles at different locations on the upper plane in the *x* direction, where $x = 0$ is the position of wire electrode. Each column in this Figure indicates the number of accumulated trapped particles in a particular space interval on the upper plane and the number above each column shows the average charge to mass ratio [C/kg] of the deposited particles in that area. According to this Figure, particles receive more charge as they enter the high electric field intensity zone in vicinity of the corona wire and more particles are collected in this area rather than at the very beginning of the channel, where particles have negligible charge. The areas with high concentration of deposited particles in Figure 4.4d also verify the depth of particle accumulation pattern obtained in Figure 4.4b. The model predicts a collection efficiency of 100% for 50 μm particles and the total deposited mass on the upper and lower surfaces of collecting planes are statistically about the same due to the symmetry of the problem. The numerical results are summarized in Table 4.2.

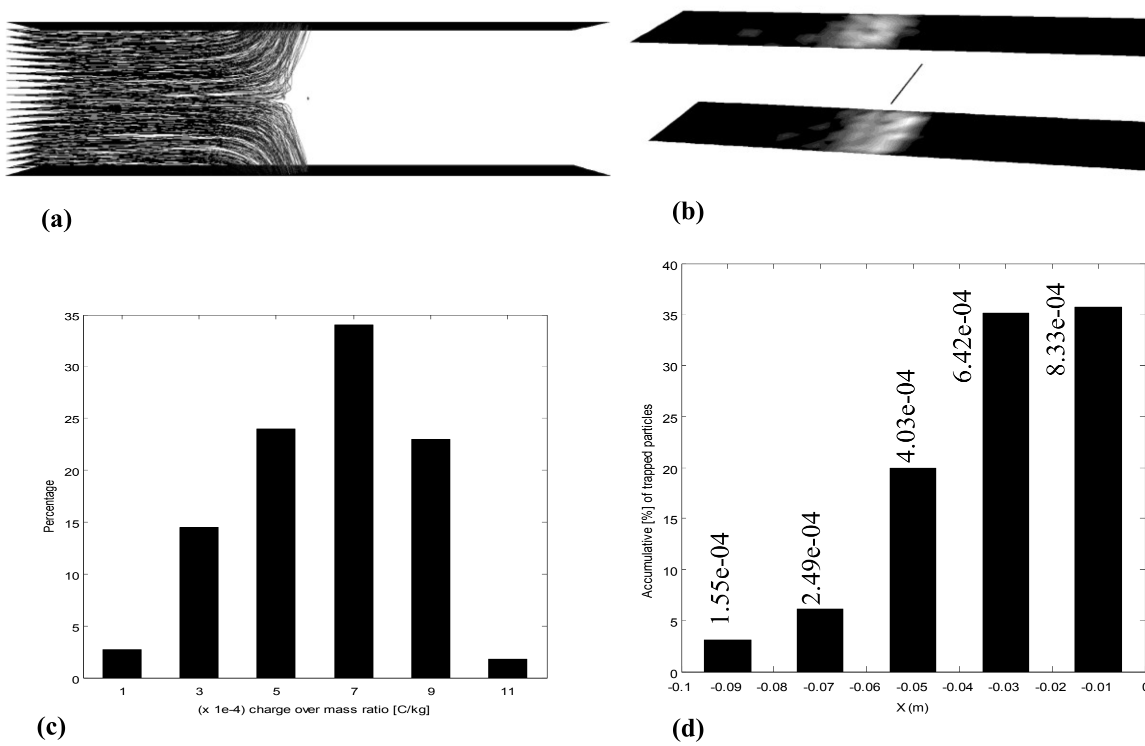

Figure 4.4. Results of numerical simulation for precipitation of 50 μm particles assuming the inlet velocity of 1.0 m/s (a) particle trajectories, (b) particle accumulation on collecting plates, (c) charge to mass ratio distribution of collected particles, (d) accumulative percentage of particles captured on the upper plane along with average charge to mass ratio.

Similar simulations were done for 10 μm diameter particles and the numerical results are shown in Figure 4.5a - Figure 4.5d. There is a significant difference between Figure 4.5a and Figure 4.4a as some particle trajectories are extended further through the channel before terminating on the wall downstream of the wire electrode. According to Table 4.2, in this case only 3 of 400 particles escape from the outlet and the collection efficiency is 99.2%. The largest depth of particle accumulation on the collecting plates are in the areas adjacent to the corona wire (Figure 4.5b) and about 50% of the deposited particles have charge to mass ratio between 4 and 5 [mC/kg] (Figure 4.5c). Figure 4.5d shows a high concentration of deposited particles in the vicinity of corona wire on the upper surface of the collecting planes, which confirms the results shown in Figure 4.5b and Figure 4.5c.

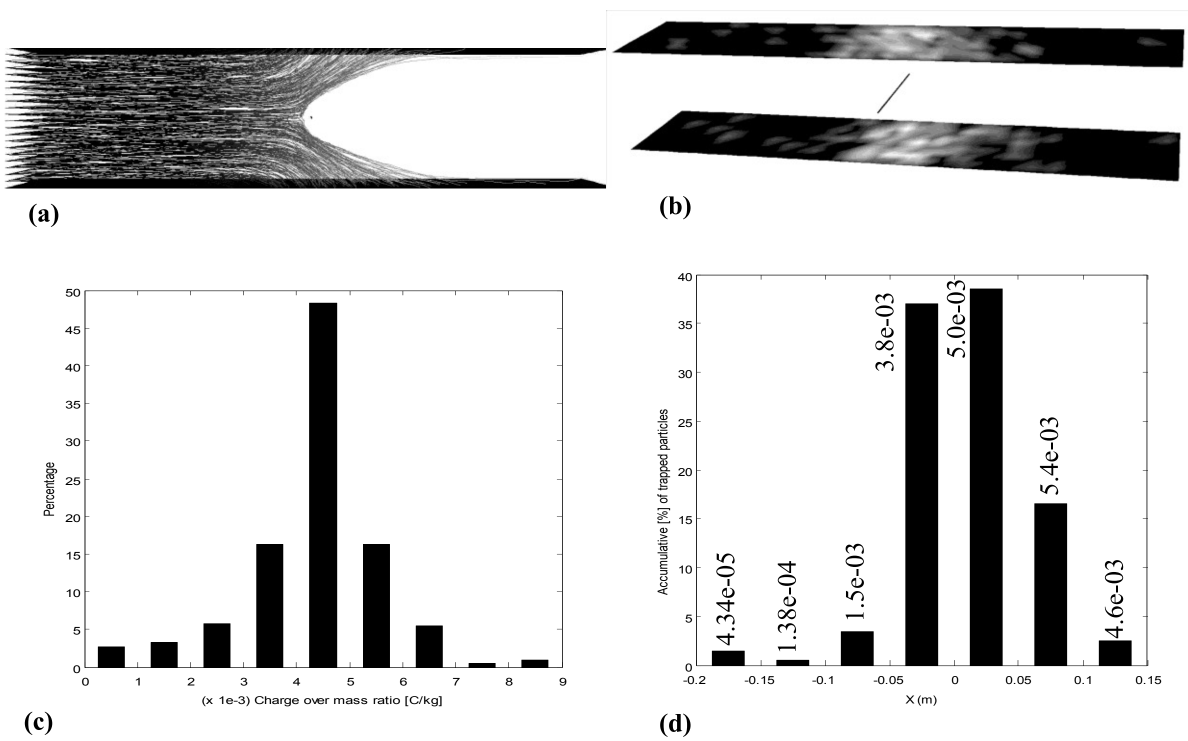

Figure 4.5. Results of numerical simulation for precipitation of 10 μm particles assuming the inlet velocity of 1.0 m/s (a) particle trajectories, (b) particle accumulation on collecting plates, (c) charge to mass ratio distribution of collected particles, (d) accumulative percentage of particles captured on the upper plane along with average charge to mass ratio.

Decreasing the particle size to 5 μm and 1 μm (Figure 4.6a and Figure 4.7a) show that more particles escape from the outlet and the collection efficiency is decreased to 58% and 14.5%, respectively. According to Figure 4.6b and Figure 4.7b, the largest depth of particle accumulation is still in the areas on the collecting plates adjacent to the corona wire. About 60% of the deposited particles have a charge to mass ratio between 8 and 10 [mC/kg] for 5 μm particles (Figure 4.6c) and almost 45% of the deposited particles have a charge to mass ratio of 40-50 [mC/kg] for 1 μm particles (Figure 4.7c). As was expected from the existing experimental results presented in the literature, for the same inlet velocity and voltage applied to the corona wire, smaller particles will go further through the channel before being trapped on the collecting plates. In comparison with large particles, small particles collect less charge as they pass through the ESP channel and particle trajectories are primarily influenced by the air drag forces - the electrostatic forces have much weaker effect in this case. Therefore, the drift velocity of such particles is small and they practically follow the gas streamlines. Figure 4.6d and Figure 4.7d verify that most of the particles are still deposited on the deposited planes in the high electric field zone close to the wire. The numerical results for the last two cases are also summarized in Table 4.2.

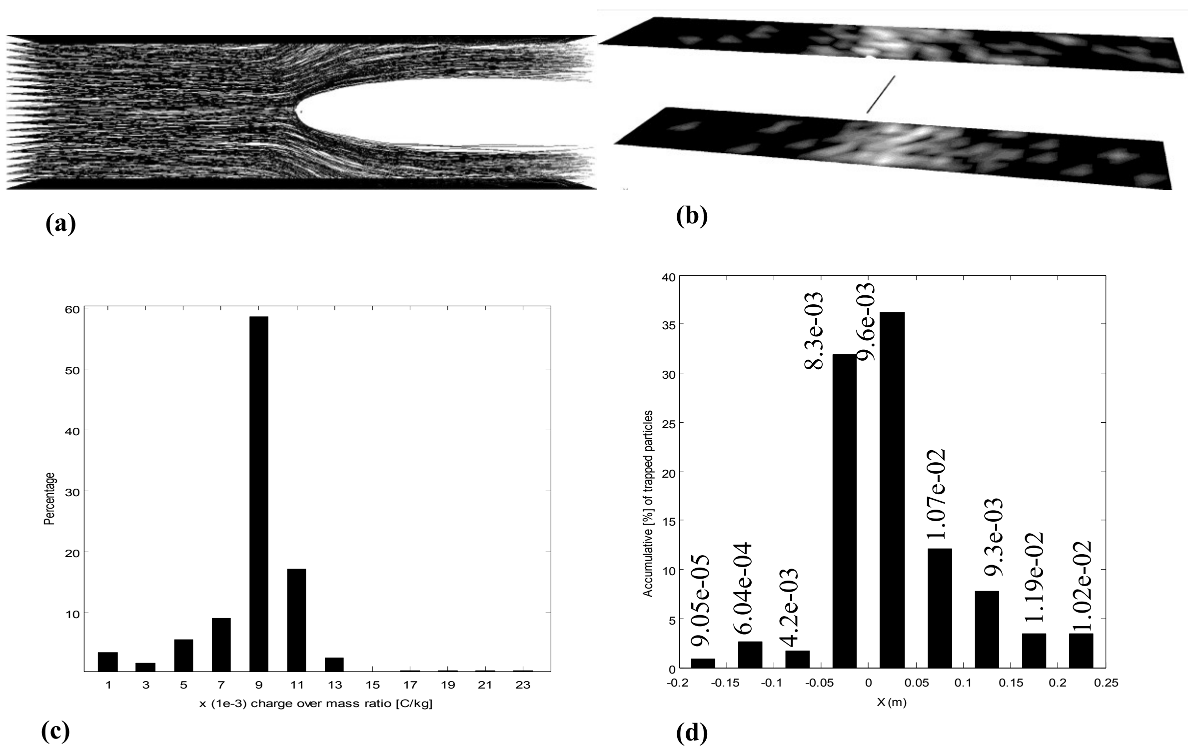

Figure 4.6. Results of numerical simulation for precipitation of 5 μm particles assuming the inlet velocity of 1.0 m/s (a) particle trajectories, (b) particle accumulation on collecting plates, (c) charge to mass ratio distribution of collected particles, (d) accumulative percentage of particles captured on the upper plane along with average charge to mass ratio.

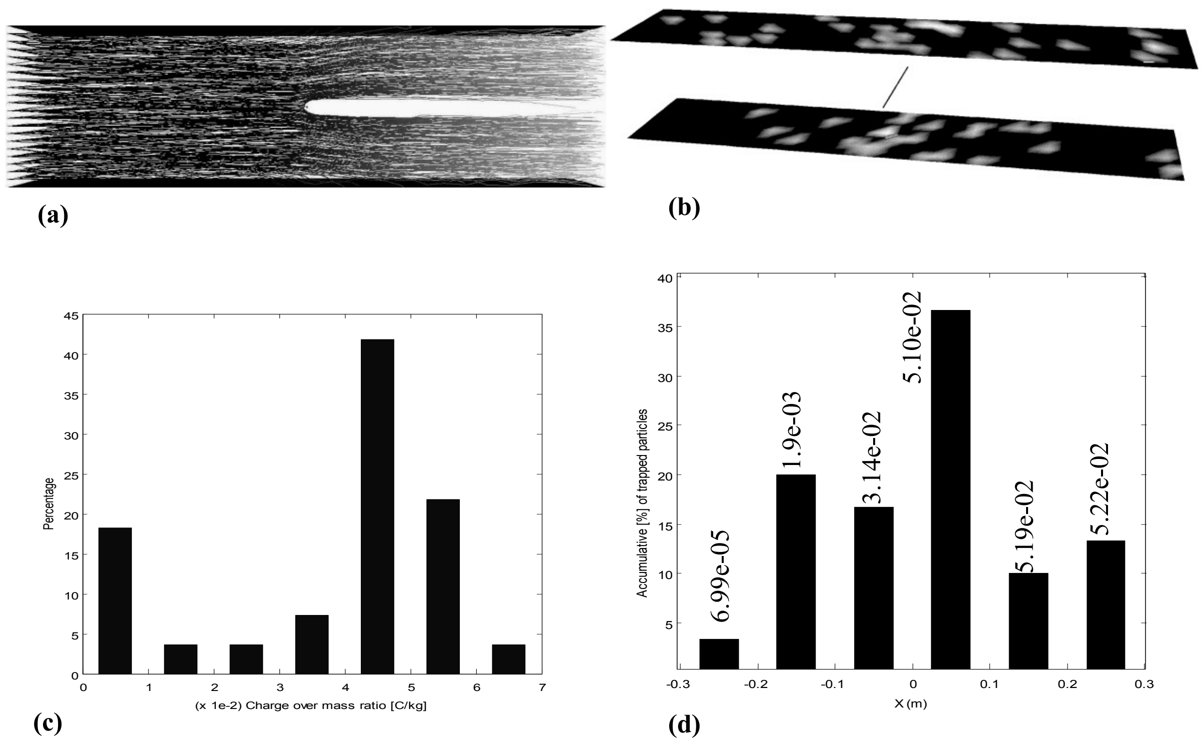

Figure 4.7. Results of numerical simulation for precipitation of 1 μm particles assuming the inlet velocity of 1.0 m/s (a) particle trajectories, (b) particle accumulation on collecting plates, (c) charge to mass ratio distribution of collected particles, (d) accumulative percentage of particles captured on the upper plane along with average charge to mass ratio.

In order to investigate the effect of the inlet velocity on the collection efficiency for 1 μm particles, the inlet velocity is decreased to 0.5 m/s and the results are shown in Figure 4.8a - Figure 4.8d. By decreasing the inlet velocity (which increases the particle residence time in the channel) the collection efficiency is increased from 14.5% up to 30.5%.

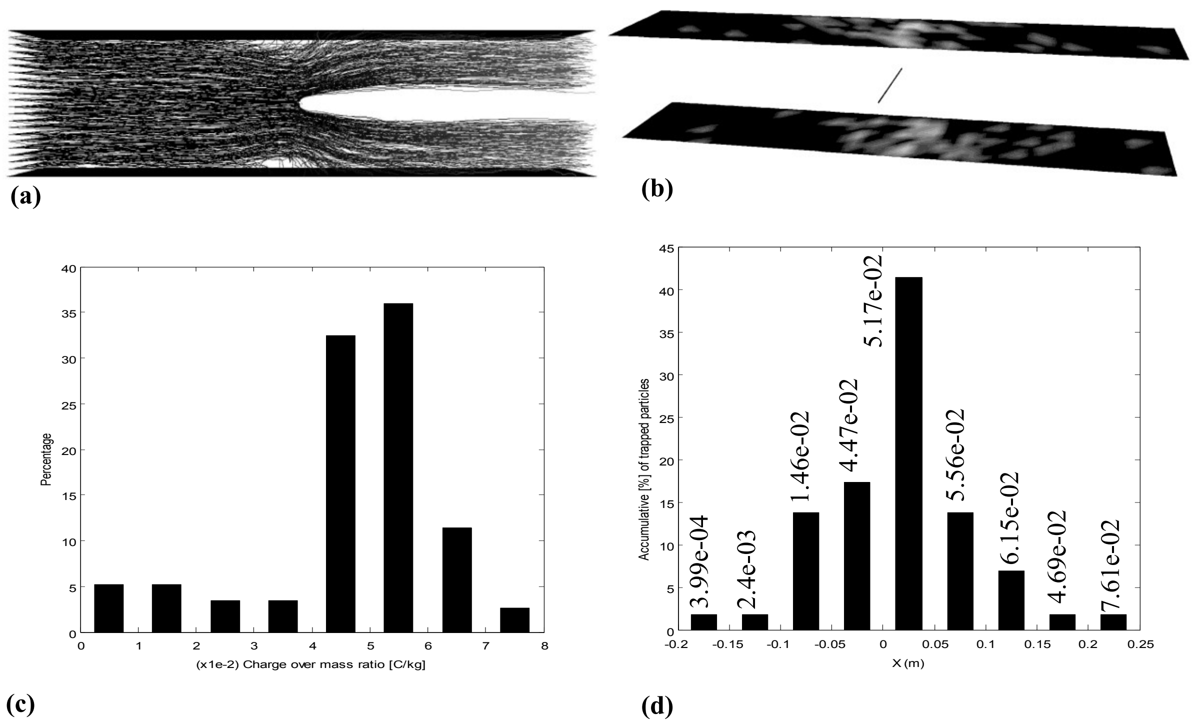

Figure 4.8. Results of numerical simulation for precipitation of 1 μm particles assuming the inlet velocity of 0.5 m/s (a) particle trajectories, (b) particle accumulation on collecting plates, (c) charge to mass ratio distribution of collected particles, (d) accumulative percentage of particles captured on the upper plane along with average charge to mass ratio.

Table 4.2. Results summary

Inlet velocity	Diameter	Trapped	Escaped	Efficiency	Upper-plane (kg/s)	Lower-plane (kg/s)
1.0 m/s	50µm	400	0	100%	2.94e-4	3.06e-4
1.0 m/s	10µm	397	3	99.25%	3.0e-4	3.0e-4
1.0 m/s	5µm	232	168	58%	1.74e-4	1.74e-4
1.0 m/s	1µm	58	342	14.5%	4.5e-5	3.75e-5
0.5 m/s	1 µm	122	278	30.5%	8.7e-5	8.4e-5

4.3.4 EHD flow effect on ESP performance

Secondary EHD flow effect on particle collection efficiency has been a subject of many discussions, sometimes leading to contradictory conclusions. Figure 4.9a and Figure 4.9b show the particle trajectories for 1 µm particles for two cases: with and without EHD flow, assuming 0.5 m/s as the inlet velocity. Simulation results show a 2% improvement in collection efficiency by considering the secondary EHD flow.

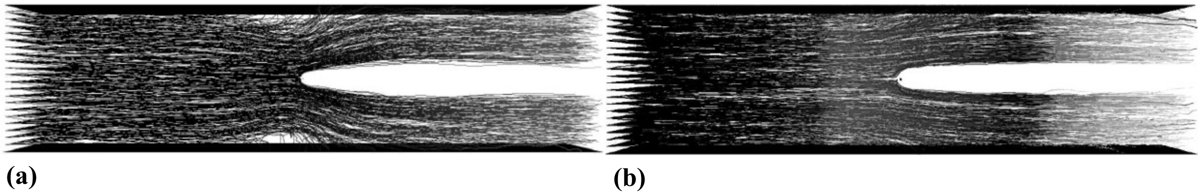

(a) **(b)**

Figure 4.9. Particle trajectory for 1µm particles, inlet velocity 0.5 m/s (a) without EHD flow (b) with EHD flow.

The same analysis was repeated for 5, 10 and 50 μm particles, where the collection efficiency was calculated and compared for the two cases. According to Table 4.3, the particle collection efficiency increase in case 2 for 5 μm particles is even smaller than for 1 μm particles and the EHD flow has no effect for larger particles. Therefore, the EHD flow shows a slight increase on the particle collection efficiency for very small particles only and, in general, has a negligible influence on the overall particle collection efficiency which is in good agreement with the results obtained in [17].

Table 4.3. Comparison of particle collection efficiency for inlet velocity of 0.5 m/s

Particle diameters	1μm	5μm	10μm	50μm
Case1: without EHD	28.5%	98.75%	100%	100%
Case2: With EHD	30.5%	99.5%	100%	100%

4.3.5 Particle concentration effect on ESP performance

A wide range of particle sizes (0.3 - 90 μm) at the inlet was considered, which gives a good representation of poly-dispersed particle movement in an ESP. Particle size distribution was assumed to be lognormal, as given by Herdan [112]:

$$f(d) = \frac{1}{d \ln \sigma_g (2\pi)^{0.5}} \exp[-\frac{(\ln d - \ln d_g)^2}{2 \ln^2 \sigma_g}] \tag{4-3}$$

where $\int_0^\infty f(d) \mathrm{d}d = 1$, the geometric mean diameter d_g=5.03 μm and the geometric standard deviation σ_g=1.73 (Figure 4.10), which results from the measured data [53]. The lognormal size distribution function was divided into 18 fractions and integrated to obtain the mass flow rate percentage of each discrete particle size distribution as shown in Figure 4.11.

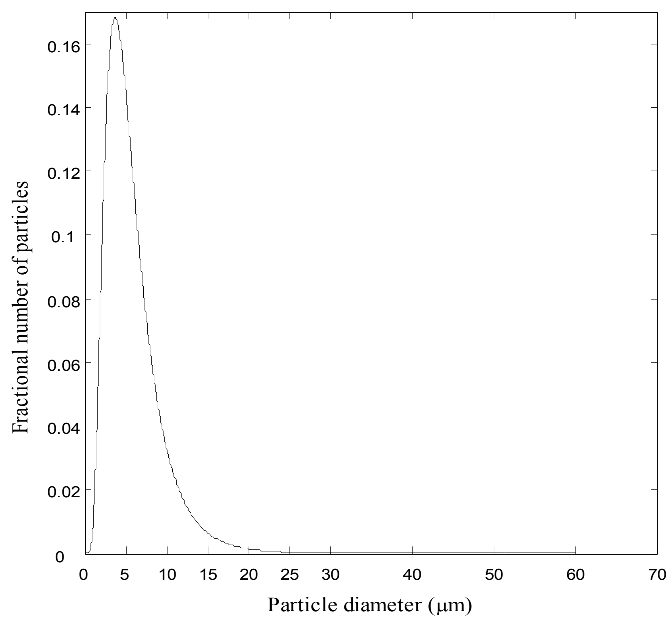

Figure 4.10. Lognormal particle size distribution.

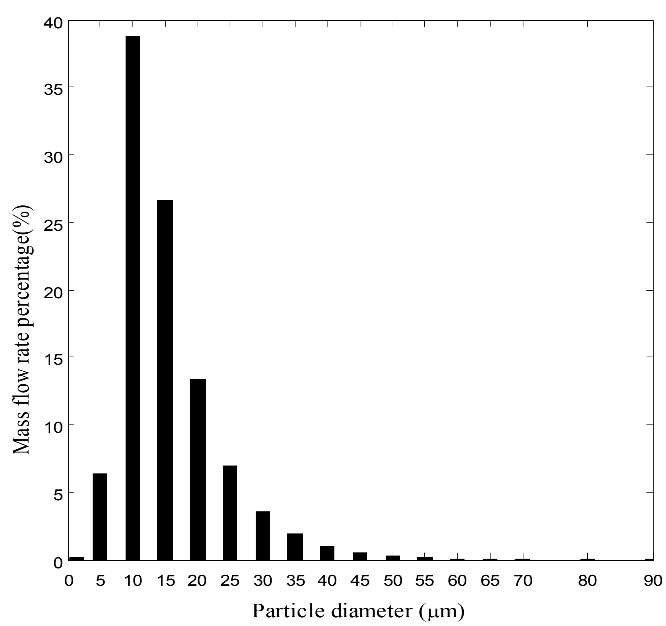

Figure 4.11. Distribution of mass flow rate versus particle size at inlet.

In the investigated model, the initial particle velocity of 1 m/s was assumed for all particles. The mean diameter and mass flow rate values of each fraction were determined separately in the DPM model of FLUENT. The governing equations of particle charging and motion for each particle fraction were solved simultaneously. The total particle space charge density was obtained by superposition of the charge densities of different fractions. The total particle mass flow rate is expressed in terms of the reference value of c_0 = 1.0e-5 kg/s. The simulations were carried out for a range of particle mass flow rates: 0.5c_0, 2c_0, 10c_0 and 20c_0 kg/s at the constant primary flow velocity (1 m/s) and the corona wire voltage (+30 kV). All the coupled processes occurring inside a typical ESP: gas flow, particle dynamics and electrostatics, were considered.

4.3.5.1 Air flow patterns and particle characteristics for $c = 0.5c_0$

At the lowest particle mass flow rate ($c = 0.5c_0$), the flow velocity contours and the corresponding flow streamlines in a plane placed perpendicularly to the wire electrode at its half length (Figure 4.12a and Figure 4.12b) show the laminar pattern, which could be expected from the values of Reynolds and EHD numbers ($Re_{(wire)}$ = 63.7, $EHD_{(wire)}$ = 4202.8 [8]). The average streamlines in Figure 4.12b are nearly parallel to the walls with tiny von Karman vortices behind the corona wire which are too small to be visible. It is clearly visible that the particle space charge hardly modifies the airflow pattern in this case and the effect of particle presence on velocity fluctuation could be ignored.

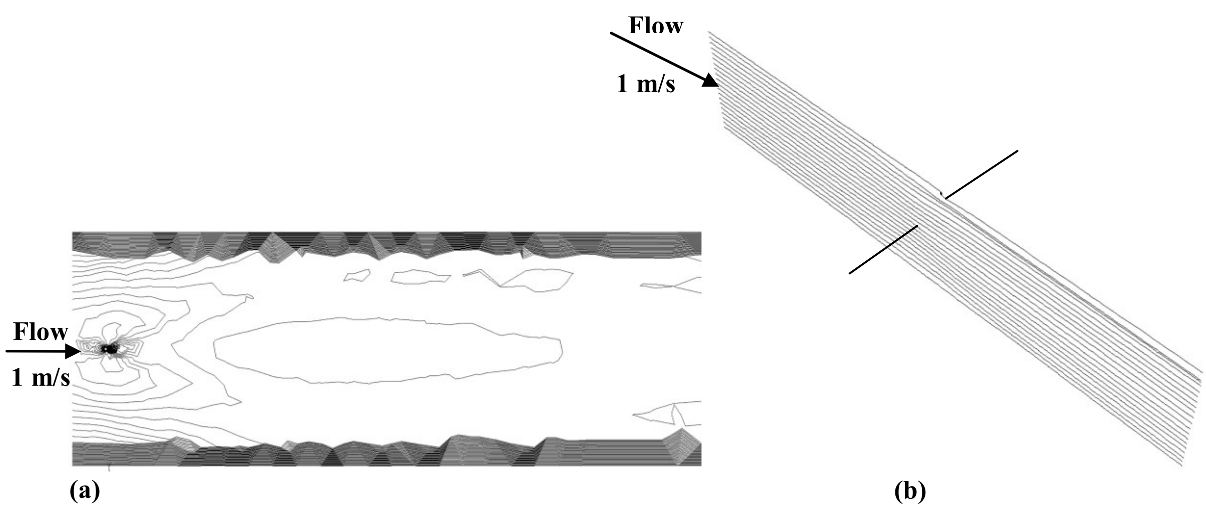

Figure 4.12. Air velocity patterns in z = 0 symmetry plane of ESP (a) contours of velocity magnitude, maximum velocity is 1.39 m/s close to the electrode and number of contours is 50 (b) flow streamlines (particle mass flow rate $c = 0.5c_0$, corona wire voltage +30 kV).

Figure 4.13a - Figure 4.13c show a selected number of particle trajectories released from the same starting points for three different particle sizes: 1.4 µm, 5 µm, and 10 µm, assuming

$c = 0.5c_0$ as the total mass flow rate of particles. Note that the shown paths are mean tracks, while in the calculations a stochastic calculator was activated to take into consideration the turbulence oscillations of individual paths around an average route. For very small particles (1.4 μm – Figure 4.13a), air drag forces have a stronger effect than electrostatic forces, so they mostly follow the flow paths moving first towards the corona wire and then are slightly pushed back to the collecting plates. However, the bigger particles (5 μm and 10 μm - Figure 4.13b and Figure 4.13c) obtain more charge and are driven to the deposition planes with stronger electrostatic forces especially in the areas close to the corona wire. In this case the particle trajectories are much shorter, most particles are trapped and only a few of them escape from the outlet.

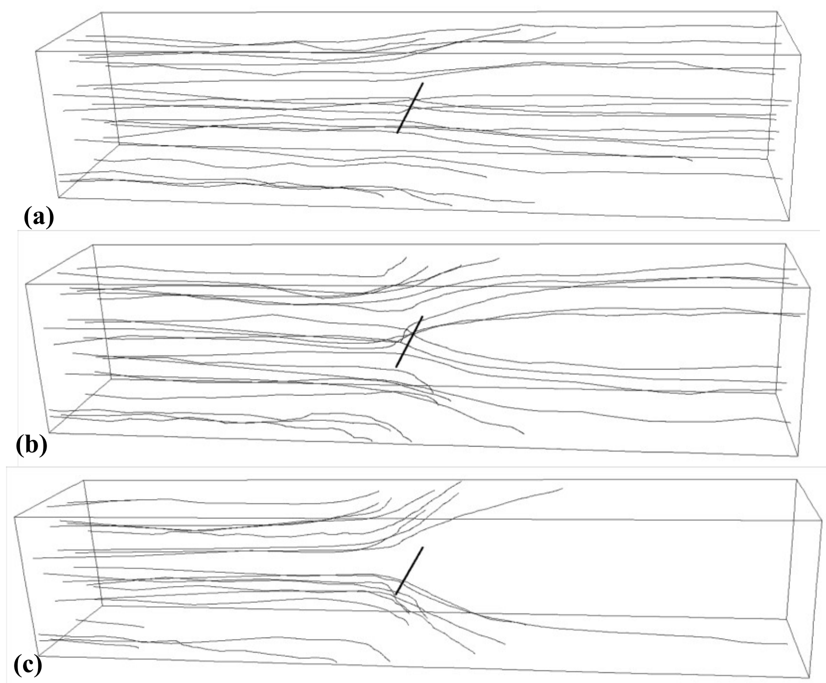

Figure 4.13. Particle trajectories for three particle sizes: (a) 1.4 μm, (b) 5 μm, (c) 10 μm (particle mass flow rate $c = 0.5c_0$, corona wire voltage +30 kV).

The particle concentration pattern in z = 0 symmetry plane is shown in Figure 4.14a, where the dark color indicates areas with low particle concentration and the bright color shows areas with a relatively high particle concentration. Behind the wire in the downstream direction, the particles are driven towards the collecting plates by the electric forces and a narrow dark trail with bright borders is produced in this region, which confirms the experimental results obtained by Mizeraczyk and his co-workers [20]. Due to stronger electrostatic forces acting on particles in the areas close to the corona wire, more particles are collected in this region as it is shown in the deposition pattern (Figure 4.14b). The brighter color in this Figure shows the higher particle accumulation on the deposition planes. Figure 4.14c shows the percentage of trapped particles of three different sizes (1.4, 5 and 10 μm) on the collecting plates in 10 intervals along the length of the channel in *x* direction. As expected, regardless of particle size, more particles are trapped in vicinity of the corona electrode (-0.05 m<*x*<0.05 m) and less are trapped at the beginning and end of the channel. Increasing the particle size from 1.4 to 10 μm, the percentage of particles trapped in the areas close to the wire is increased as well. Due to a non-uniform distribution of electric field and space charge density, particles have different trajectories and charging rates, especially when they are in vicinity of the corona wire. The average values of charge to mass ratio at the deposition position of the three different particle sizes are compared in each interval as shown in Figure 4.14d. It is obvious that the particles collected closer to the inlet have a small value of charge and as they pass through the channel they obtain more charge.

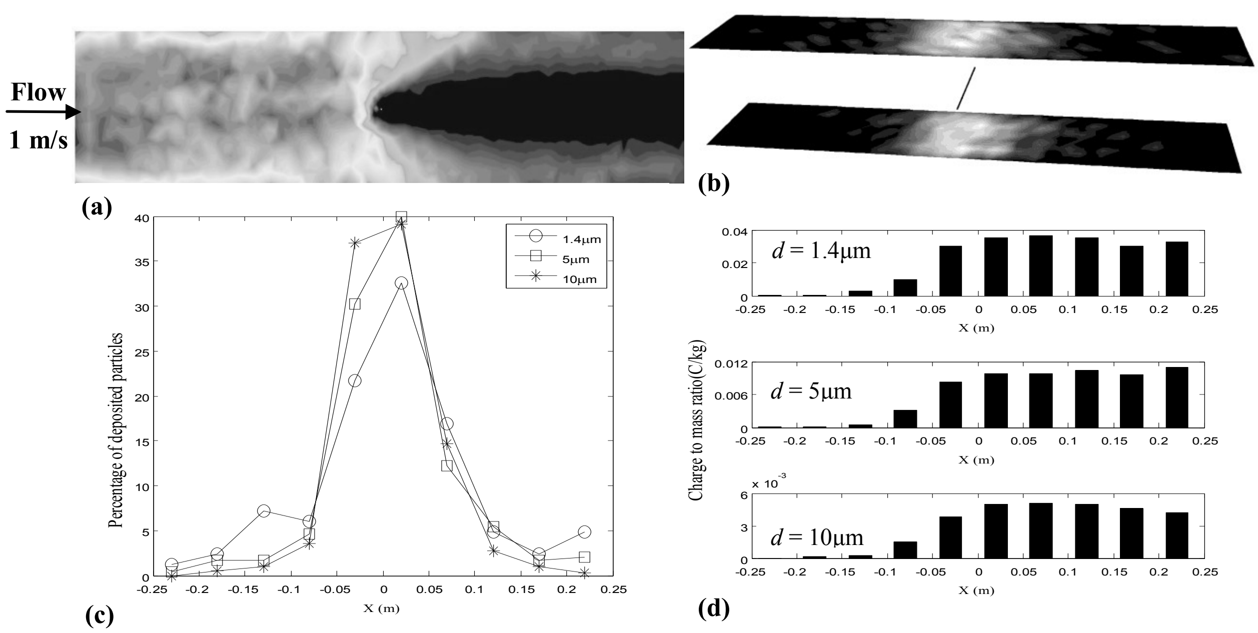

Figure 4.14. Particle transport and deposition for the particle mass flow rate $c = 0.5c_0$ and corona wire voltage +30 kV (a) particle concentration (b) deposition pattern on the collection plates (c) collection performance and (d) charge to mass ratio along the channel, for three particle sizes: 1.4, 5 and 10 μm.

4.3.5.2 Air flow patterns and particle characteristics for $c = 2c_0$

After a four times increase in the particle mass flow rate ($c = 2c_0$), no dramatic changes can be observed in the velocity contours and the generated velocity fluctuations are weak (Figure 4.15).

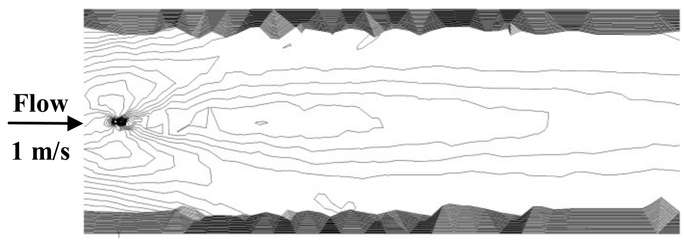

Figure 4.15. Velocity contours in $z = 0$ symmetry plane (maximum velocity is 1.4 m/s close to the electrode, number of contours is 50, particle mass flow rate $c = 2c_0$ and corona wire voltage +30 kV).

Comparing the particle concentration pattern in Figure 4.16a with Figure 4.14a, the dark trail is getting slightly wider, pushing more particles towards the deposition planes in the downstream direction. Figure 4.16b also shows a higher particle collection in the intervals close to the corona wire. The higher percentage of deposited particles of 1.4 μm at the beginning and end of the channel verify the random movement of small particles, which have smaller inertia, in the turbulent flow in the channel. The average values of charge to mass ratio for the three different sizes of particles are also shown in Figure 4.16c which follows the same trend as that shown in Figure 4.14c.

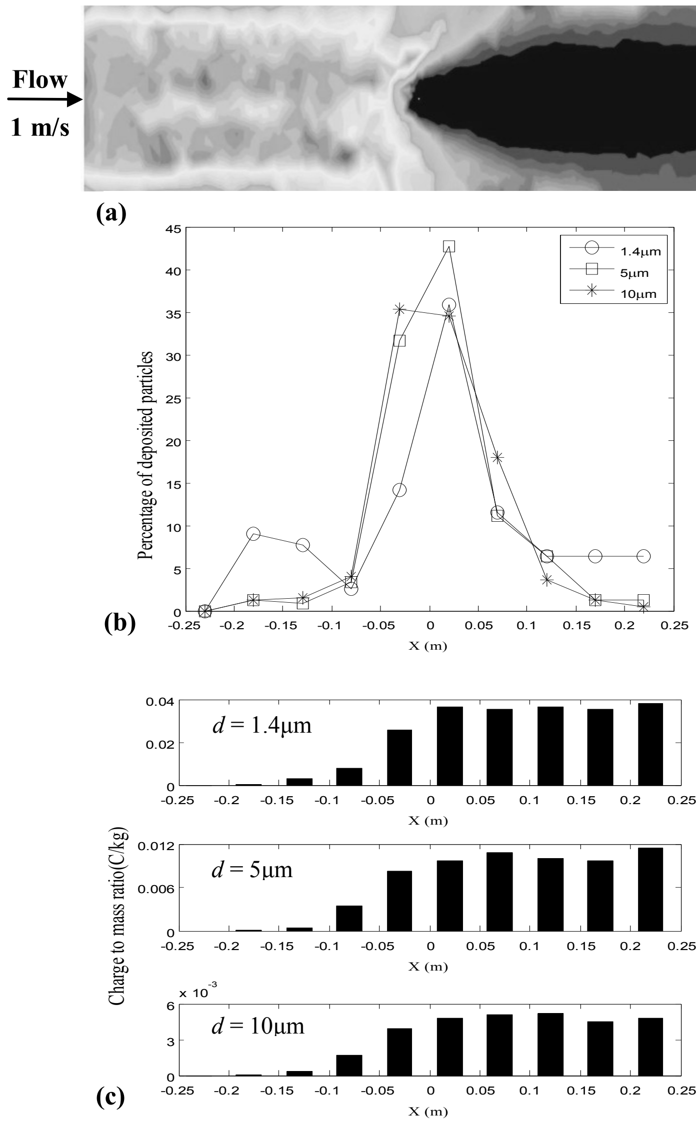

Figure 4.16. Particle transport and deposition for the particle mass flow rate $c = 2c_0$, corona wire voltage +30 kV and three particle sizes: 1.4, 5 and 10 μm (a) particle concentration (b) collection performance and (c) charge to mass ratio along the channel.

4.3.5.3 Air flow patterns and particle characteristics for $c = 10c_0$

After the particle mass flow rate has been increased 20 times comparing to the original value ($c = 10c_0$), some velocity fluctuations start to appear in the downstream direction. In order to show this effect better the velocity contours are shown not only in the $z = 0$ symmetry plane (Figure 4.17a), but in several planes parallel to the corona wire along the length of the channel as well (Figure 4.17b). This pattern is not constant and fluctuates with time. Figure 4.18 shows that the flow streamlines in $z = 0$ symmetry plane are mostly parallel to the walls in upstream direction, but a very narrow oscillating wake is generated behind the wire in downstream direction, which expands slightly towards the channel outflow end.

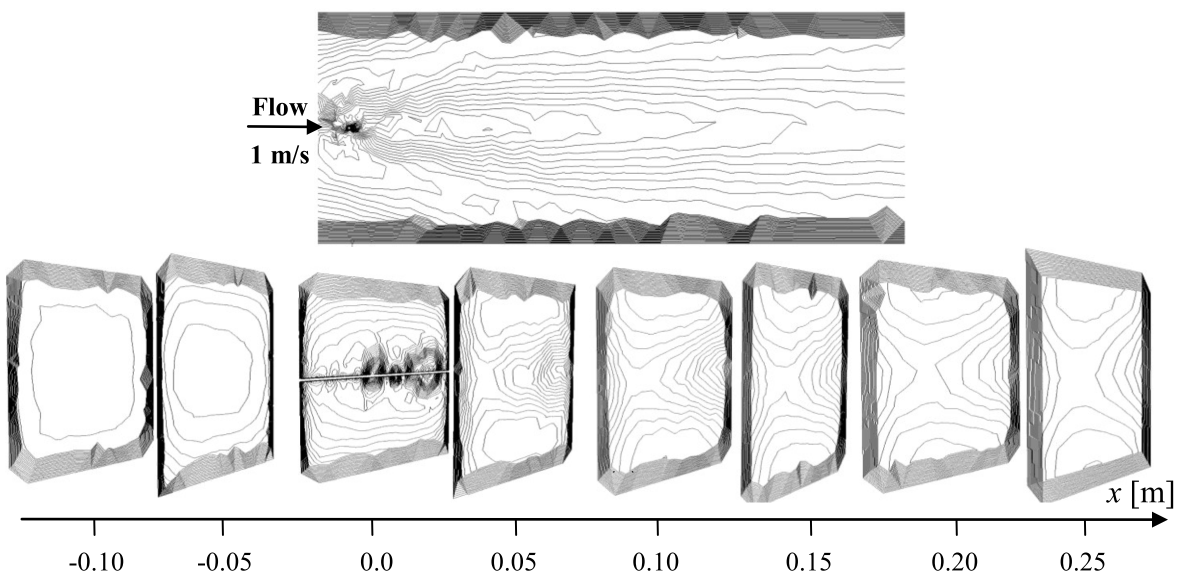

Figure 4.17. Velocity contours for the particle mass flow rate $c = 10c_0$ and corona wire voltage +30 kV (a) $z = 0$ symmetry plane (maximum velocity 1.4 m/s is close to the electrode, number of contours is 50) and (b) planes parallel to the corona wire along the channel.

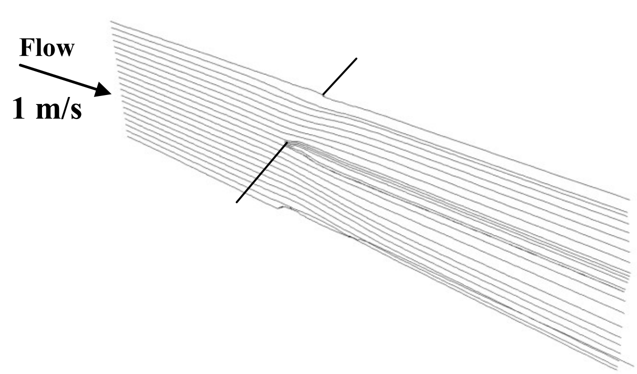

Figure 4.18. Flow streamlines beginning in $z = 0$ symmetry plane (particle mass flow rate $c=10c_0$, corona wire voltage +30 kV).

The particle trajectories for the three different particle sizes in Figure 4.19 are very similar to the results obtained in Figure 4.13 assuming a very low particle concentration.

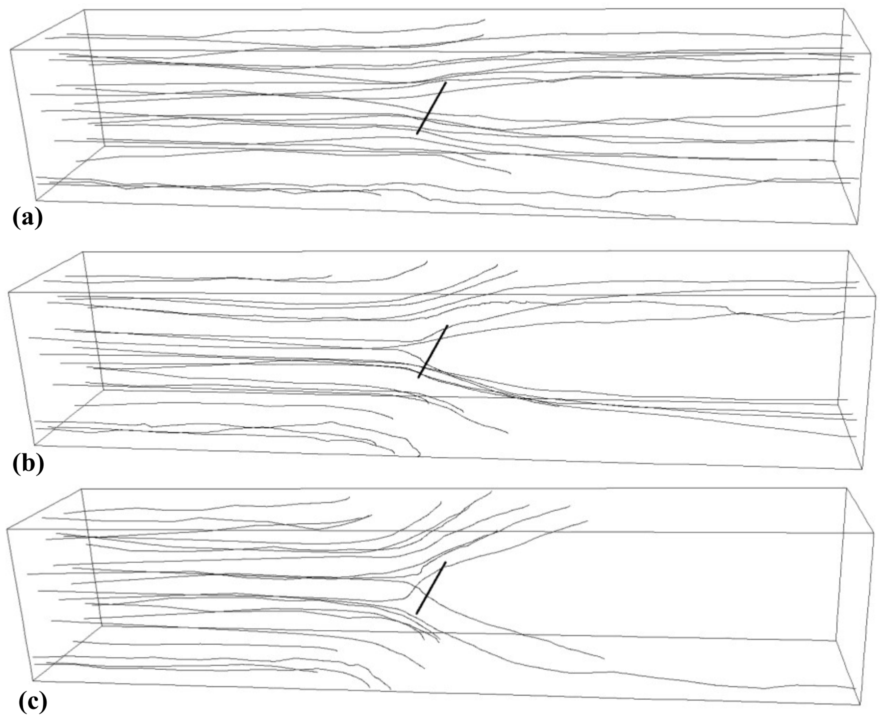

Figure 4.19. Particle trajectories for three particle sizes: (a) 1.4 μm, (b) 5 μm, (c) 10 μm (particle mass flow rate $c = 10c_0$, corona wire voltage +30 kV).

As it is demonstrated in the particle concentration pattern in Figure 4.20a, the black trail in downstream of the channel is getting even wider. The deposition pattern on the collecting plates in Figure 4.20b, the collection performance along the length of channel in Figure 4.20c and the values of average charge to mass ratio in different intervals along the channel in Figure 4.20d also follow a pattern as expected, showing that regardless of various particle concentration these results are very similar in all cases. Comparing Figure 4.20c with Figure 4.14c and Figure 4.16b, an increase in percentage of deposited particles of 1.4 μm in vicinity of the corona wire can be observed, showing increased sensitivity of smaller particles to the generated turbulence in the flow pattern.

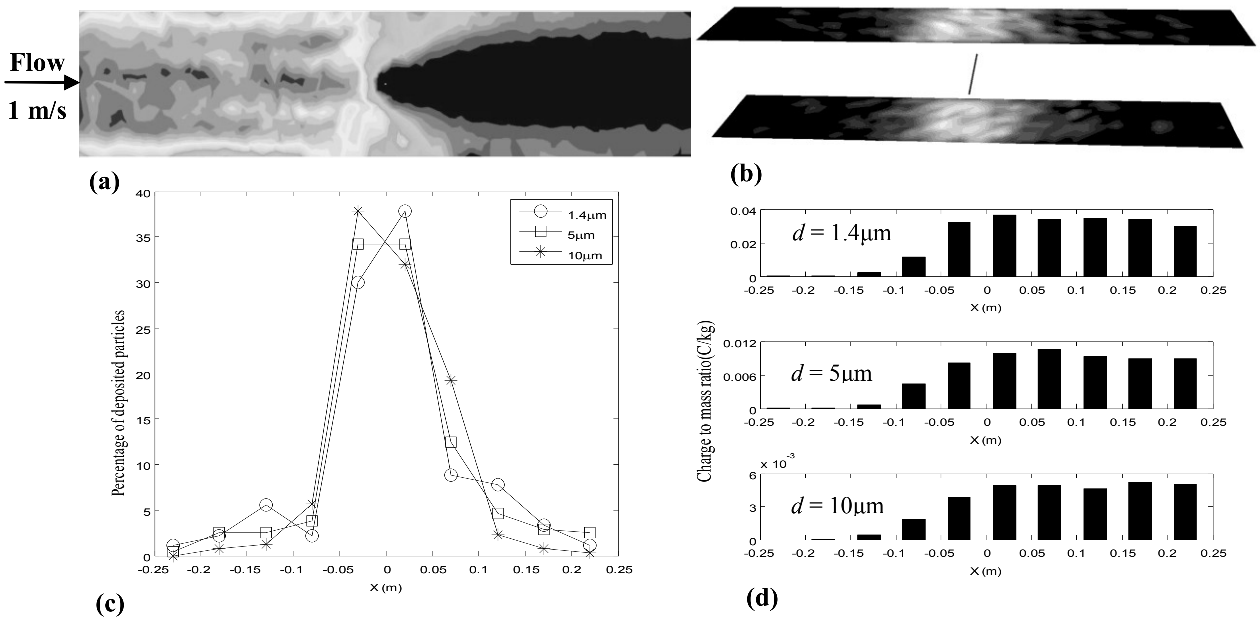

Figure 4.20. Particle transport and deposition for the particle mass flow rate $c = 10c_0$ and corona wire voltage +30 kV (a) particle concentration (b) deposition pattern on the collection plates (c) collection performance and (d) charge to mass ratio along the channel for three particle sizes: 1.4, 5 and 10 μm.

4.3.5.4 Air flow patterns and particle characteristics for $c = 20c_0$

Increase of the particle concentration increases the particle charge density in the channel, which results in significant changes in the electric field distribution and, as a consequence, in the gas flow patterns. At the highest analyzed particle mass flow rate ($c = 20c_0$) the flow disturbance is strongest and high velocity variation is generated in the downstream part of the channel close to the wire, changing the flow aerodynamic conditions as shown in Figure 4.21a - Figure 4.21c, in which the velocity contours are shown in three different stages of the iteration process for better comparison. The velocity contours change dramatically in time and less velocity fluctuation is observed in Figure 4.21c than Figure 4.21a. Figure 4.22a - Figure 4.22c show the corresponding flow streamlines for the three different stages of the iteration process as well.

The flow streamlines in Figure 4.22a demonstrate a very unsteady turbulent flow with violent oscillations along the channel. The flow streamlines are modified in time, as shown in Figure 4.22b and Figure 4.22c, and represent less turbulent behavior.

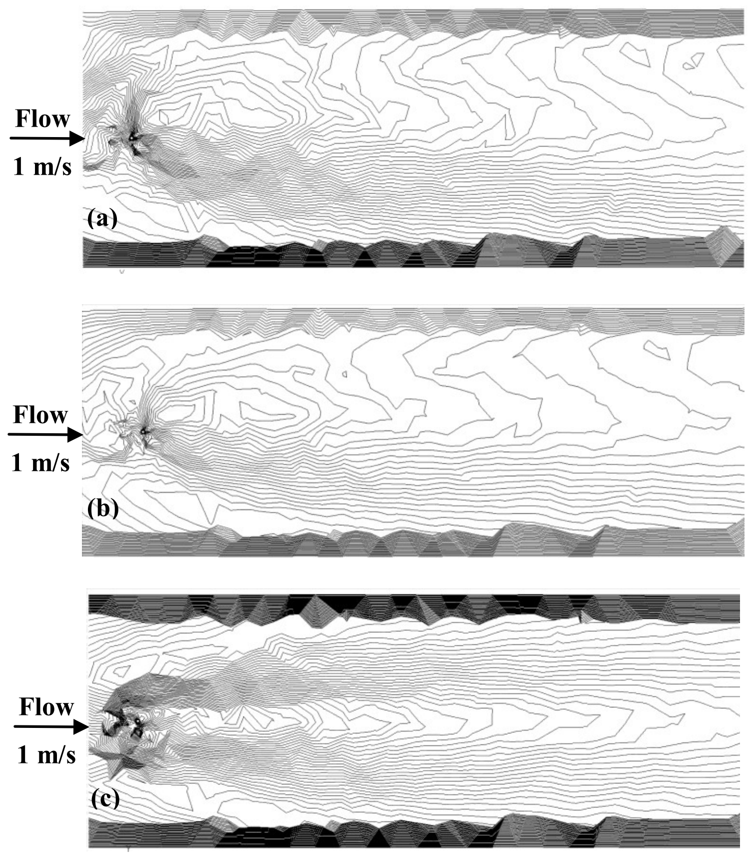

Figure 4.21. Velocity contours in $z = 0$ symmetry plane for three different stages of the iteration process. The maximum velocity close to the electrode is (a) 1.8 m/s (b) 1.5 m/s and (c) 1.3 m/s and number of contours is 50 (particle mass flow rate $c = 20c_0$, corona wire voltage +30 kV).

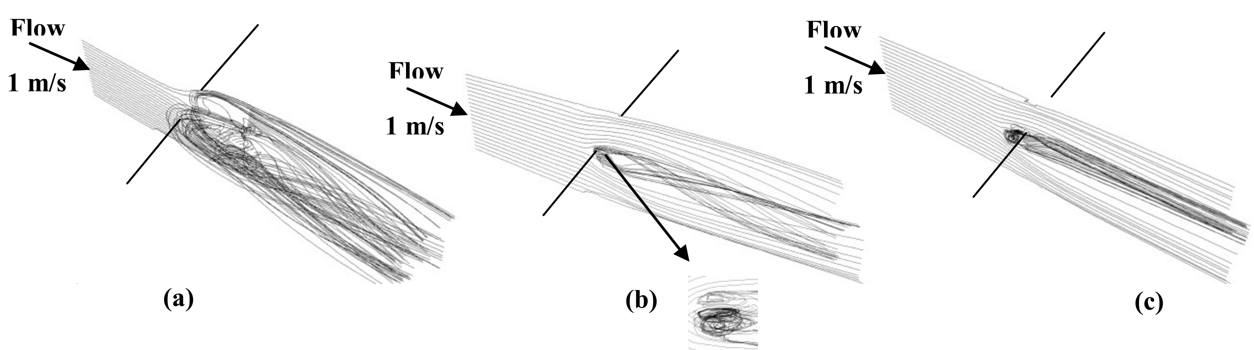

Figure 4.22. Airflow streamlines in $z = 0$ symmetry plane for three different stages of the iteration process. (particle mass flow rate $c = 20c_0$, corona wire voltage +30 kV).

By increasing the particle concentration, the dark area behind the corona wire (particle free region) in the particle flow pattern spreads out more widely due to flow turbulence and covers almost the whole height of the ESP, as was also experimentally reported in [20], strongly driving the particles towards the deposited planes (Figure 4.23). For the three different stages of the iteration process, significant changes in the particle concentration patterns are also observed as shown in Figure 4.23a - Figure 4.23c, which correspond to changes in time of the flow pattern.

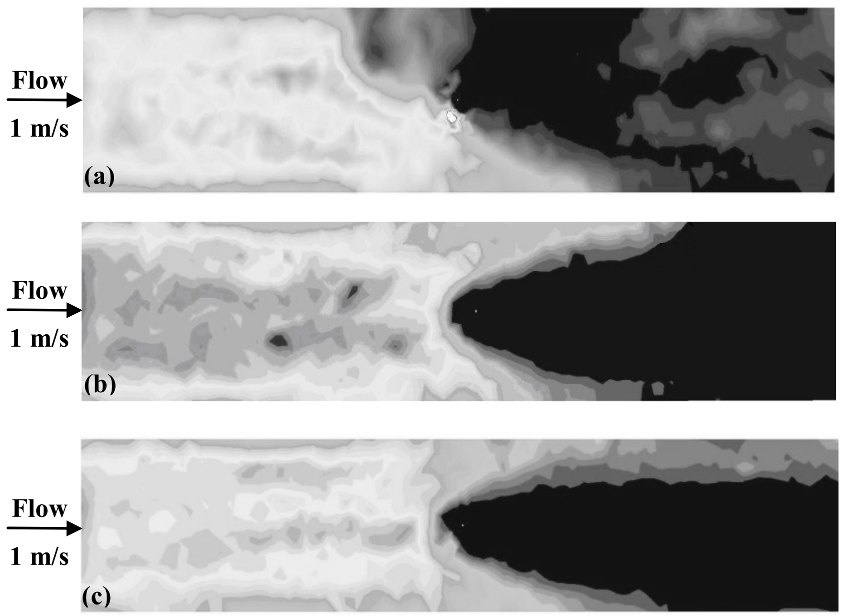

Figure 4.23. Particle concentrations in $z = 0$ symmetry plane for three different stages of the iteration process.

4.3.5.5 Comparing precipitation performance for different concentrations

The results of total mass transfer efficiency and collection efficiency for the individual particle sizes of: 0.3, 1.4, 5, 10 and 15 μm, and for different particle mass flow rates are shown in Table 4.4. For the smallest particle size (0.3 μm) the collection efficiency is very low; increasing the particle size to 10 μm, the collection efficiency also increases and for particles of 15 μm and larger, all of the particles are theoretically trapped on the deposited planes. The effect of different particle concentration on collection efficiency of small particle sizes is also shown in Table 4.4. Increasing the particle mass flow rate from $c = 0.5c_0$ to $c = 20c_0$, the collection efficiency for small particles of: 0.3, 1.4 and 5 μm rise by 47.1%, 26.5%

and 8.8%, respectively. With regard to the particle concentration patterns for different mass flow rates at inlet (Figure 4.14a, Figure 4.16a, Figure 4.20a and Figure 4.23), it is clear that, due to turbulence, the air drag forces, which push the particles towards the deposition planes, are getting stronger with increasing particle concentration. This is why the particle free region downstream of the channel significantly spreads out towards the collecting plates. Since the drift velocity of very small particles is negligible, they are easily entrained by the airflow and directed towards the deposition planes, which increases their chances of being trapped there. The slight decrease in collection efficiency of 10 μm particles for higher particle concentrations, shown in Table 4.4, is due to corona discharge suppression. According to Figure 4.11, 54.7% of the total mass flow at the precipitator inlet is in the form of large particles (15-90 μm) and these particles are fully trapped. On the other hand, 10 μm particles contribute almost 38% of the total mass flow at the inlet, having high collection efficiency as well. Therefore, the small particles (0.3-5 μm) with low collection efficiency occupy only a small portion of the total mass at the inlet (approximately 7.3%), having negligible effect on the total mass transfer efficiency. The above reasons justify the high and almost the same value of total mass collection efficiency obtained for different particle mass flow rates.

Table 4.4. ESP performance for different particle mass flow rates.

Total mass flow rate (kg/s)	**Collection efficiency**					**Total mass transfer efficiency**
	0.3 μm	**1.4 μm**	**5 μm**	**10 μm**	**15 μm**	
$c=0.5c_0$	8.5%	20.7%	59.5%	98.5%	100%	96.7%
$c=2c_0$	10.0%	19.5%	58.5%	98.5%	100%	96.6%
$c=10c_0$	10.7%	22.5%	60.0%	97.7%	100%	96.5%
$c=20c_0$	12.5%	26.2%	64.7%	96.7%	100%	96.4%

4.3.5.6 Particle distribution at inlet and outlet for different concentrations

The two curves in Figure 4.24a show the mass flow rate distribution of different particles fractions at the inlet and outlet, as the percentage of total mass flow rate in ESP entrance, assuming $c = 10c_0$. The areas under these curves are equal to the total mass flow rates of inlet and outlet particles. The inlet curve is based on a lognormal function distribution as shown in Figure 4.10. From these curves, one can estimate the mass collection efficiency of the precipitator. Integrating the area under the outlet curve in Figure 4.24a, the ratio of escaped particle mass and the total mass injected to the inlet could be obtained, which is 3.5% for this case and hence yielding 96.5% particle removal efficiency. Similar curves can be obtained for different inlet particle concentrations. Figure 4.24b shows the escaped mass flow rate of different particle sizes as percentage of the total mass flow rate at the outlet for different inlet particle concentrations. For all particle concentrations the maximum portion of mass at the outlet is due to 5 μm particles and no particles greater than 15 μm can be observed in this region. For high particle mass flow rates ($c = 10c_0$ and $c = 20c_0$) the mass percentage of 10 μm particles at the outlet is increased, where the corona discharge is suppressed by the existence of charged particles in the channel, leading to decrease in the charge carried by larger particles; thus, the slight decrease in collection efficiency of larger particles is mainly due to the weak contribution of electrostatic drag forces.

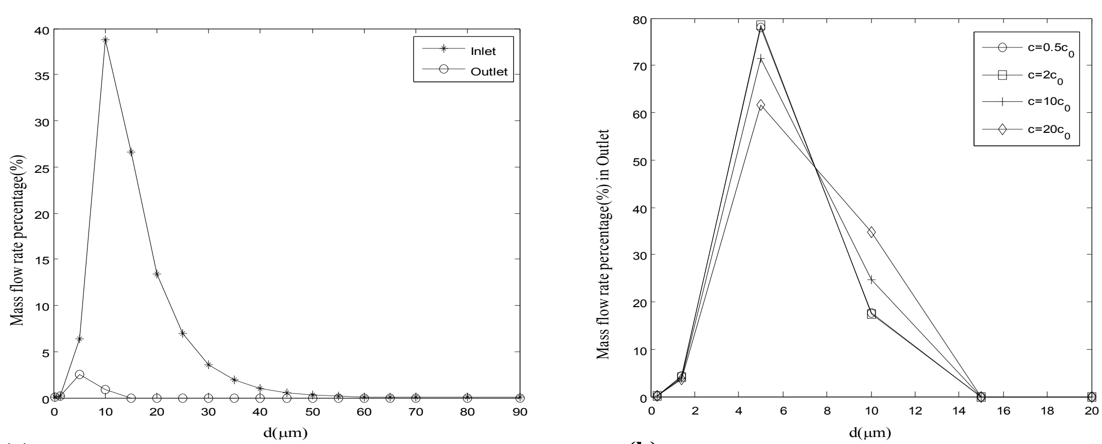

(a) **(b)**

Figure 4.24. Distribution of mass flow rate versus particle diameter (a) at inlet and outlet for the inlet particle mass flow rate of c=10c_0 (b) at outlet for different inlet particle mass flow rates (inlet velocity 1 m/s, corona wire voltage +30 kV).

4.3.6 Particle concentration effect on corona discharge current

The effect of the particle mass flow rate on the total corona current is shown in Figure 4.25. The increase of particle concentration causes a decrease in the average discharge current from I_0 = 108 μA for very low particle concentration to I_0 = 63 μA for very high particle concentration. Increasing the particle concentration increases the total charge density in the Poisson equation leading to the decrease of electric field intensity on the corona wire surface [21]. Therefore, the total discharge current, which depends on ionic charge density and electric field intensity on the corona surface, decreases.

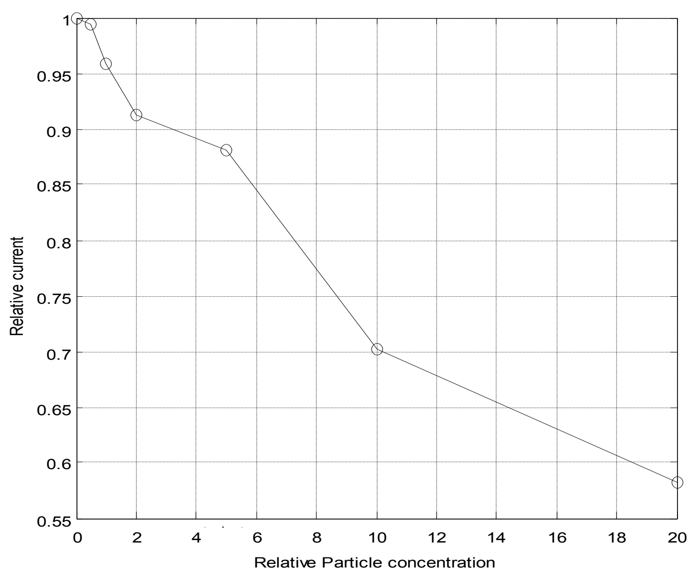

Figure 4.25. Relative corona current versus relative particle concentration.

4.4 Summary

A 3-D computational model was developed to study all essential phenomena in a simple one stage single wire-plate ESP, taking into account the mutual interactions between electrostatic field, flow field, particle charging and their turbulent motion. It includes a determination of the electrical conditions (electric field and space charge), the flow pattern induced by the interaction of the ionic wind with the main gas flow, and the particle trajectories and deposition under different particle concentrations at inlet. The model was created in commercially available FLUENT 6.2 software through the addition of UDFs. Particle charging and the electrostatic forces on them were computed in the corresponding UDFs. Particle motion was determined using the FLUENT DPM as discussed in Chapter 3.

The 3-D numerical simulations for a range of mono-disperse particle diameters (1 μm-50 μm), a dilute particle concentration and negligible particle space charge was demonstrated and discussed. The influence of the EHD flow on particle collection was also investigated. The presented results confirmed that higher particle collection efficiencies are obtained for the larger particles. It was shown that the EHD flow has a negligible effect on the collection efficiency of very small particles and no practical effect on large particles. The influence of increasing particle concentration on the airflow and particle flow pattern was investigated as well. A poly-dispersed lognormal particle size distribution was assumed at the inlet and particle transport of different sizes, particle concentration patterns and the average charge to mass ratio for each particle sizes on the collecting planes were simulated. The results confirm that regardless of the particle size, a high percentage of the deposited particles are trapped in the areas close to the corona wire on the collecting planes and the larger particles always have the highest collection efficiency due to stronger electrostatic forces acting on them. It was shown that the increase of particle concentration significantly changes the airflow structure behind the wire and makes it more turbulent, leading to slightly higher collection efficiency for very small particles. The particle flow patterns obtained for different inlet mass flow rate verified that the particle free region in the downstream direction behind the corona wire spreads out as the concentration increases. A similar value of mass collection efficiency was obtained for different mass flow rates due to the dominant portion of large particles injected at the inlet. No particle size of 15 μm and greater was observed at the outlet and 5μm particles had the highest mass percentage at the outlet for various particle concentrations. About 42% decrease in the total average discharge current was observed by increasing the mass flow rate from $c = 0.5c_0$ to $c = 20c_0$ which agrees fairly well with measurements presented in [20].

The content of this chapter has been published in two journal papers [113], [114].

5. MODELING OF A SINGLE-STAGE SPIKE-PLATE ESP

5.1 Introduction

The numerical algorithm proposed in Chapter 3 has been utilized to evaluate the electrical and EHD flow characteristics of a laboratory scale single-stage spike-plate ESP, experimentally investigated in [25,26], and to predict the collection of submicron particles with diameters in the range of 0.25-1.5 μm. The precipitator consists of two parallel collecting plates with a spiked electrode mounted at the center, parallel to the planes and excited with a high negative dc voltage. A non-uniform corona discharge is produced along the electrode in the form of a flat tape with some number of spikes, assuming that ions are generated only near the spike tips, where the electric field magnitude is the strongest. The complex interaction between the electric field, fluid dynamics and the particulate flow in this precipitator was taken into account in the simulation. The fully 3-D turbulent airflow distribution was calculated using the commercial FLUENT software assuming a standard k-ε turbulence model. Particles were assumed to be charged by combined field and diffusion charging mechanisms. Motion of submicron particles under electrostatic and aerodynamic forces in turbulent airflow was calculated using a Lagrangian-type DRW model and UDFs feature of the commercial FLUENT 6.2 software.

The EHD secondary flow patterns, particle migration velocity patterns and particle collection efficiencies were examined for three different corona discharge electrode configurations: a two-sided spiked electrode and a one-sided spiked electrode with the spikes located either in the upstream or downstream direction of the airflow. The EHD secondary flow and its interaction with the main airflow in different planes along the precipitation channel were examined for different voltages applied to the corona wire. For a given dust mass flow rate at inlet, the EHD flow effect on particle deposition rate and the average charge-to-mass ratios along the channel were evaluated for different particle sizes and applied voltages. Finally, the influence of dust mass flow rate on collection efficiency for the ESP with spikes on two sides was investigated for -30 kV applied voltage. In selected cases, the numerical results were compared with experimental data published in the literature [25,26].

5.2 Model description

The ESP model consists of two grounded parallel plates, which are electrically conducting and grounded, and a spiked electrode located midway between the plates and supplied with a high negative potential as shown in Figure 5.1. The ESP channel is 600 mm long, 200 mm wide and 100 mm high. The discharge electrode consists of a flat metal strip having a series of spikes alternatively oriented upstream and downstream and parallel to the airflow. The electrode was 200 mm long, 1 mm thick and 30 mm tip to tip wide (Figure 5.2 [25]). Three spiked electrode configurations were considered: spikes located alternatively on both sides of the electrode and spikes located on one side of the electrode, either in the upstream or downstream direction (Figure 5.3 [26]).

A negative high voltage supply was connected to the spiked electrode, which created gas ionization (corona discharge) at the spike tips, injecting ionic space charge into the channel. The airflow was assumed to be incompressible, steady and turbulent. A flat velocity profile of 0.6 m/s at the channel inlet, zero gauge pressure at the outlet and zero velocity components at all electrodes and walls were considered as the fluid boundary conditions. The air viscosity μ = 1.57e-5 [kg/m.s], air density ρ_f = 1.205 [kg/m^3] and ion mobility K = 2.4e-4 [m^2/V.s] were chosen in calculations.

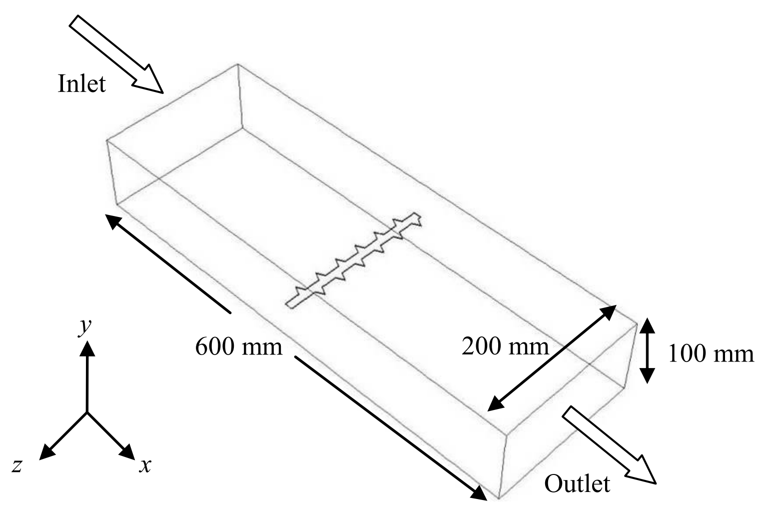

Figure 5.1. 3-D configuration of a single spike wire-plate model of ESP.

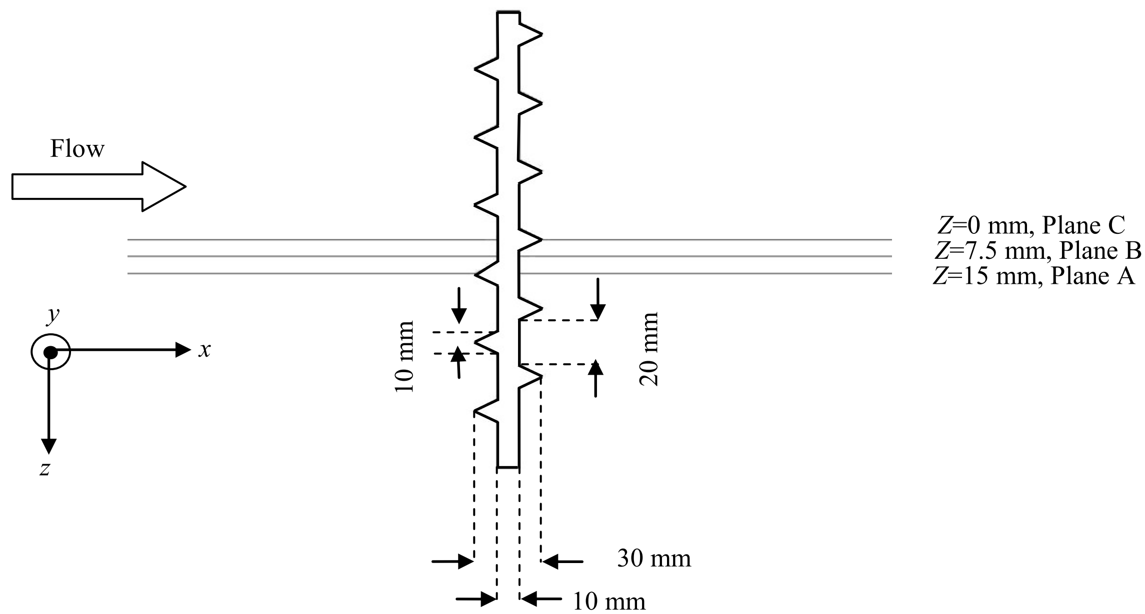

Figure 5.2. Schematic drawing of the discharge electrode with spikes on two sides (top view).

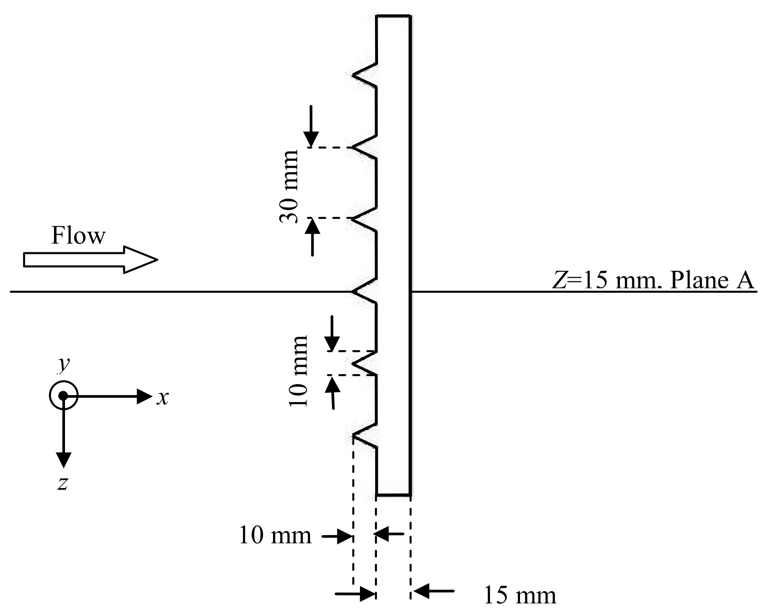

Figure 5.3. Schematic drawing of the discharge electrode with spikes in the upstream direction (top view).

5.3 Numerical Algorithm

The whole computational domain was discretized into a number of tetrahedral elements with a very non-uniform density, using the commercial software GAMBIT (Table 5.1); the elements in the vicinity of the spikes' tips were much smaller than in other places, especially very close to the collecting plates. The hybrid FEM-FCT technique was implemented for solving the Poisson and current continuity equations to estimate the electric potential and ion charge density distributions in the precipitation channel for different applied voltages. The full description of this method can be found in Chapter 3. Due to a non-uniform distribution of the ion charge density along the corona electrode surface, the Kaptzov assumption was not practical in this simulation. Instead, the total corona discharge current obtained from numerical simulations was compared with the experimental value obtained by Mizeraczyk *et al.* [25,26]. In the iterative process the electric ion charge density on the corona wire surface was modified until the discharge current obtained from simulation was in a close agreement with the experimental data. According to our investigations, the ionic charge density distribution pattern is only very slightly perturbed by the airflow; therefore, the convection of ions was ignored and only the strong effect of electrostatic forces due to the presence of ionic space charge in electric fields on the airflow patterns was considered in this simulation.

Table 5.1. Number of nodes and elements in discretization for three spiked electrode geometries.

GAMBIT discretization	Two sided spiked electrode	One sided spiked electrode (in upstream direction)	One sided spiked electrode (in downstream direction)
# Tetrahedral elements	178316	197457	195135
# Nodes	35889	40115	39723

5.4 Simulation results and discussions

5.4.1 Electrical characteristics

Figure 5.4 shows the electric potential distribution in $z = 0$ plane of the precipitation channel, assuming that the corona electrode is excited with a negative voltage of 30 kV. 50 contours are shown, which means that the potential difference between two adjacent lines is 600 V. The contour density decreases from the area in vicinity of the corona electrode to the grounded plates. Determining the 3-D distribution of ionic space charge density in the ESP channel for the spike-type discharge electrode is crucial, because ions are only injected from areas close to the spikes tips and a noticeable volume fraction of the ESP is charge free. The ion charge density at the injection tips has been evaluated to have the total average discharge current obtained from calculations equal to experimental data presented in [25]. Figure 5.5a shows the ion charge density distribution contours in $y = 0$ symmetry plane. When a negative voltage of 30 kV is applied, the maximum ion charge density of -485 $\mu C/m^3$ is obtained close to the spike tips. The ions injected from each spike migrate to the collecting plates creating ionic space charge density, which decreases in the field direction as shown in the $z = 0$ plane in Figure 5.5b. The corresponding ionic current densities on the ground plates are shown in Figure 5.6 as well. According to the time averaged current-voltage characteristics curves the total discharge current at this voltage is 350 μA [25].

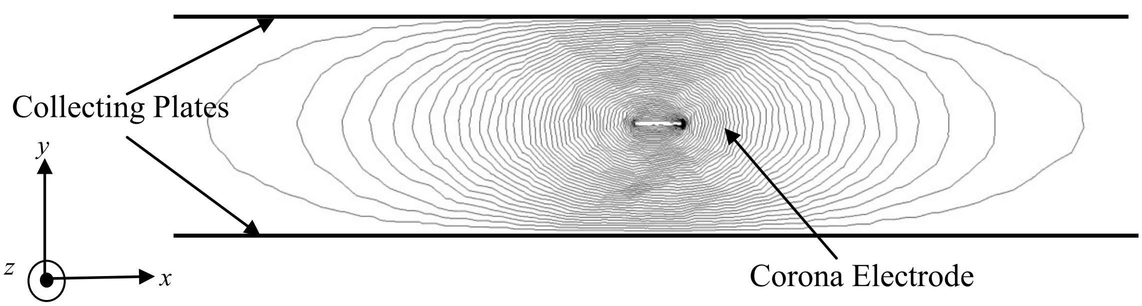

Figure 5.4. Electric potential contours in $z = 0$ plane of ESP (number of contours 50, applied voltage -30 kV).

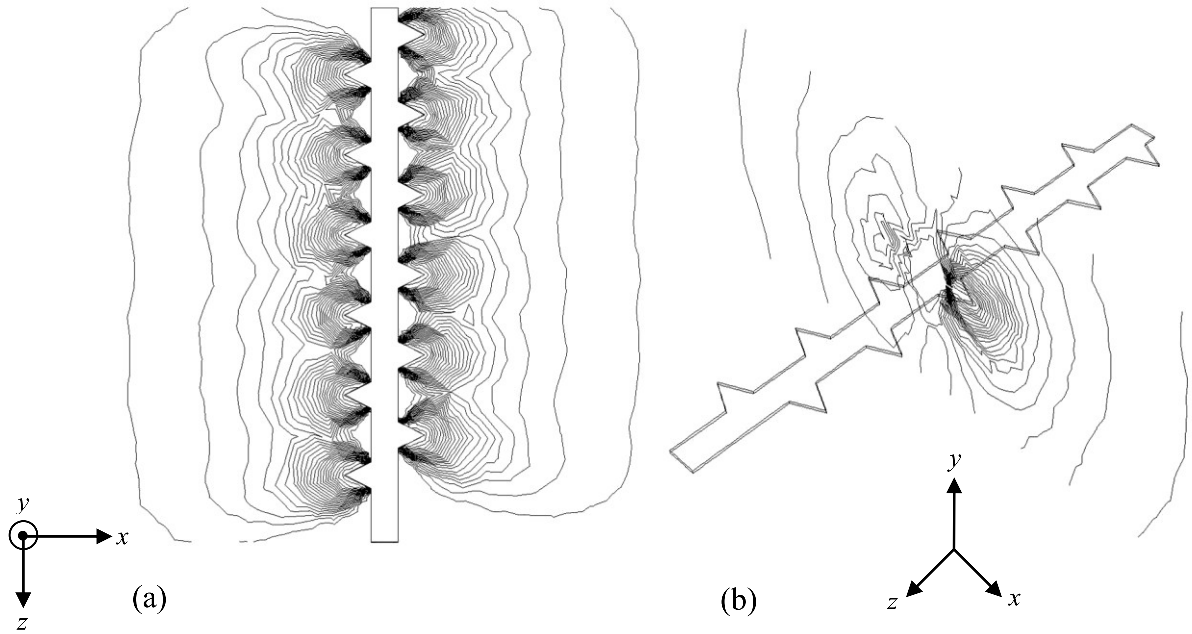

Figure 5.5. Ion charge density distribution contours in (a) $y = 0$ and (b) $z = 0$ planes (number of contours is 25, the maximum ion charge density on each spike is -485 $\mu C/m^3$and the applied voltage is -30 kV).

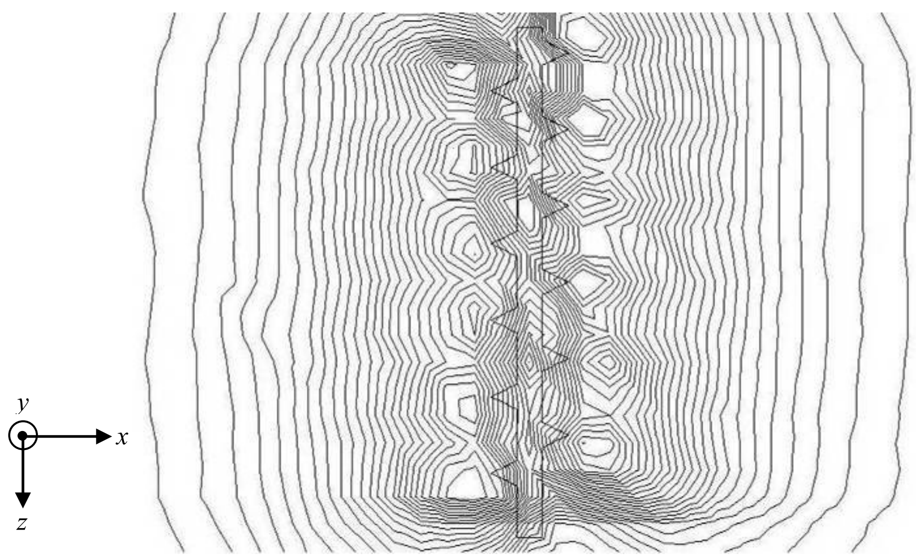

Figure 5.6. Ion charge density distribution on the collecting plates (number of contours 25 and maximum ion charge density -68.5 $\mu C/m^3$).

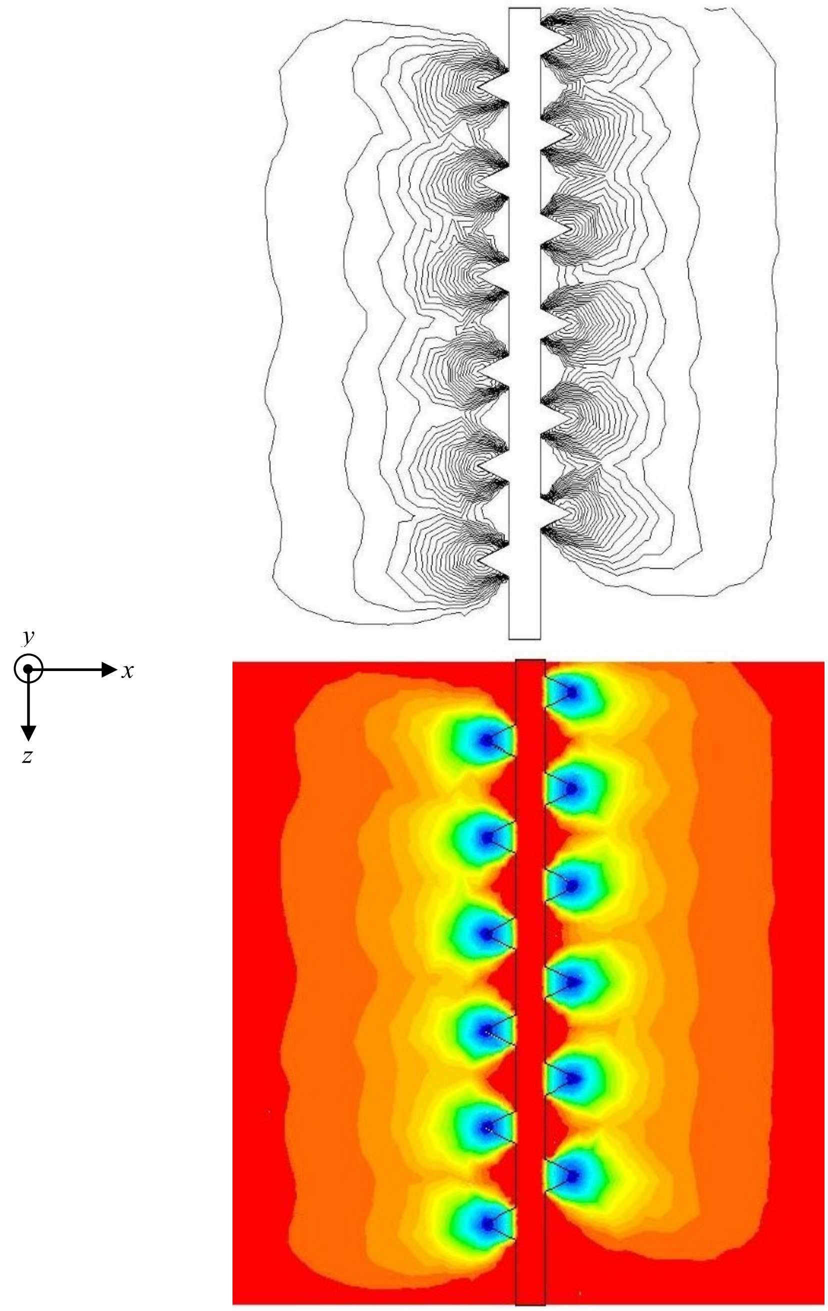

Figure 5.7. Ion charge density distribution contours in the $y = 0$ plane for non-uniform discharge from spike surfaces (number of contours is 20, the maximum ion charge density on each spike tip is -565 $\mu C/m^3$ and the applied voltage is -30 kV).

For the ESP configuration with spikes pointed in the upstream direction, Figure 5.8 shows ionic charge density distribution for -30 kV applied voltage. Non-uniform ion charge injection from the spike surfaces are assumed where the maximum ion charge density on the spike tips, calculated from the experimental *V-I* characteristics [26], is -532 μC/m^3.

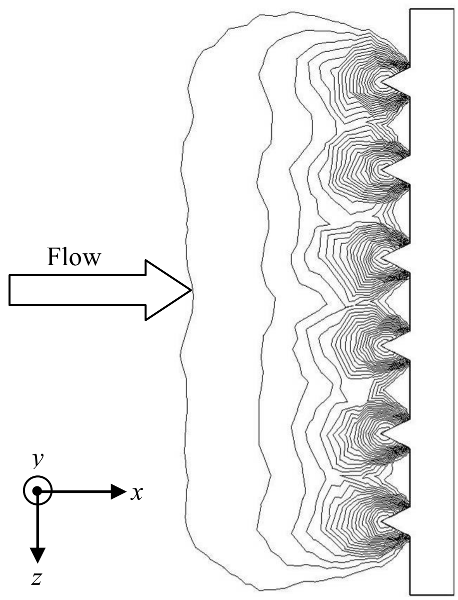

Figure 5.8. Contours of ion charge density distribution in the $y = 0$ plane for ESP with spikes in the upstream direction (number of contours is 20, the maximum ion charge density on each spike tip is -532 μC/m^3, applied voltage is -30 kV and inlet velocity is 0.6 m/s).

5.4.2 3-D EHD flow patterns

5.4.2.1 Two-sided spiked electrode

In this study a uniform ion space charge density on the spike surfaces was assumed, as depicted in Figure 5.5a and Figure 5.5b. All numerical simulations were repeated considering non-uniform ion charge density distribution on the spikes in which the maximum charge was injected from a small area close to the tip of each spike (Figure 5.7) to model a more realistic situation. Due to this change in the boundary conditions a small difference in the ion space charge density close to the corona electrode can be noticed. However, no significant changes were observed in the distribution of the ion space charge density farther from the discharge electrode. As a result, all calculated airflow velocity patterns are practically identical for both cases.

The effect of the secondary EHD flow on the main airflow pattern for different applied voltages was examined by comparing the airflow streamlines in three different planes (A, B and C) located along the channel length and perpendicular to the spiked electrode as shown in Figure 5.2. Figure 5.9a - Figure 5.9c show the 3-D airflow streamlines in plane A, which passes through the tip of the upstream-directed central spike electrode for three negative applied voltages of -30 kV, -23.5 kV and -19.2 kV, respectively. These figures demonstrate a very complicated airflow structure around the spikes tips.

As shown in Figure 5.9a for the highest excitation voltage (-30 kV), due to the strong interaction between the secondary EHD flow and the main airflow, a pair of vortices is generated in plane A, located in the vicinity of the upstream directed spike tip. The two vortices interfere with the main airflow in the upstream part of the channel and drive the airflow towards the collecting plates. However, these two vortices get smaller and move closer towards the spike electrode, when the excitation voltage is decreased to -19.2 kV (Figure 5.9c). The experimental results in [25] demonstrate another pair of vortices as well, which is formed in the downstream of the channel very close to the collecting planes preventing the main airflow from moving towards the plates. However, this is not clearly visible in the simulation results. The observed differences in the results could be due to the resolution of the numerical method: the domain discretization close to the collecting plates is not sufficiently fine to capture the vortices generated in these areas. On the other hand, the experimental flow velocity patterns in planes A, B and C in [25] are composed of three adjacent overlapping velocity fields and are obtained from averaging of 100 measurements using a 3-D PIV method, in which fine TiO_2 particles of less than 1 μm in size were blown through the channel. Thus, in practice the velocity streamlines presented in their paper demonstrate the average trajectories of submicron particles, which mostly follow the airflow streamlines. The numerical results in Figure 5.9a - Figure 5.9c also show a slight deflection of airflow streamlines towards the center of the channel in the downstream direction after the airflow passes the spiked electrode.

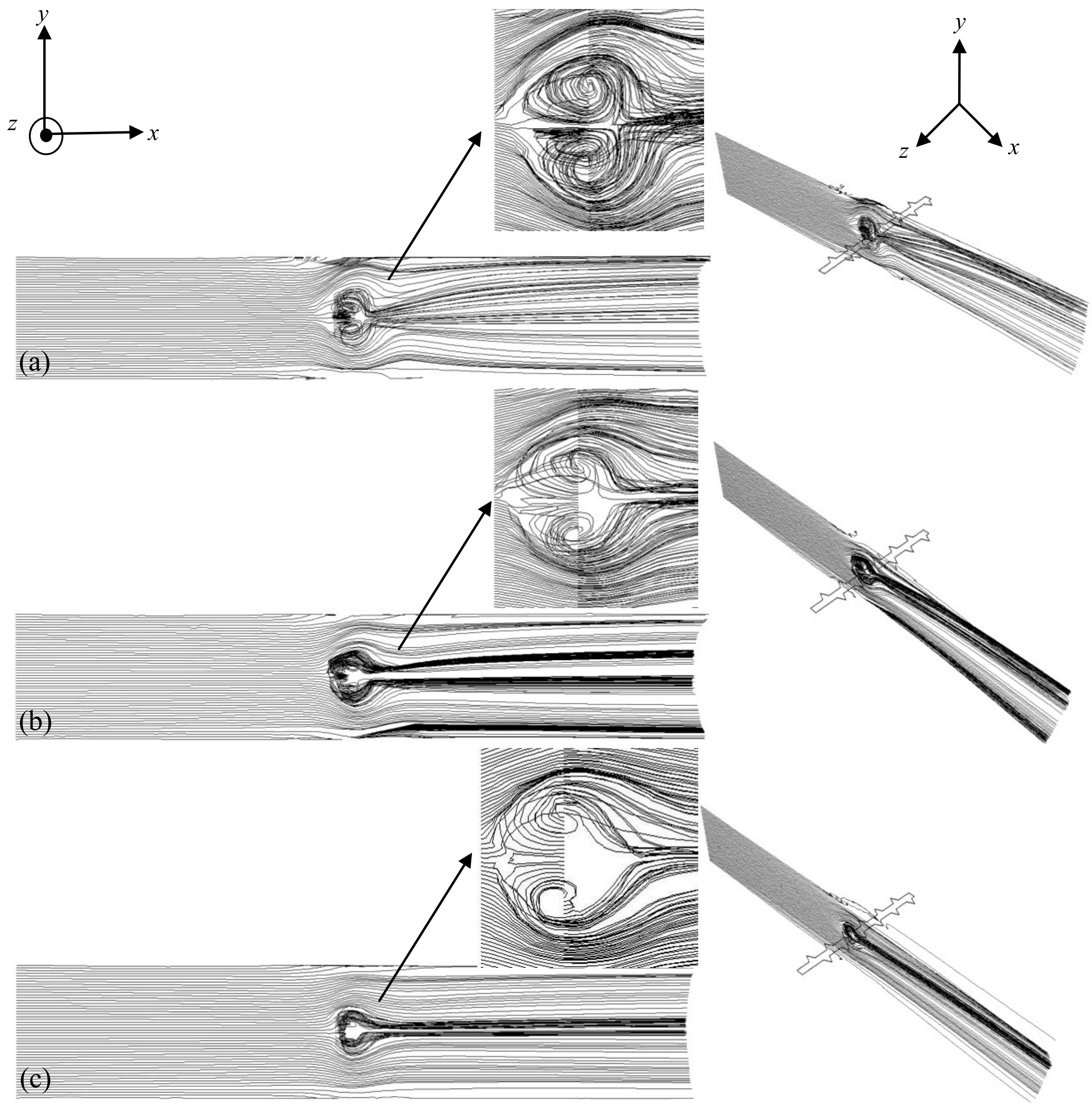

Figure 5.9. Airflow streamlines in plane A for negative applied voltage of (a) -30 kV and discharge current 350 μA (b) -23.5 kV and discharge current 170 μA (c) -19.2 kV and discharge current 90 μA.

Figure 5.10a - Figure 5.10c show the airflow streamlines in plane B, which passes between upstream and downstream spikes. For the same voltages, the centers of the two vortices slightly move in the upstream direction and are smaller in size than the vortices generated in plane A. The pattern of airflow streamlines in plane C, which passes through the tip of the neighbouring downstream-directed spike, Figure 5.11a - Figure 5.11c, shows no generated vortices. Since the secondary EHD flow from the spike tip in the plane C and the primary airflow are in the same direction, their interaction is weaker and the vortices generated in this plane are not significant. Looking from a different angle to the airflow streamlines for -30 kV applied voltage (Figure 5.12) shows that some of the streamlines deflect towards the neighbouring spike tip located behind the plane C, which is in opposite direction with respect to the main airflow, and then turn back towards the downstream direction of the channel. Therefore, due to the strong interaction of the upstream-directed secondary EHD flow generated from the upstream spike tip in the plane A with the oppositely directed primary airflow, stronger vortices are generated in plane A rather than in plane C. Higher excitation voltages always induce stronger vortices.

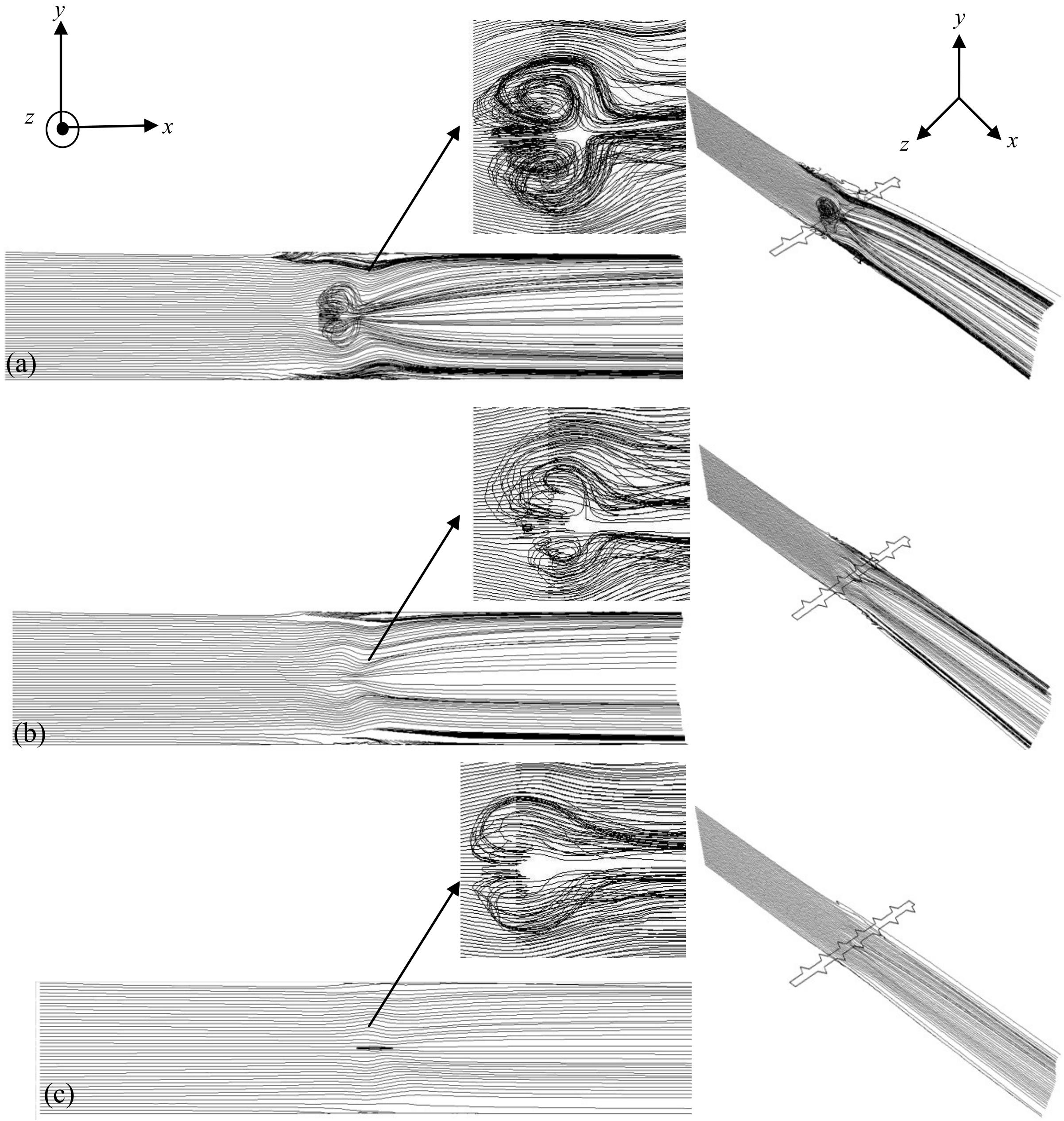

Figure 5.10. Airflow streamlines in plane B for negative applied voltage of (a) -30 kV and discharge current 350 μA (b) -23.5 kV and discharge current 170 μA (c) -19.2 kV and discharge current 90 μA.

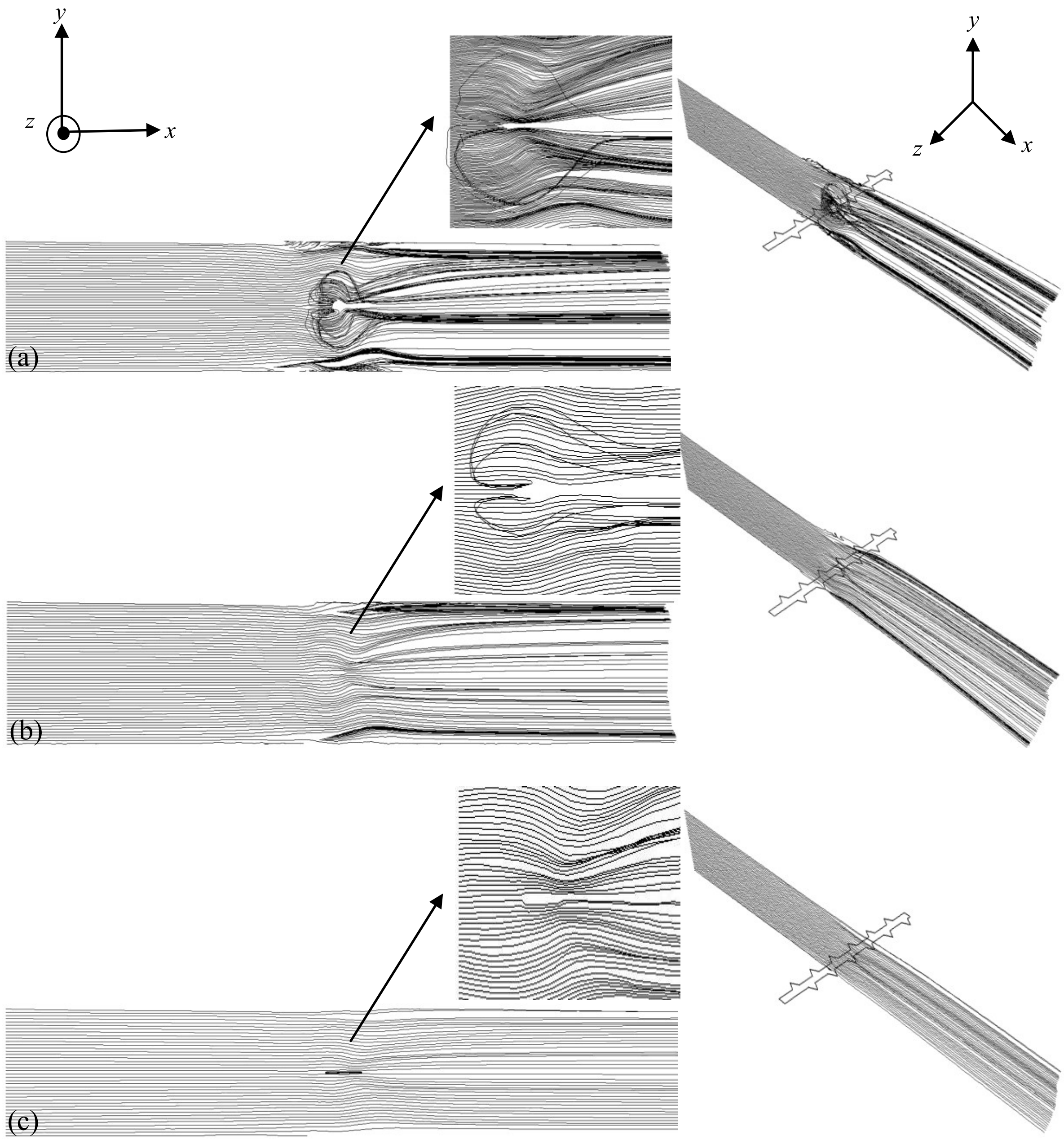

Figure 5.11. Airflow streamlines in plane C and negative applied voltage of (a) -30 kV and discharge current 350 μA (b) -23.5 kV and discharge current 170 μA (c) -19.2 kV and discharge current 90 μA.

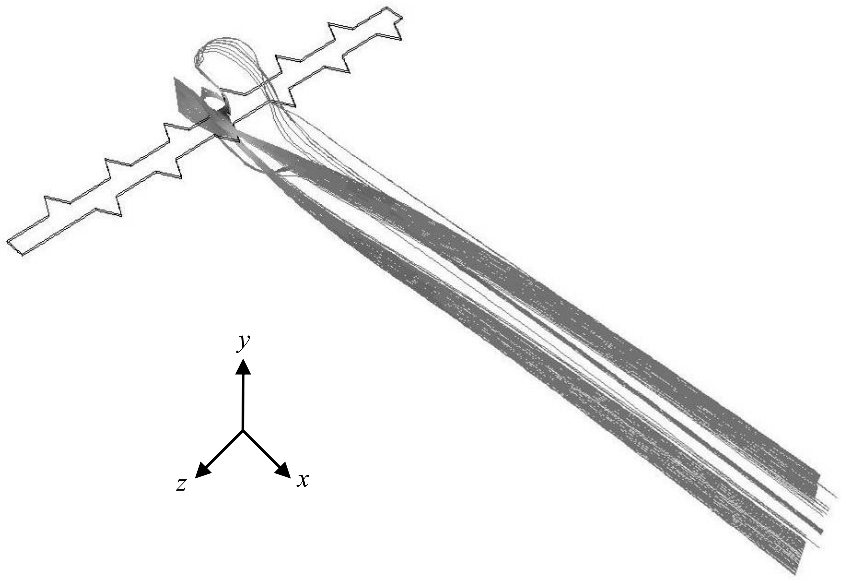

Figure 5.12. Interaction of airflow streamlines in planes C and A for applied voltage of -30 kV.

Figure 5.14 - Figure 5.16 show the *x* component of the airflow velocity vector in planes D-H for different applied voltages. The planes are perpendicular to the ESP channel and spaced uniformly from 60 mm upstream the spike electrode (x = -60 mm) to 60 mm downstream the spike electrode (x = 60 mm), as shown in Figure 5.13. Perturbed airflow velocity patterns are generated in the channel due to the complex interaction between main airflow and EHD flow. The airflow velocity pattern in plane D is not much disturbed for the lowest applied voltage (-19.2 kV), whereas quite a regular airflow pattern originating from the spike tips is visible in planes E-H. By increasing the excitation voltage, some airflow irregularities arise in central part of the channel in plane D, as shown in Figure 5.16.

These results are in a good agreement with the experimental results obtained by Mizeraczyk and his co-workers [25]. The side walls cause a dramatic airflow fluctuation around the spike tips nearest the walls. However, the airflow patterns around the central spikes tips are stable and very similar to each other as is also reported in [25]. The results confirm the complex 3-D airflow structures in spiked electrode configuration as well.

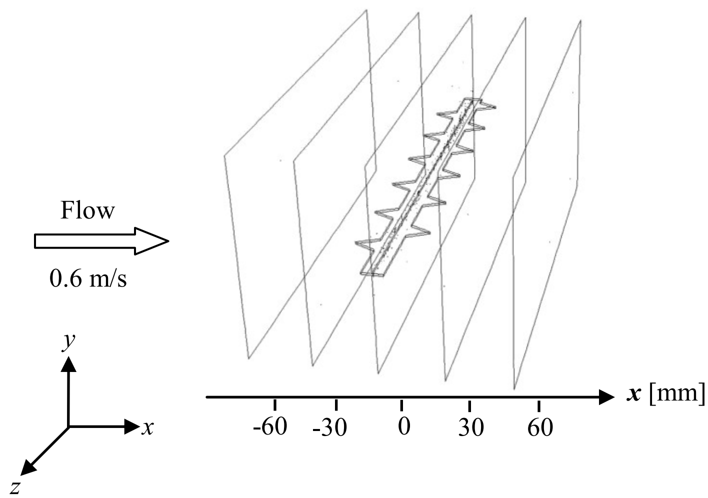

Figure 5.13. Equally spaced planes along the channel placed perpendicularly to airflow direction.

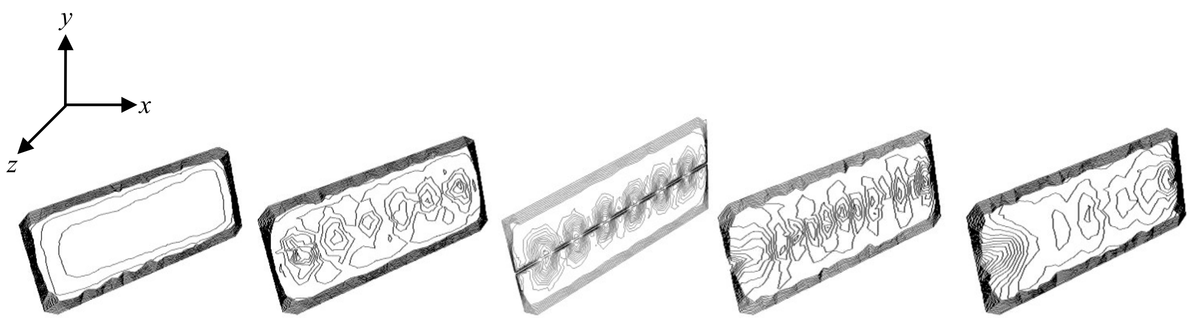

Figure 5.14. Distribution of the longitudinal component of airflow velocity in planes D-H for the applied voltage of -19.2 kV.

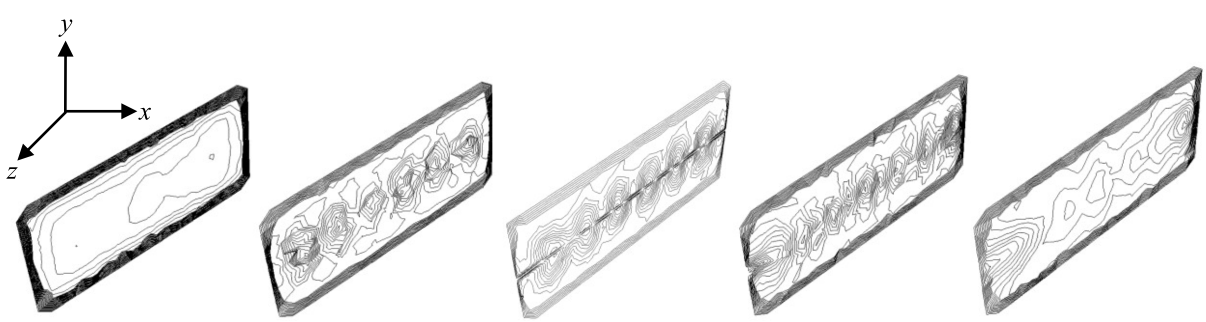

Figure 5.15. Distribution of the longitudinal component of airflow velocity in planes D-H for applied voltage of -23.5 kV.

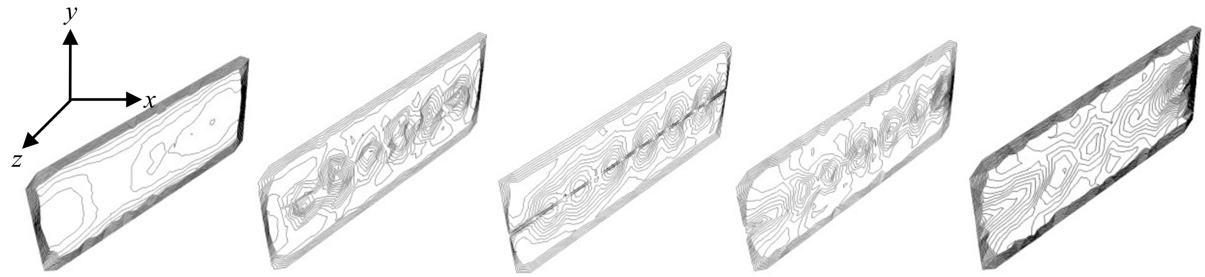

Figure 5.16. Distribution of the longitudinal component of airflow velocity in planes D-H for applied voltage of -30 kV.

Figure 5.17 and Figure 5.18 show turbulence intensity contours in the $y = 0$ plane for the lowest (-19.2 kV) and highest (-30 kV) applied voltages, respectively. The electric corona discharge is responsible for a strong increase of the turbulence level. Assuming 3% turbulence intensity at the inlet and increasing the applied voltage from -19.2 kV to -30 kV, the maximum turbulence intensity in the vicinity of the spiked electrode increases from 36% to 65%. The larger density of contours in the downstream direction of the channel in the case of -30 kV applied voltage also confirms larger turbulence intensity generated in this area for the larger excitation voltage.

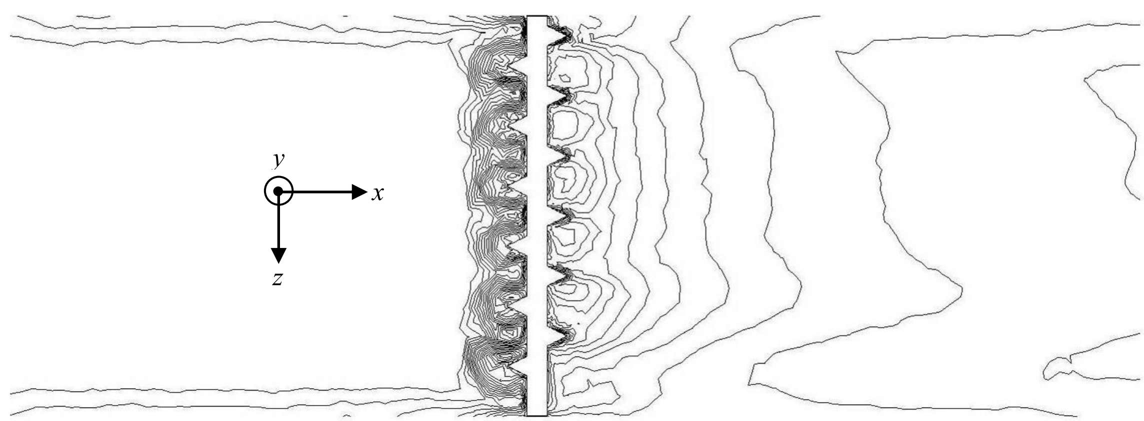

Figure 5.17. Turbulence intensity contours in $y = 0$ plane for applied voltage of -19.2 kV (number of contours is 20, the maximum and minimum turbulence intensities are 36% in vicinity of spiked electrode and 3% at the inlet)

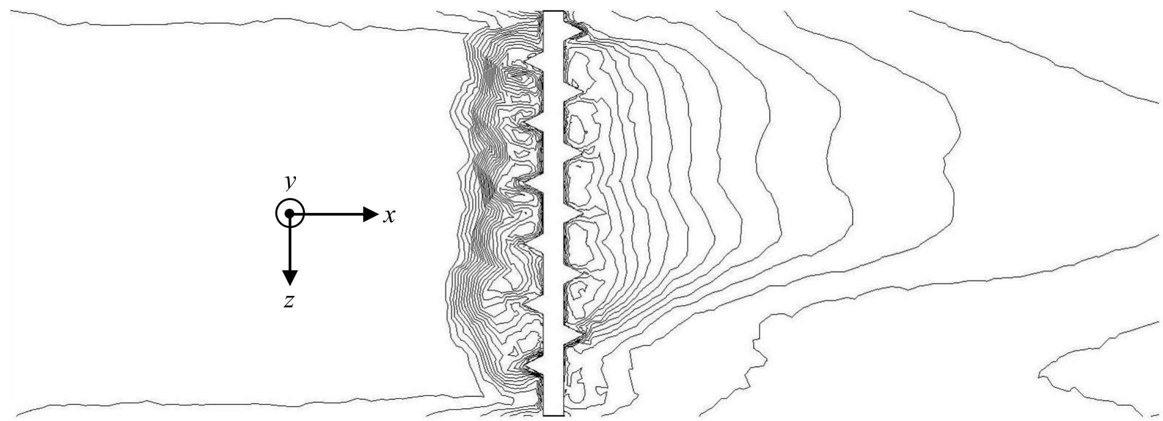

Figure 5.18. Turbulence intensity contours in $y = 0$ plane for applied voltage of -30 kV (number of contours is 20, the maximum and minimum turbulence intensities are 65% in vicinity of spiked electrode and 3% at the inlet)

The 3-D secondary EHD flow distributions in the channel in the case of -30 kV applied voltage without the main airflow are shown in Figure 5.20a and Figure 5.20b from both side and top view. The EHD flow streamlines in Figure 5.20a show two pairs of spiral vortices in the vicinity of the spiked electrode: one downstream and the other in the upstream direction of the channel. Figure 5.20b shows the EHD flow streamlines from the top view. The asymmetry in this figure is due to the non-symmetric position of the spikes on both sides of the strip electrode and the fact that the same value of ion space charge density was assumed on the spike surfaces along the discharge electrode (Figure 5.19a). The EHD flow has a swirling motion in the channel and consists of one very small circular vortex and a bigger spiral vortex in the -*x* direction and one long-elliptic spiral vortex in the *x* direction. After repeating the simulation for a non-uniform ion charge density distribution on the spikes surfaces along the electrode, *i.e.* the ion charge density on the spikes surfaces close to the walls is 75% of the ion charge density on spikes surfaces located in the middle (Figure 5.19b), the EHD flow streamlines in Figure 5.21a and Figure 5.21b demonstrate more symmetric patterns, as it was expected.

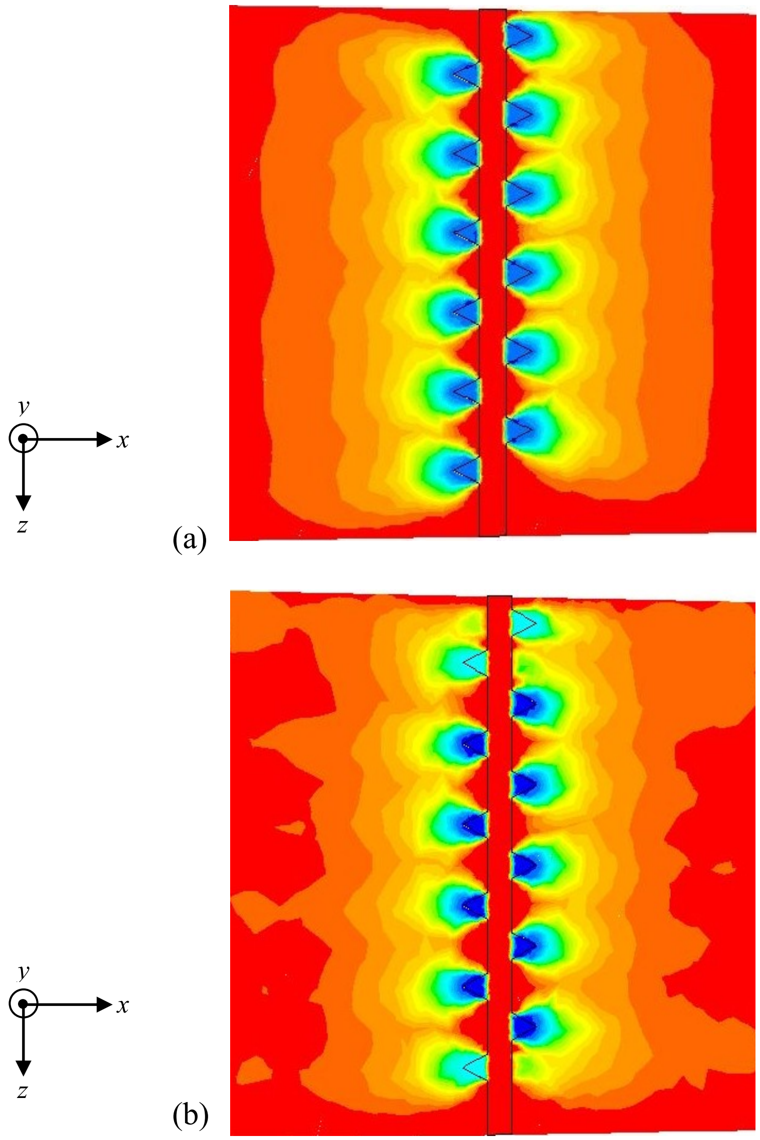

Figure 5.19. (a) Uniform and (b) non uniform charge density distributions on the spikes surfaces

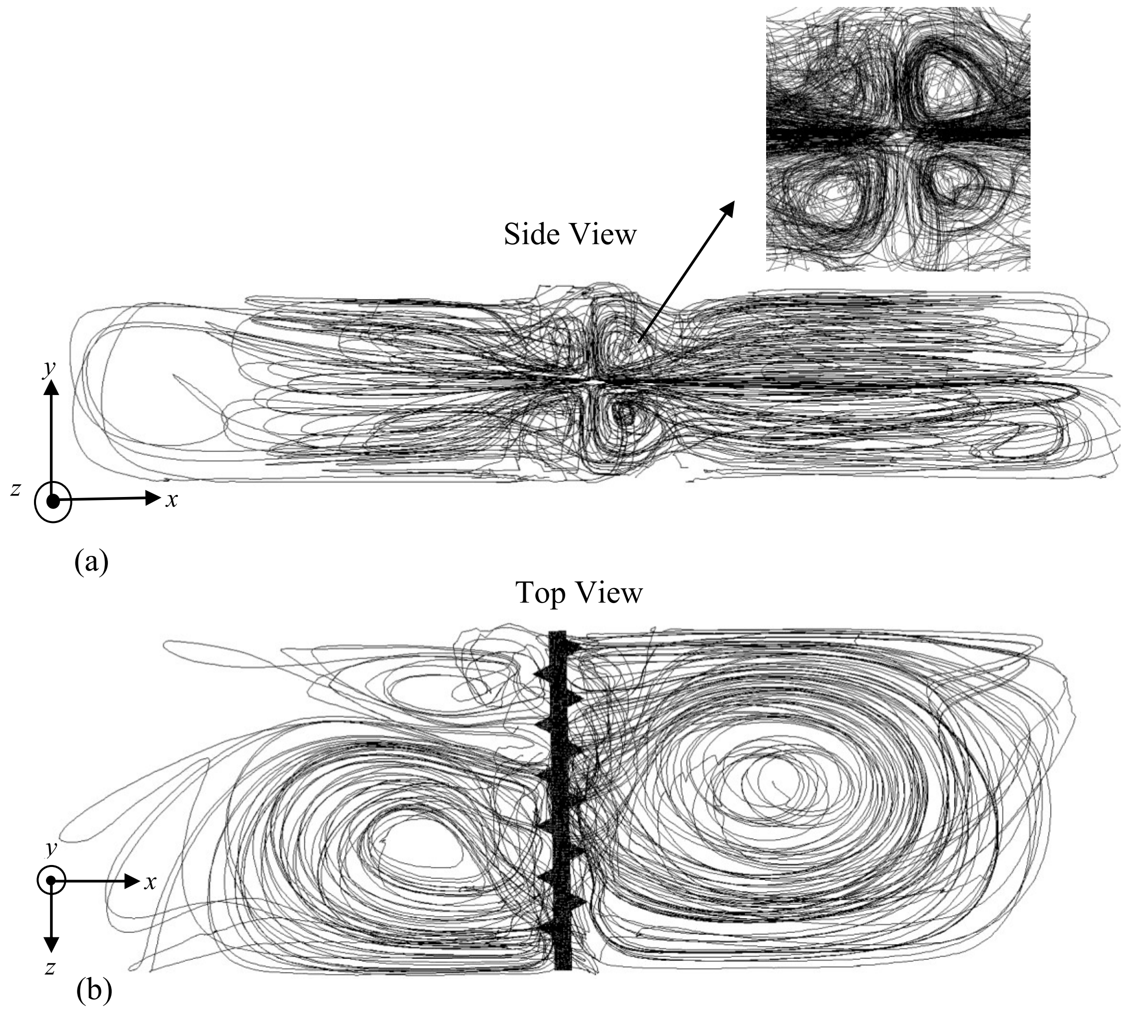

Figure 5.20. EHD Flow streamlines when inlet velocity is zero and applied voltage is -30 kV, assuming uniform ion charge density on spikes.

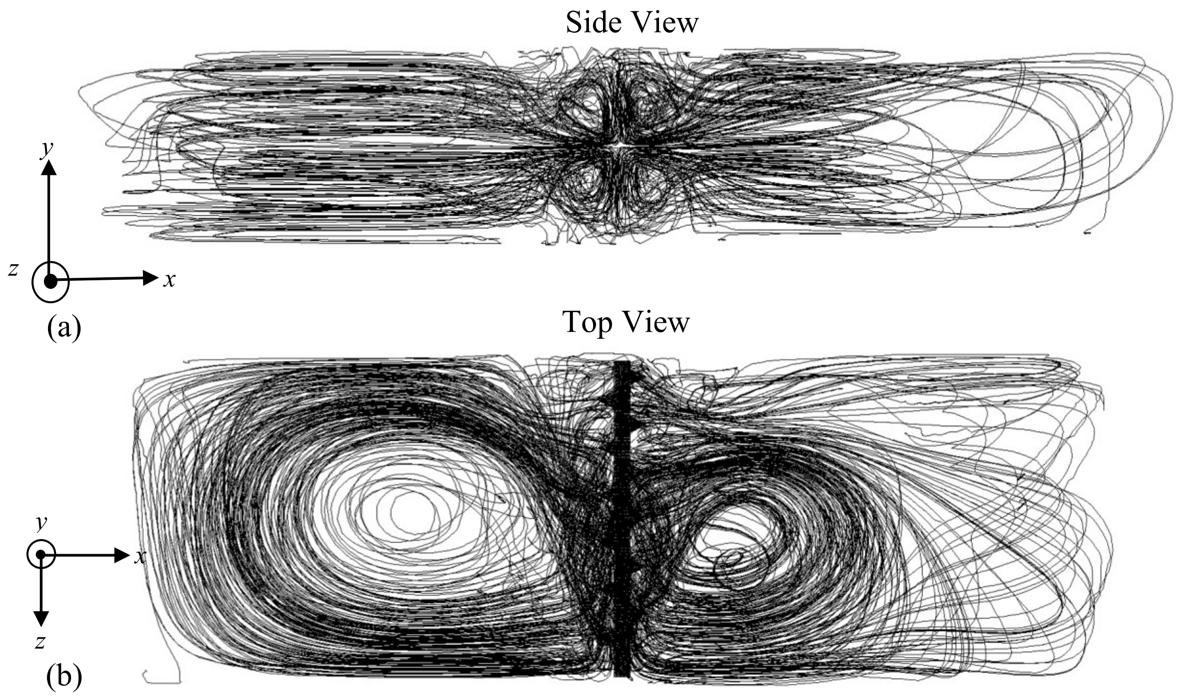

Figure 5.21. EHD Flow streamlines when inlet velocity is zero and applied voltage is -30 kV, assuming non-uniform ion charge density on spikes.

5.4.2.2 One-sided spiked electrode

Figure 5.22 and Figure 5.23 show the airflow streamlines in the plane A for the ESP with spikes in the upstream direction for -19.2 kV and -30 kV applied voltages, respectively. Two vortices are formed in the vicinity of the discharge electrode with the airflow circulating in opposite direction with respect to the main airflow. These vortices are much stronger for the higher applied voltage, partially blocking the main airflow in the channel, as shown in Figure 5.23, thus the airflow streamlines are more widely deflected towards the deposition planes. Therefore, due to the robust interaction of EHD secondary flow and the main airflow, and strong electrostatic forces near the corona electrode, the particles are moved from the central part of the channel towards the collecting plates.

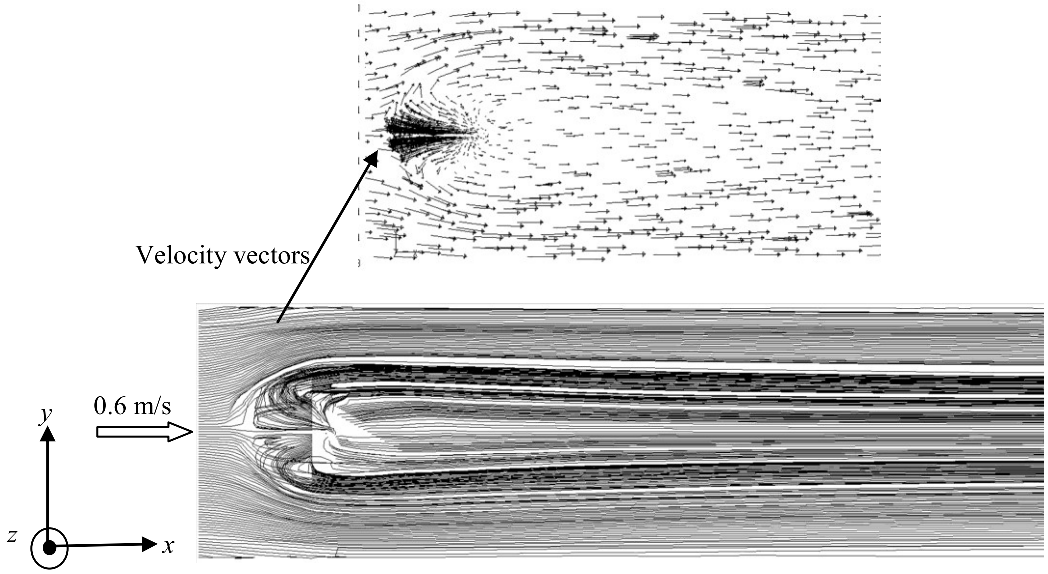

Figure 5.22. Airflow streamlines in plane A for ESP with spikes in upstream direction; applied voltage is -19.2 kV and inlet velocity is 0.6 m/s.

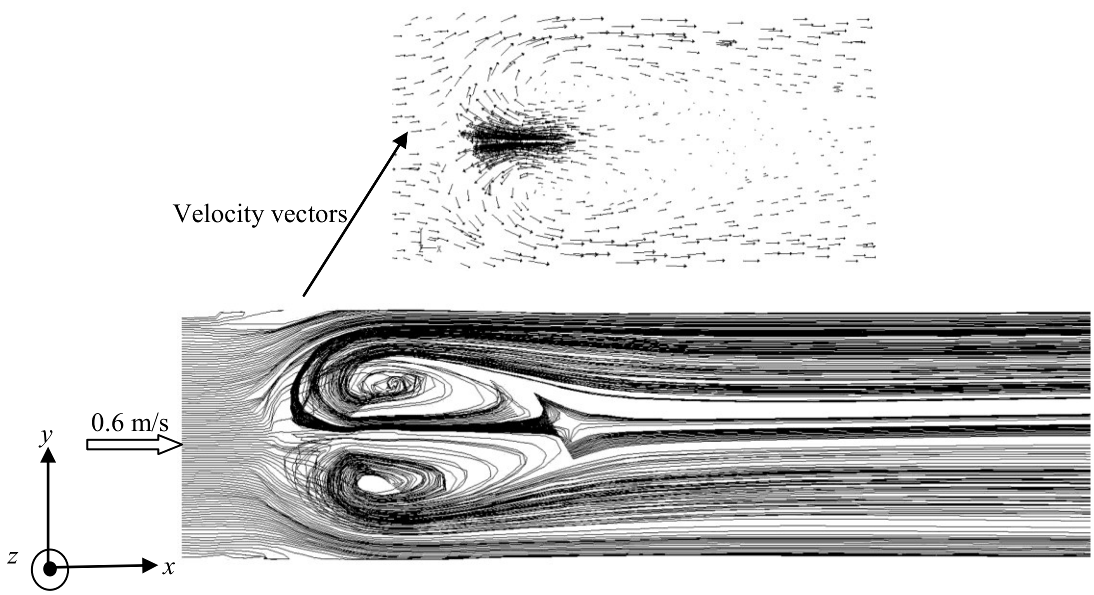

Figure 5.23. Airflow streamlines in plane A for ESP with spikes in upstream direction; applied voltage is -30 kV and inlet velocity is 0.6 m/s.

Figure 5.24 and Figure 5.25 show the airflow streamlines in plane A for -19.2 kV and -30 kV applied voltages, assuming that spikes along the discharge electrode are oriented in the downstream direction of the channel. Two vortices are formed in the vicinity of the deposition planes pushing the airflow towards the center of the ESP channel. Although these two vortices are very small and for -19.2 kV applied voltage (Figure 5.24) have negligible effect on collection efficiency, they get larger and stronger by increasing the applied voltage to -30 kV (Figure 5.25). In this case they have a more significant effect on fine particle removal.

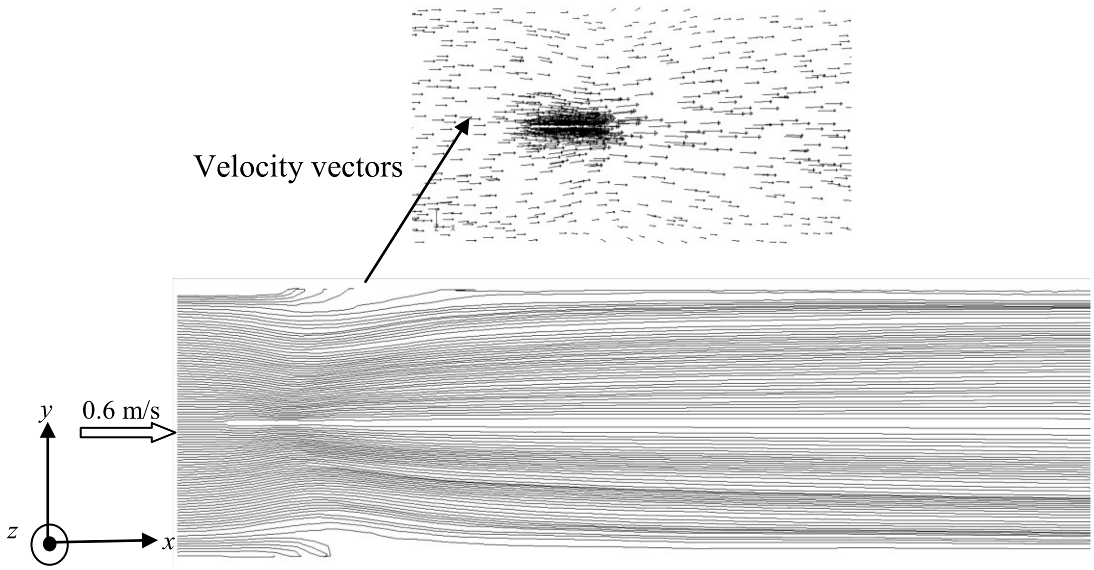

Figure 5.24. Airflow streamlines in the plane A for ESP with spikes in downstream direction (applied voltage is -19.2 kV and inlet velocity is 0.6 m/s).

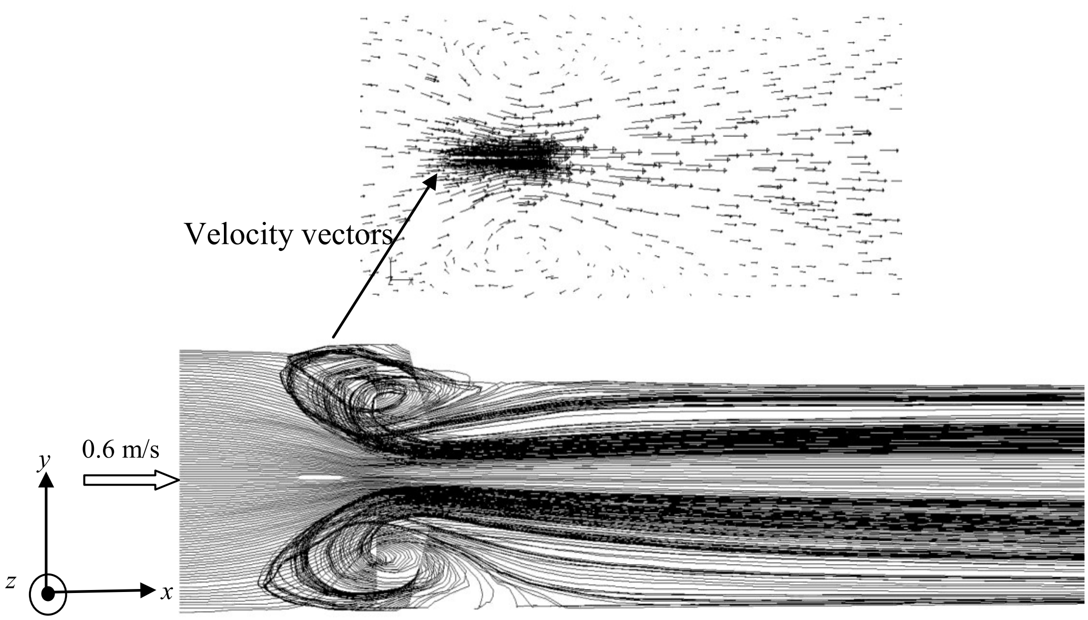

Figure 5.25. Airflow streamlines in the plane A for ESP with spikes in downstream direction (applied voltage is -30 kV and inlet velocity is 0.6 m/s).

5.4.3 EHD flow effect on ESP performance

The dust injected to the precipitation chamber is poly-dispersed with particles in the range of 0.25-1.5 μm, relative permittivity of 4.0 and different concentrations at inlet as shown in Figure 5.26. For each particle size, 200 particle injection points, spatially distributed at the inlet, were assumed; thus 1200 trajectories were traced for all particle sizes. Initially neutral particles were released into the duct with initial inlet velocity of 0.6 m/s. Under the electrostatic and aerodynamic forces some particles are trapped on the collecting plates and some manage to escape. The deposited particles were assumed to be removed from the model, and particle collision and agglomeration were neglected.

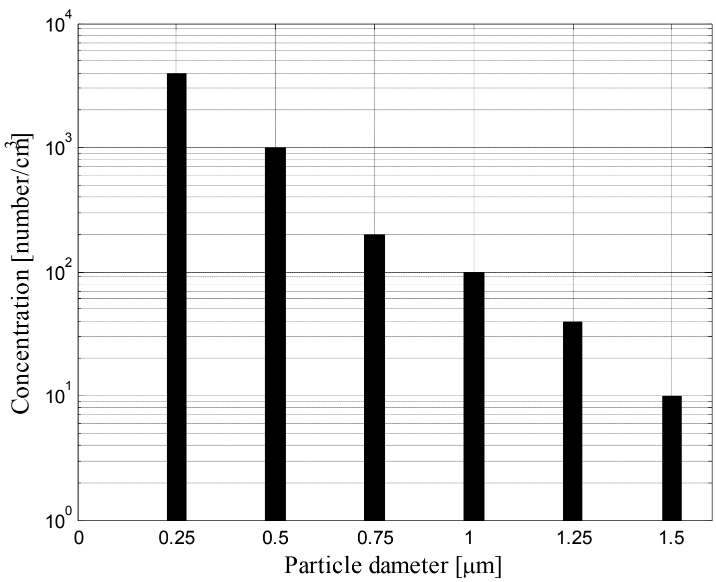

Figure 5.26. Distribution of particle concentration versus particle diameter at inlet.

5.4.3.1 Two-sided spiked electrode

Figure 5.27 shows the predicted collection efficiency of submicron particles with diameters in the range of 0.25-1.5 μm (size distribution shown in Figure 5.26) for different applied voltages. As expected, the particle collection efficiency increases by increasing the applied voltage and decreases for smaller particle size. In Figure 5.28 and Figure 5.29, our numerical results are compared with the experimental data published in [25]. Since the collection efficiency for each particle size is obtained by making an average over the estimated collection efficiencies of ten independent particulate phase simulations, error bars are utilized showing the variations over the average values in the graphs. It is clear that the numerical simulation predicts lower collection efficiency than measured experimentally. We speculate that the larger collection efficiency for particles larger than 0.25 μm reported in the experiments is the result of agglomeration of suspended particles after collisions, and the lower collection efficiency of 0.25 μm particles could be due to the particle re-entrainment to the channel, both of which were neglected in the numerical model.

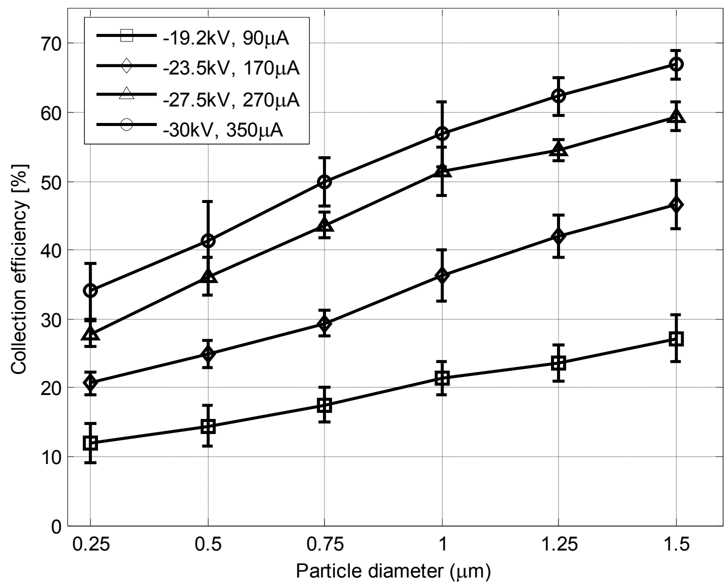

Figure 5.27. Collection efficiency of ESP with spikes on two sides versus particle diameter for four negative applied voltages and inlet velocity of 0.6 m/s calculated from the numerical model.

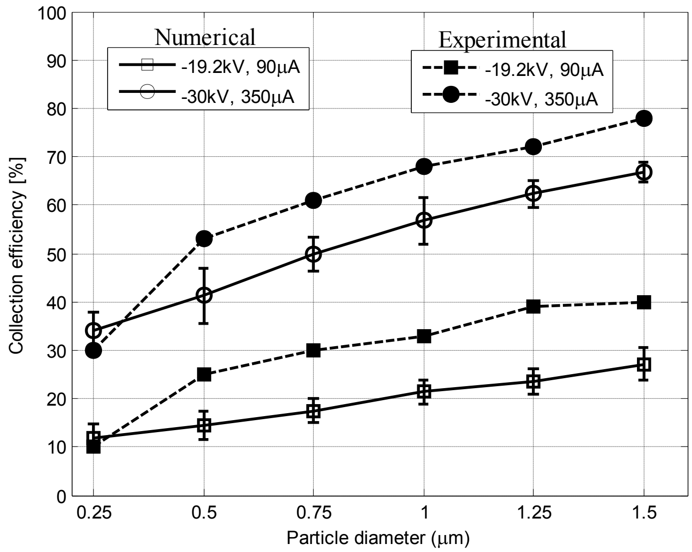

Figure 5.28. Numerical and experimental values of collection efficiency of ESP with spikes on two sides versus particle diameter for -19.2 kV and -30 kV applied voltages and inlet velocity of 0.6 m/s.

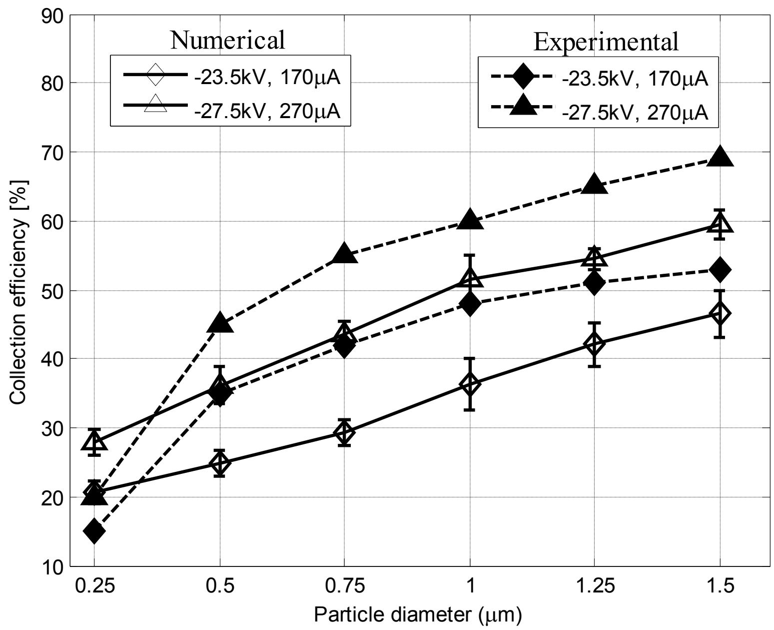

Figure 5.29. Numerical and experimental values of collection efficiency of ESP with spike on two sides versus particle diameter for -23.5 kV and -27.5 kV applied voltages and inlet velocity of 0.6 m/s.

5.4.3.2 One-sided spiked electrode

Figure 5.30 compares the numerical results of particle collection efficiency for all particle sizes and four negative excitation voltages of -19.2, -23.5, -27.5 and -30 kV. As it was expected, the collection efficiency increases with increasing particle size and excitation voltage. For the highest applied voltage (-30 kV), the collection efficiency for 0.25 µm particles is 32% and increases to 54% for 1.5 µm particles. It is also clear that the error bar values showing the standard deviation around the average value of collection efficiency are larger by decreasing the particle size mostly due to strong sensitivity of these particles to the airflow fluctuations in time.

Since submicron particles have very low drift velocity, they mostly follow the airflow streamlines and their trajectories are more affected by the airflow fluctuations than electric forces. Therefore, particle migration velocity (y component of airflow velocity in this case) is a critical parameter for an accurate description of very fine particle transport and removal in turbulent airflow. Figure 5.31 shows the y component of the airflow velocity vector in plane A for the highest (-30 kV) excitation voltage. It is shown that the y component of airflow velocity in the upstream direction of the channel is directed from the center of the channel towards the deposition planes and reaches values up to 0.7 m/s. This velocity pattern is in good agreement with the experimental results presented in [26].

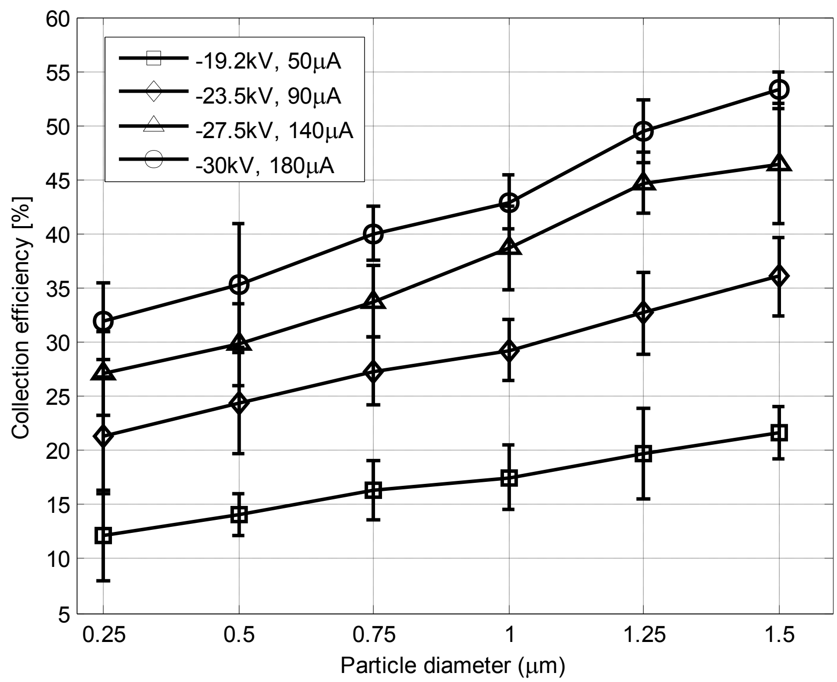

Figure 5.30. Numerical values of collection efficiency of the ESP with spikes pointed in the upstream direction versus particle diameter for four negative applied voltages and inlet velocity of 0.6 m/s.

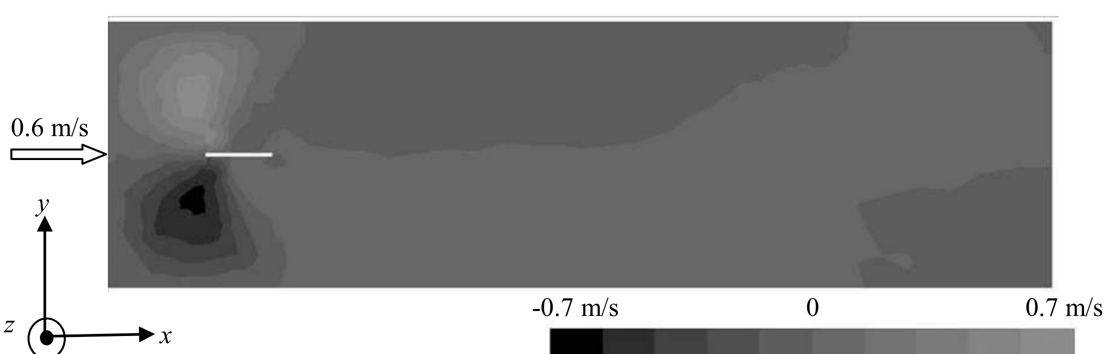

Figure 5.31. *y* component of the airflow velocity in ESP with spikes on upstream direction in plane A (applied voltage is 30 kV and inlet velocity is 0.6 m/s).

Particle collection efficiencies for the whole range of particle sizes estimated for the ESP with spikes in the downstream direction are shown in Figure 5.32. As expected, the collection efficiency increased with increasing applied voltage and particle size. For the highest applied voltage (-30 kV) the collection efficiency for 0.25 μm particles is 26% and increases to 42% for 1.5 μm particles. The decrease in collection efficiency of submicron particles in comparison with the ESP with spikes on upstream direction may be explained by analyzing the airflow velocity pattern shown in Figure 5.33. The *y* component of airflow velocity in an area downstream of the discharge electrode is directed from the center of the channel towards the deposition planes, but reaches lower values of below 0.6 m/s. In the upstream area of the channel a considerable airflow is directed from the collecting plates towards the center of the channel, which means that particles in this part of the channel are repelled from the collecting plates, resulting in reduction of particle collection efficiency. This velocity pattern is in good agreement with the experimental results presented in [26].

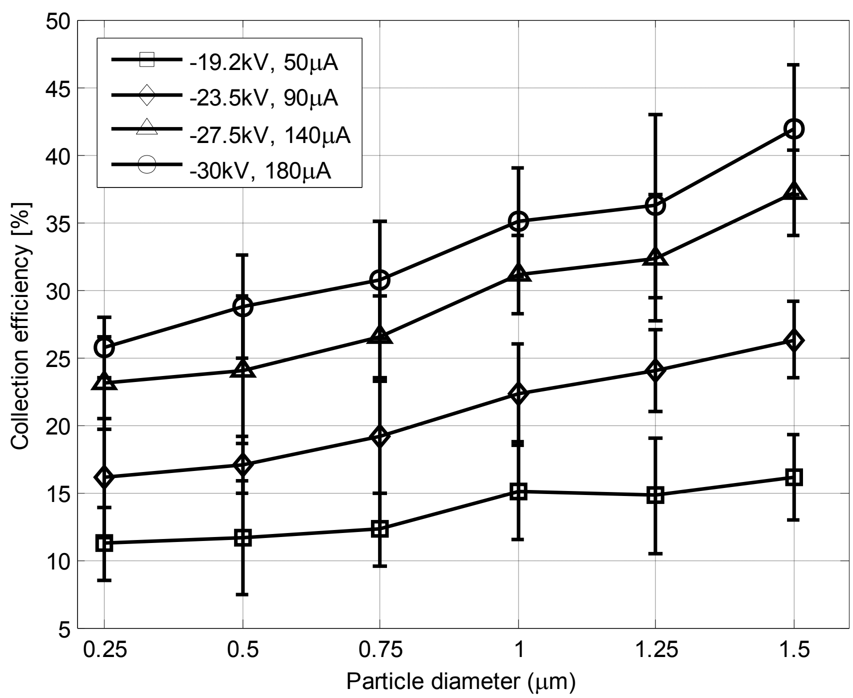

Figure 5.32. Numerical values of collection efficiency of the ESP with spikes in the downstream direction versus particle diameter for four negative applied voltages and inlet velocity of 0.6 m/s.

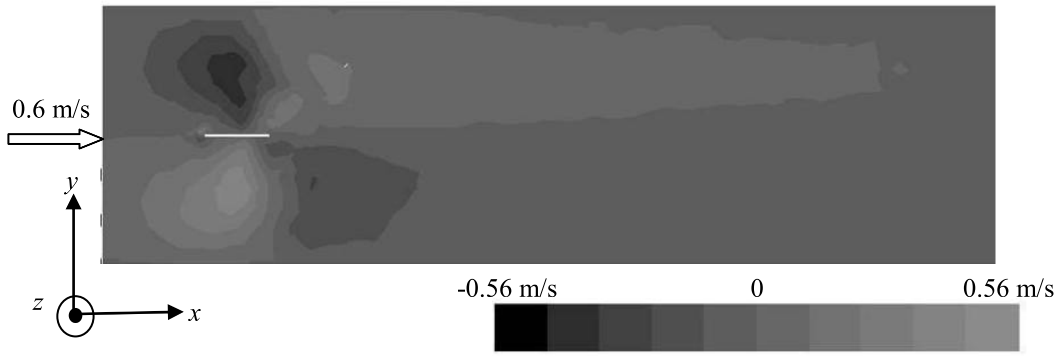

Figure 5.33. y component of the airflow velocity vector in ESP with spikes in downstream direction in the plane A (applied voltage is -30 kV and inlet velocity is 0.6 m/s).

5.4.4 Collection efficiency comparison for three spiked electrode geometries

In Figure 5.34, the collection efficiency of submicron particles for -19.2 kV and -30 kV applied voltages are compared for ESPs with spikes pointed either in the upstream or downstream direction. It is obvious that the estimated particle removal for the ESP with spikes in the upstream direction is always larger due to the significant differences in vortices formation in the channel. Therefore, an ESP with spikes directed upstream is more efficient for fine particle collection than an ESP with spikes directed downstream.

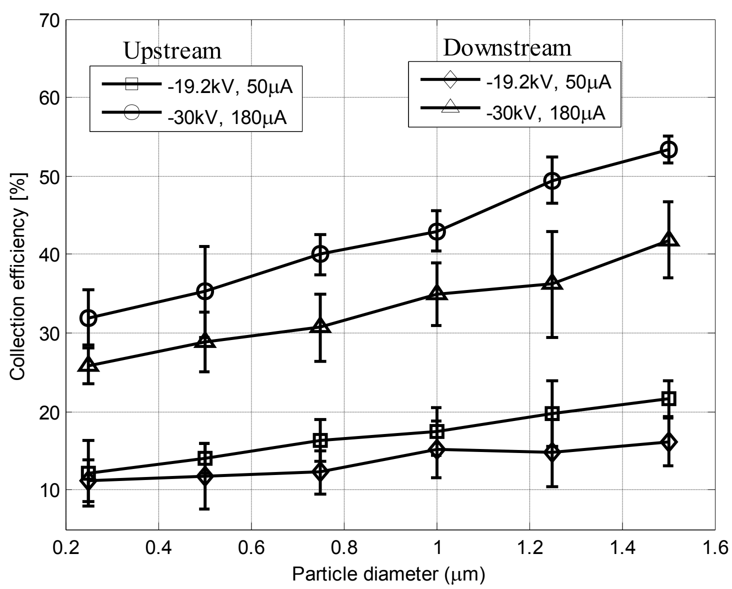

Figure 5.34. Collection efficiency versus particle diameter of ESP with spikes either in upstream or downstream direction for -19.2 kV and -30 kV applied voltages and inlet velocity of 0.6 m/s.

In Figure 5.35a - Figure 5.35d, the collection efficiency of four particle sizes of 0.25, 0.5, 0.75 and 1.5 μm for the three ESP configurations are compared for four negative applied voltages of -19.2, -23.5, -27.5 and -30 kV. It is shown that the ESP with spikes on both sides is the best design for collecting particles in the range of 0.25 -1.5 μm and ESP with spikes on downstream direction has the lowest collection efficiency.

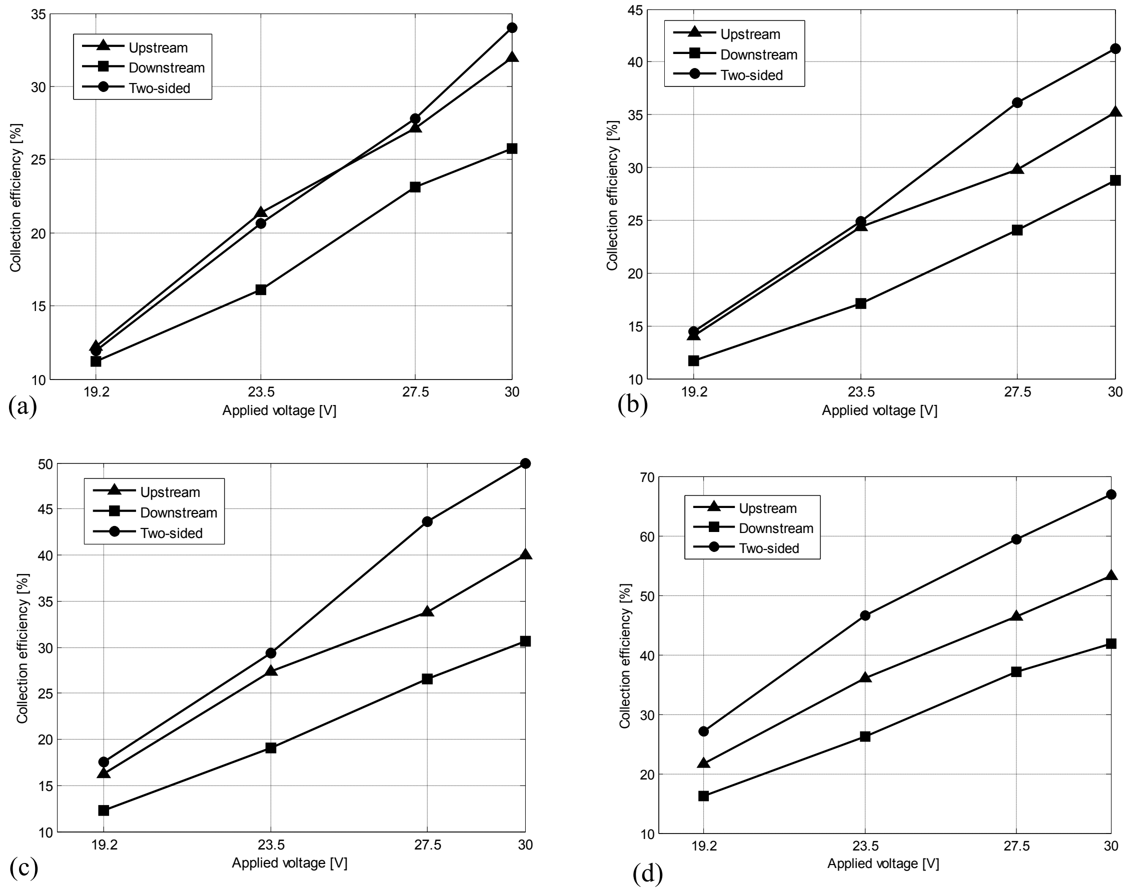

Figure 5.35. Collection efficiency of ESP with spikes on two sides and one side directed either upstream or downstream for different negative applied voltages and particle sizes of (a) 0.25 μm, (b) 0.5 μm, (c) 0.75 μm and (d) 1.5 μm (inlet velocity is 0.6 m/s).

5.4.5 Submicron particle charging, trajectories and deposition

To better demonstrate the influence of spike orientation on the discharge electrode with different excitation voltages on submicron particle collection, the particle deposition rate and average charge to mass ratio in different space intervals along the channel were investigated for -19.2 kV (Figure 5.36 and Figure 5.37) and -30 kV (Figure 5.38 and Figure 5.39) applied voltages and for particle sizes of 0.25, 0.5, 0.75 and 1.5 μm.

Figure 5.36a - Figure 5.36d and Figure 5.38a - Figure 5.38d show the particle deposition rate along the channel for -19.2 kV and -30 kV applied voltages, respectively. It is clear that for ESP with spikes directed upstream and for all particle sizes, the peak values of the particles deposition curves are located in an area upstream of the channel ($x<0$) in the vicinity of discharge electrode, where the two generated vortices in this area push the particles away from the center of the channel towards the deposition planes. For ESP with spikes directed downstream, the two vortices generated in upstream of the channel push the particles away from the collecting plates towards the center of the channel, thus a very small portion of the particles are deposited in this area and the majority of particles is trapped in an area downstream in the channel ($x>0$). For the ESP with spikes on two sides, the particle deposition curves have quite a symmetric pattern around the center of the channel ($x = 0$) and the majority of trapped particles are deposited in vicinity of the discharge electrode.

Figure 5.37a - Figure 5.37d and Figure 5.39a - Figure 5.39d show the corresponding average charge to mass ratio of the deposited particles for -19.2 kV and -30 kV applied voltages. This ratio is increased for all particle sizes as the particles traverse the channel. The results are obtained by calculating an average over the values of charge to mass ratio of a number of particles deposited in a specific space interval along the channel.

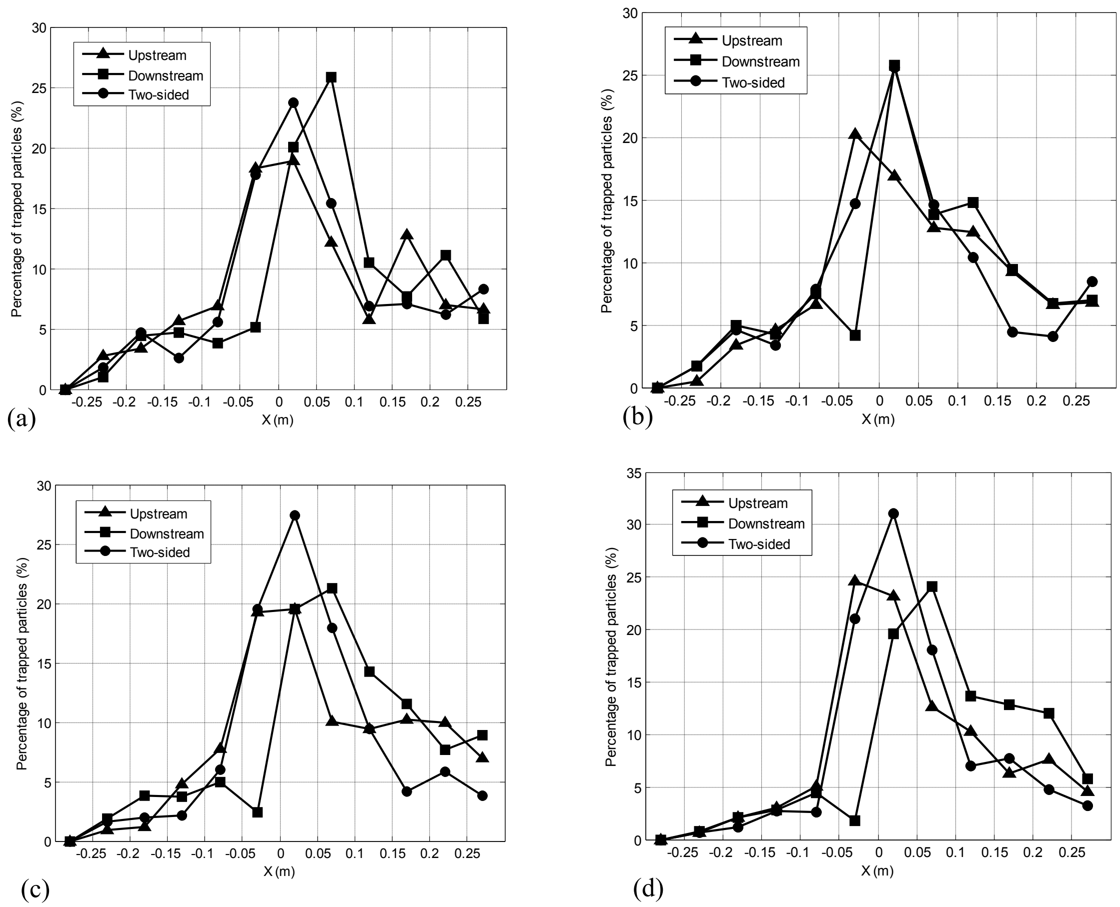

Figure 5.36. Particle deposition rate along the channel for ESP with spikes on two sides and one side directed either upstream or downstream for particle sizes of (a) 0.25 μm, (b) 0.5 μm, (c) 0.75 μm, and (d) 1.5 μm (applied voltage is -19.2 kV and inlet velocity is 0.6 m/s).

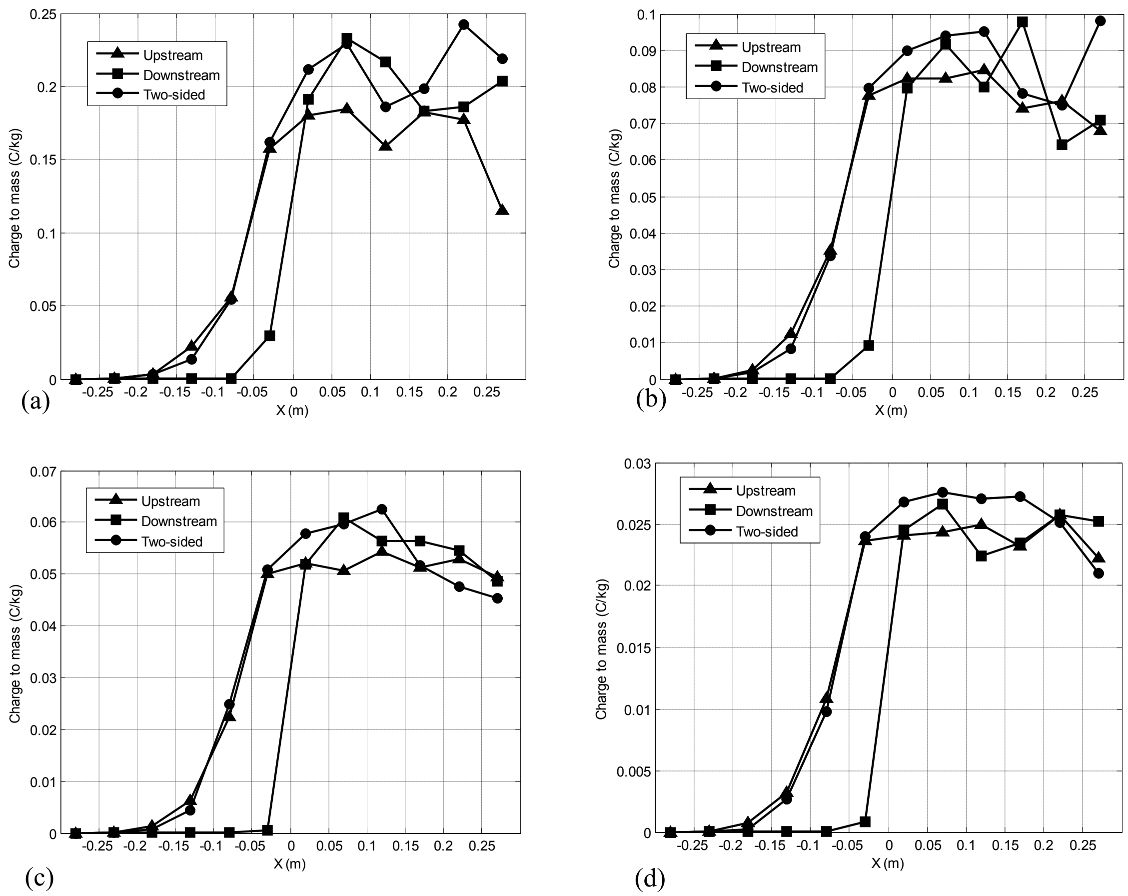

Figure 5.37. Charge-to-mass ratio of deposited particles along channel for ESP with spikes on two sides and one side directed either upstream or downstream for particle sizes of (a) 0.25 μm, (b) 0.5 μm, (c) 0.75 μm and (d) 1.5 μm (applied voltage -19.2 kV and inlet velocity 0.6 m/s).

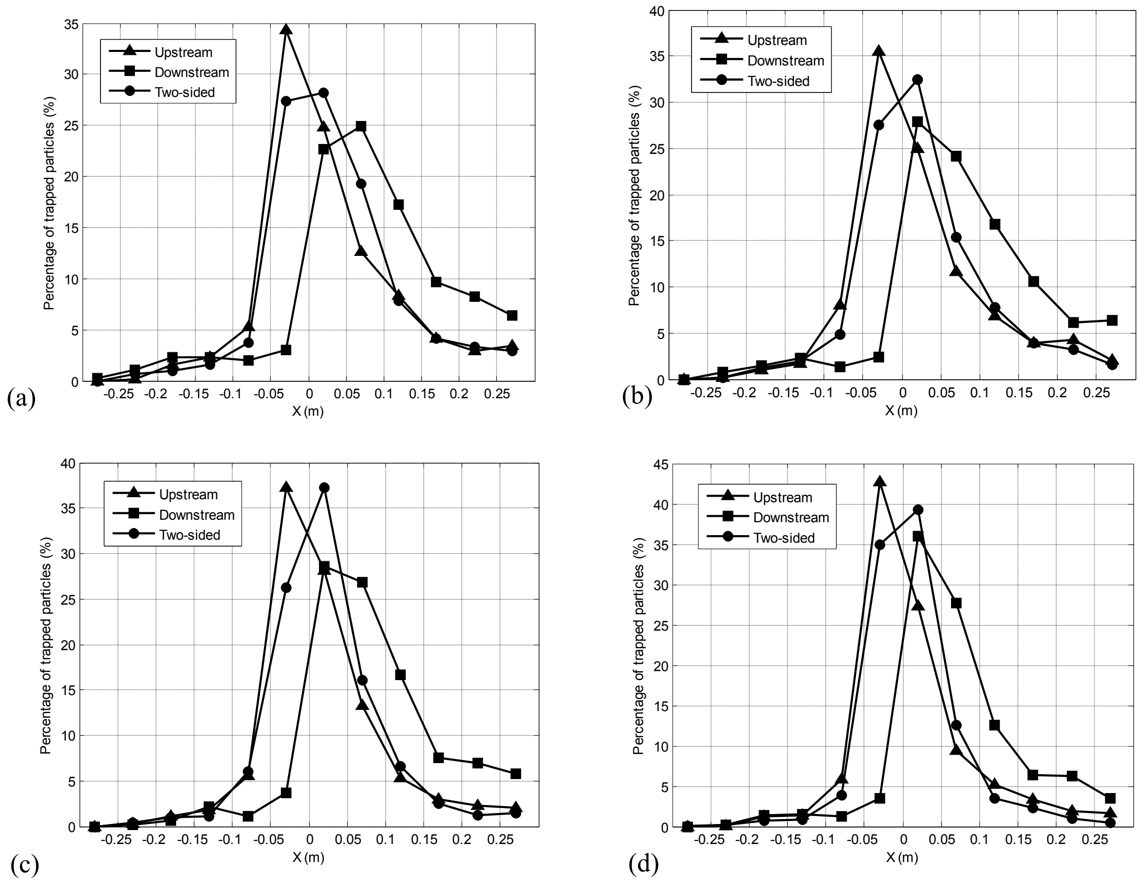

Figure 5.38. Particle deposition rate along the channel for ESP with spikes on two sides and one side directed either upstream or downstream for particle sizes of (a) 0.25 μm, (b) 0.5 μm, (c) 0.75 μm and (d) 1.5 μm (applied voltage -30 kV and inlet velocity 0.6 m/s).

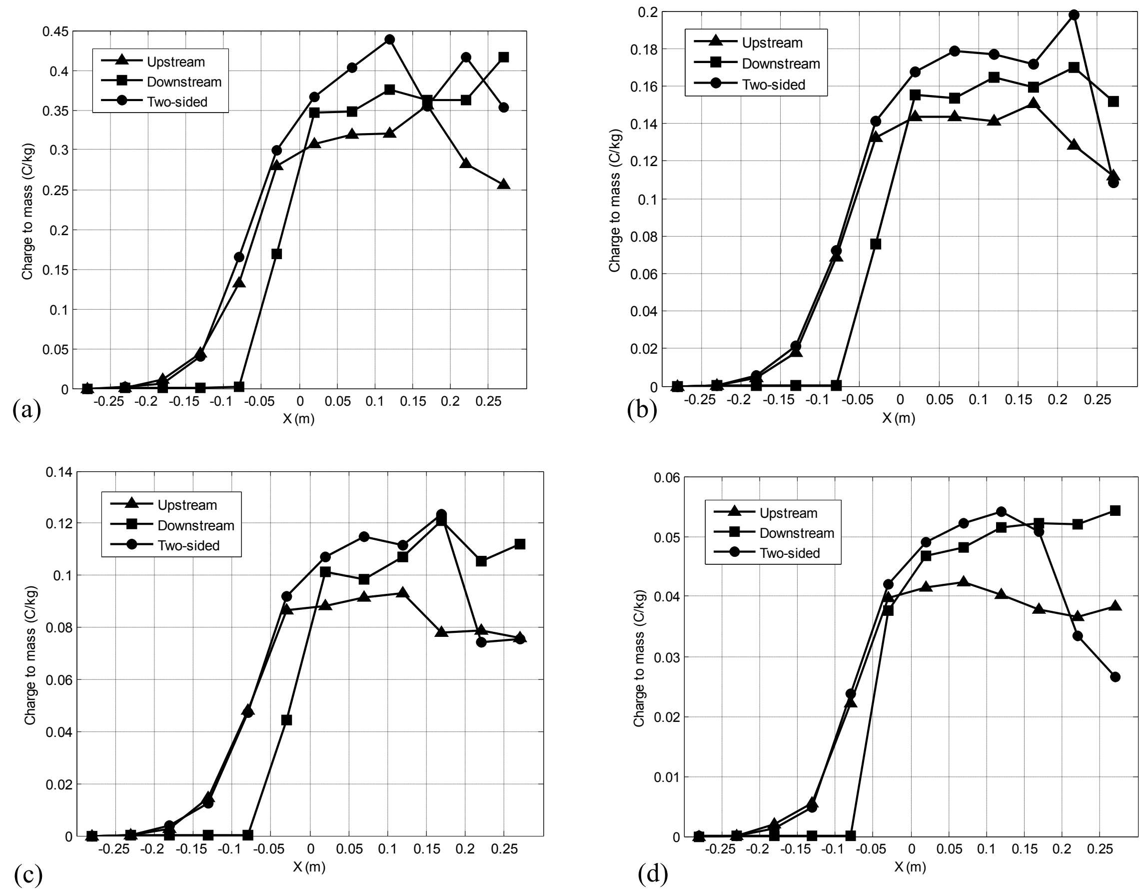

Figure 5.39. Charge-to-mass ratio of deposited particles along the channel for ESP with spikes on two sides and one side directed either upstream or downstream for particle sizes of (a) 0.25 μm, (b) 0.5 μm, (c) 0.75 μm and (d) 1.5 μm (applied voltage -30 kV and inlet velocity 0.6 m/s).

5.4.6 Particle mass flow rate effect on collection efficiency

A larger mass flow rate of particles increases the particle charge density in the channel resulting in changes in the electric field and ionic charge density distributions, which also increases the airflow turbulence in the channel. In order to investigate this effect, the particle mass flow rate at the inlet was increased 20 times and the particle collection efficiencies for 0.25 - 1.5 μm particles were calculated for the ESP with spikes on two sides under negative applied voltage of -30 kV. A 45% reduction in discharge current was assumed, as discussed in Chapter 4. Figure 5.40 compares the particle collection efficiency for all particle sizes assuming the lowest and the highest particle mass flow rate at inlet. It is clear that by increasing the particle mass flow rate the collection efficiency of all particle sizes decreases, which is mainly due to corona current suppression and, thus, decreased particle charge and electrostatic forces acting on the particles.

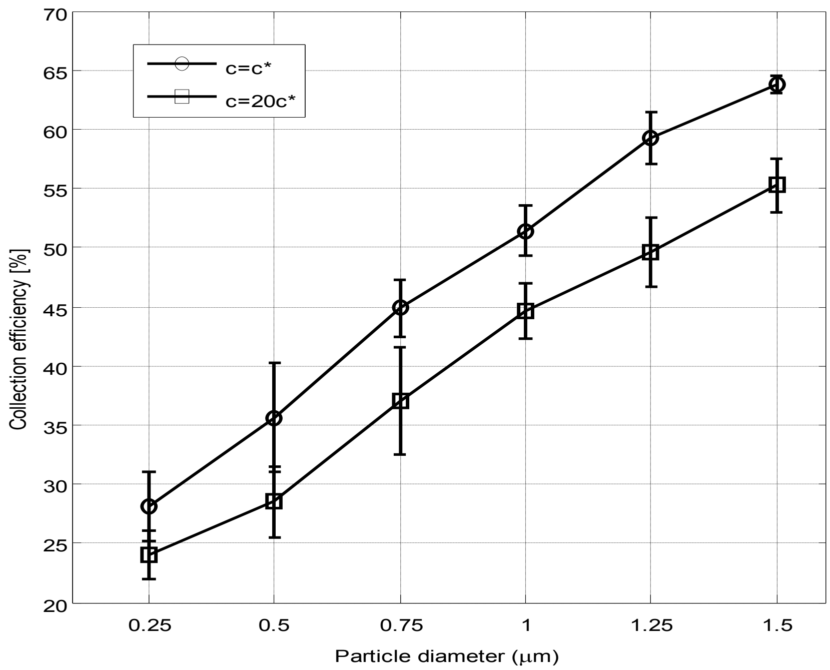

Figure 5.40. Particle collection efficiency versus particle diameter for ESP with spikes on two sides for the lowest (c=c*) and highest (c=20c*) particle mass flow rates at inlet (applied voltage -30 kV and inlet velocity 0.6 m/s).

5.5 Summary

In the first part of this chapter, the developed 3-D numerical technique in Chapter 3 was applied to simulate the electrical and EHD characteristics of a laboratory scale spiked-plate ESP for three geometries of discharge electrodes: two-sided spiked electrode and one-side spiked electrode with the tips directed upstream or downstream of the airflow. Due to the high mobility of the ions produced by the corona discharge, the effect of airflow velocity fluctuations on the ion distribution was neglected. The airflow velocity patterns generated in the channel due to the strong interactions between the main and EHD flows were demonstrated for different applied voltages. The 3-D secondary EHD flow streamlines in different planes of the spike-plate ESP model obtained for various applied voltages show that the strength and dimension of the gas vortices depend not only on the value of the excitation voltage but also on the mutual directions of the secondary EHD and the primary flows. Most of the numerical results obtained in this simulation qualitatively agree with the experimental data presented in [25,26]. Comparing the airflow streamlines obtained for the spiked-type electrode geometry with our previous results presented in Chapter 4, where a smooth corona electrode in a single wire-ESP model was assumed, emphasizes the significant role played by the discharge electrode structure, or discharge pattern, for determining the magnitude and structure of electrically induced flow, and turbulence levels in the channel. Furthermore, this improved modeling and understanding of the secondary EHD flow characteristics in the spiked type precipitator design is crucial for an accurate collection analysis of submicron particles in practical applications. This numerical technique can also be applied for other types of electrode geometry and ESP arrangements.

In the second part of this chapter, the collection efficiencies of submicron particles in a spike electrode-plate laboratory-scale ESP were predicted for three geometries of discharge electrodes. The airflow streamlines, y component of airflow velocity patterns and collection efficiency of particles in the range of 0.25 - 1.5 μm were evaluated and compared for all discharge electrode configurations. It was shown that the ESP with spikes on two sides is the best discharge electrode design for collecting particles in the range of 0.25 - 1.5 μm. The ESP with spikes in the upstream direction showed slightly better collection efficiency for 0.25 μm particles, especially for lower excitation voltages. The particle mass flow rate effect on fine particle collection efficiency for ESP with spikes on two sides at the highest applied voltage (-30 kV) was also investigated. It was shown that increasing the particle mass flow rate at the inlet decreases the particle collection efficiency. A 20 times increase in particle mass flow rate at the inlet resulted in 10% decrease in particle collection efficiency of 1.25 and 1.5 μm particles and about 5-7% decrease for particles in the range of 0.25 to 1 μm. The numerical results were in fairly good agreement with the experimental data published in [25,26].

The content of this chapter has been accepted for publication in two journal papers [115,116].

6. COLLECTION OF ULTRAFINE DIESEL PARTICULATE MATTER IN A CYLINDRICAL SINGLE-STAGE ESP

6.1 Introduction

Long-term exposure to diesel particulate matter emissions are linked to increasing adverse human health effects due to the carcinogenic nature of these particulates. Current diesel vehicular particulate emission regulations are based solely upon total mass concentration, albeit it is the submicron particles that are highly respirable and the most detrimental to human health. The impact of diesel emissions on human health has drawn a great deal of attention from both researchers and governmental agencies seeking a promising and economical control technology.

In this chapter, a wire-cylinder ESP was modeled to predict the collection efficiency of conductive diesel particulates under different conditions. It consists of a circular tube and a wire electrode mounted at the center of the tube, energized by a negative high dc applied voltage, while the tube wall is electrically grounded. The analytical solution of Poisson and current continuity equations was implemented to obtain the ionic space charge density, electric potential distributions and the corresponding electric body forces in the channel. FLUENT commercial software was used to solve the k-ε turbulent airflow equations with considering the electrical body forces. Particle charging and motion equations were solved using the DPM feature of FLUENT and programming the corresponding UDFs.

The corona induced 3-D EHD flow pattern was investigated when the corona wire is slightly off-center (eccentric) in the $z > 0$ direction. The particle deposition rate and average charge-to-mass ratio along the channel, and the collection efficiency of the ESP were evaluated and compared for different particle sizes. The effects of different inlet exhaust gas velocities, excitation voltages and channel length on particle migration velocity and precipitation performance were also assessed.

6.2 Model description

Figure 6.1 shows the schematic illustration of the experimental wire-cylinder ESP used by H. Hayashi *et al*. [77] to collect exhaust gas released from a diesel engine generator (Fuji

Heavy Industries Ltd., SGD3000S-III and maximum power output: 3 kW). The discharge electrode is a stainless steel wire with the diameter of $2r_0$ = 0.2 mm energized with a negative high dc voltage to generate corona discharge. A stainless steel tube with the diameter of $2r_1$ = 36 mm and different lengths of 50-300 mm is used as a collection electrode. The exhaust gas is passed through the precipitator with initial velocities in the range of 0.6 - 1.5 m/s and the mass concentration of 20 mg/m^3. The diesel engine generator was tested in two modes: low load (0 W) and high load (2.6 kW). It was proven that the ratio of Soluble Organic Fraction (SOF) consisting of unburned fuel and lubricant decreases at the high load of the engine [77]. Typical size of diesel aerosols is in the range of 10-1000 nm and has a constant density with a value between 1000 and 1500 kg/m^3. Figure 6.2a and Figure 6.2b show two number concentrations of diesel particulates assumed at the inlet, for engine at low load and high load conditions and 110^o C and 210^o C temperature of the exhaust gas, respectively. Groups of each particle size were injected from 248 points from the inlet resulting in total number of 7440 and 6696 particle streams in the ESP channel for engine at zero and high loads, respectively. In this simulation, particle density of 1000 kg/m^3 was considered. Since the diesel particulates are conductive, the saturation charge was obtained by assuming the particle relative permittivity equal to infinity. A constant velocity at the inlet and "outflow" boundary condition at the outlet were imposed. Depending on the diesel engine load, a constant temperature of 110^o C or 210^o C was assigned for the boundary conditions of the walls.

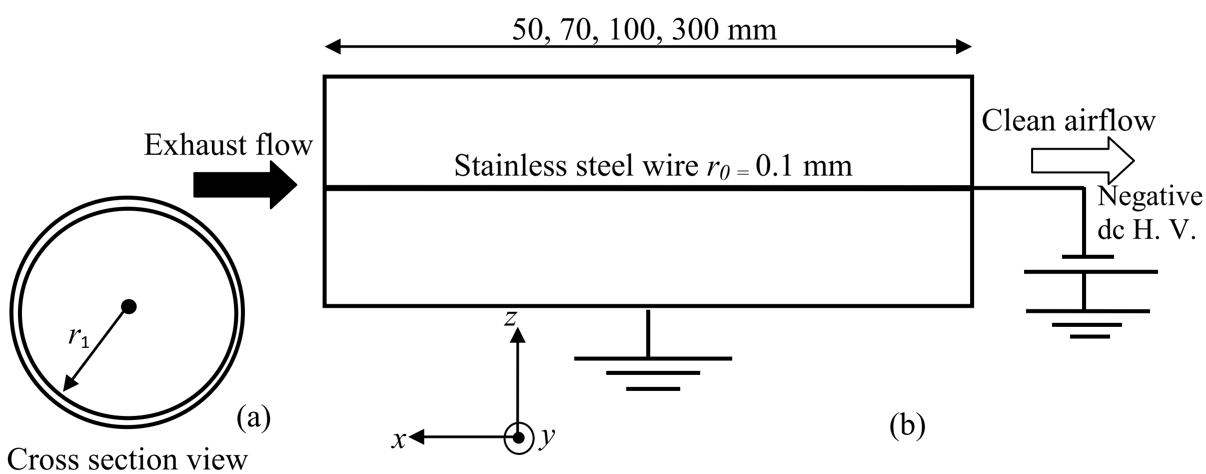

Figure 6.1. Schematic diagram of wire-cylinder ESP channel (a) cross section (b) side view.

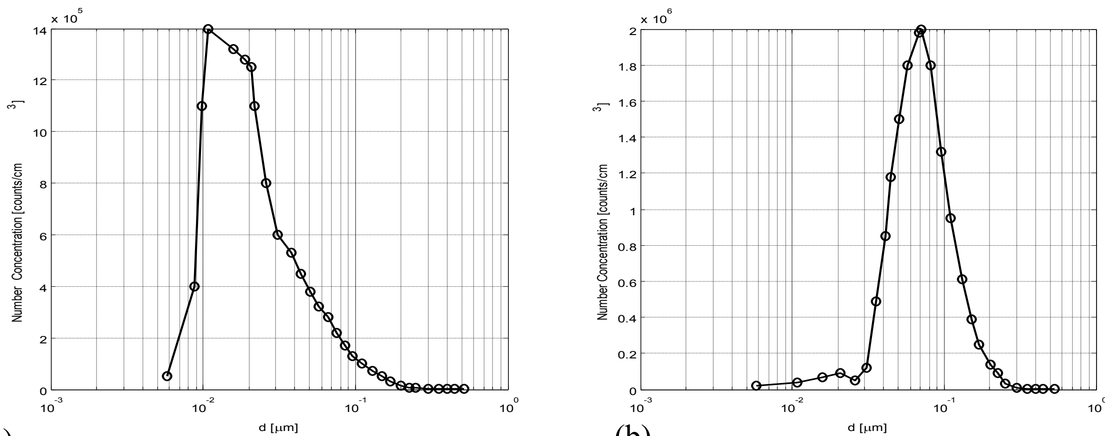

(a) (b)

Figure 6.2. Number concentration versus exhaust particle diameter at inlet for (a) zero engine load and 110° C temperature (b) high engine load and 210° C temperature

6.3 Simulation results and discussions

The whole computational domain was discretized into a number of tetrahedral elements using the commercial software GAMBIT, Table 6.1, with very fine elements in the vicinity of the wire electrode and larger elements in the vicinity of the collecting tube.

Table 6.1. Number of nodes and elements from discretization for different channel lengths

Channel length (mm)	# Tetrahedral elements	# Nodes
50	88363	17048
70	117694	22392
100	164155	30827
300	466398	85757

The exact analytical solution for solving the Poisson and current continuity equations for wire-cylinder geometry in [117] was utilized to obtain the electric potential, Φ , electric field, $\vec{E}$, and ion charge density distributions, ρ_i in the precipitation channel for different applied voltages. Considering [r_0, r_1] the region of interest as shown in Figure 6.1a, the closed form of the solution is as follows:

$$\Phi(r) = \Phi_0 - k_1 \left\{ f_1(r) - k_2 + k_3 [\ln \frac{r}{r_1} + \ln(k_3 + k_2) - \ln(k_3 + f_1(r))] \right\}$$
$$E(r) = \frac{k_1}{r} f_1(r) \tag{6-1}$$

Electric field is directed radially outward for $\Phi_0 > 0$

$$\rho_i(r) = \frac{\sqrt{r_0 E_p \varepsilon_0 \rho_0}}{f_1(r)} \tag{6-2}$$

where $k_1 = \sqrt{\frac{r_0 E_p \rho_0}{\varepsilon_0}}$, $f_1(r) = \sqrt{r^2 + k_2^2 - r_0^2}$, $k_2 = \sqrt{\frac{r_0 E_p \varepsilon_0}{\rho_0}}$ and $k_3 = \sqrt{k_2^2 - r_0^2}$.

$\rho_0 = \rho_i(r_0)$ is determined implicitly from the following transcendental equation:

$$\Phi_0 = k_1 \left\{ f_1(r_1) - k_2 + k_3 [\ln \frac{r_1}{r_0} + \ln(k_3 + k_2) - \ln(k_3 + f_1(r_1))] \right\} \tag{6-3}$$

where Φ_o is the applied voltage and E_p is the electric field strength at the surface of the corona wire, equal to the onset value in air (Peek's formula Eq. (3-41)).

It was assumed that the ionic charge distribution in the channel would not be disturbed by the airflow and only the strong effect of electrostatic forces, due to the presence of ionic space charge in electric fields, on the airflow patterns was considered. The airflow equations were solved inside FLUENT using FVM and the turbulence effect was included by using the *k-ε* model. The Lagrangian random walk approach was used to determine particle motion, as affected by EHD flows and turbulence effects. This part was performed with the aid of DPM module in FLUENT considering submicron particle charging equations. The detailed description of the methodology and procedures can be found in Chapter 3.

6.3.1 Electrical characteristics - analytical solution

6.3.1.1 Zero engine load and T= 110°C

Figure 6.3a and Figure 6.3b show the analytical solutions for electric potential and electric field strength distributions along the radial direction under different voltages applied to the corona wire, where the engine is at zero load condition and temperature is 110° C. The coresponding ionic charge density distributions are also shown in Figure 6.4a and Figure 6.4b.

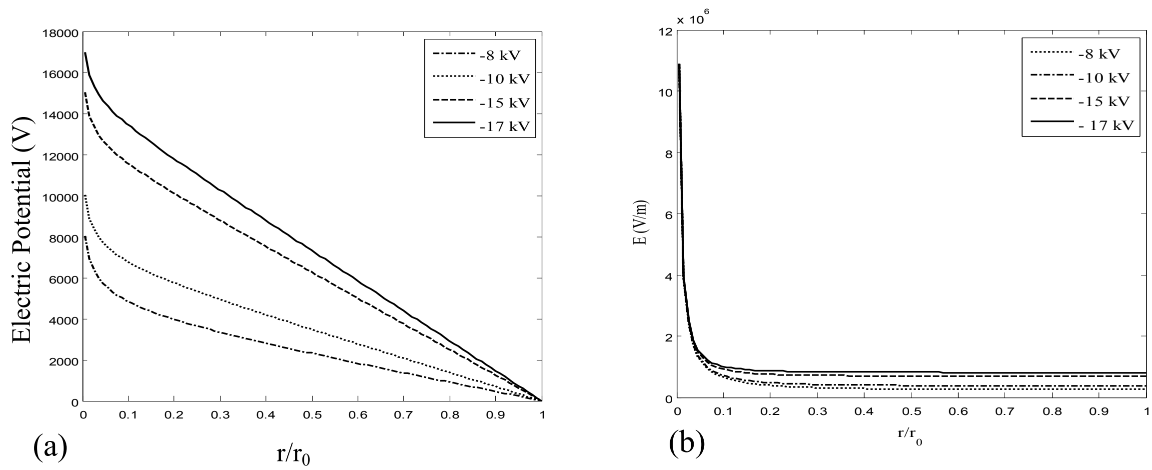

Figure 6.3. (a) Electric potential and (b) electric field strength distribution along the radial direction (zero engine load at T = 110° C)

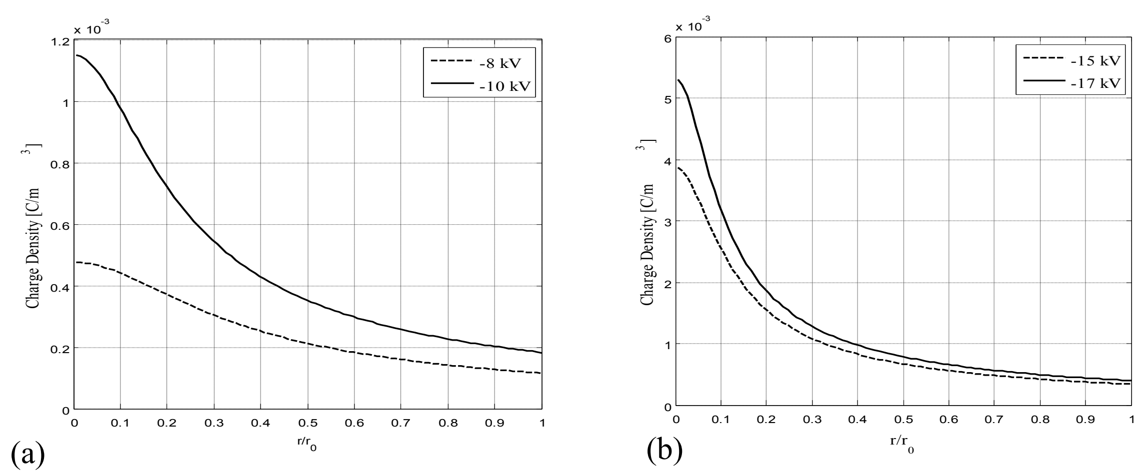

Figure 6.4. Charge density distribution along the radial direction for applied voltages of (a) -8 kV and -10 kV (b) -15 kV and -17 kV for the engine at zero load and T = 110° C

The electric field strength near the collecting tube, E_{CE} in Eq. (3-36), pseudo-homogeneous electric field strength, E_{ps} in Eq. (3-34), electric field strength (E_p) and ionic charge density (ρ_0) values on the corona wire surface, corona discharge current (I) and the electric power of the wire-cylinder ESP for different applied voltages are summarized in Table 6.2.

Table 6.2. Electrical parameters of wire-cylinder ESP (engine load is zero and $T = 110^o$ C)

Applied Voltage	E_{CE} **(kV/m)**	E_{ps} **(kV/m)**	E_p **(kV/m)**	ρ_0 **(μC/m^3)**	***I*** **(μA)**	***Power*** **(W)**
-8 kV	260	440	11000	-475	110	0.9
-10 kV	370	555	11000	-1150	271	2.7
-15 kV	740	833	11000	-3850	910	13.6
-17 kV	870	870	11000	-5300	1300	22.1

6.3.1.2 High engine load and $T = 210^o$C

The ionic charge density distribution along the radial direction for the engine at high load condition and temperature of 210^o C are shown in Figure 6.5a and Figure 6.5b for different voltages applied to the corona wire. Other electrical parameters of interest are summarized in Table 6.3. It is clear that in this case higher values of ionic charge density are generated in the channel resulting in higher electric field strength near the collecting tube and higher electric power consumption.

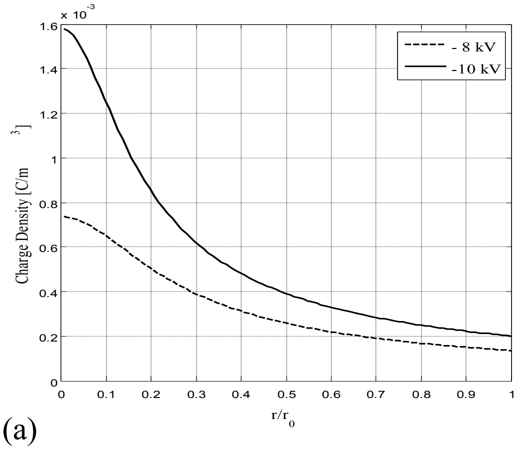

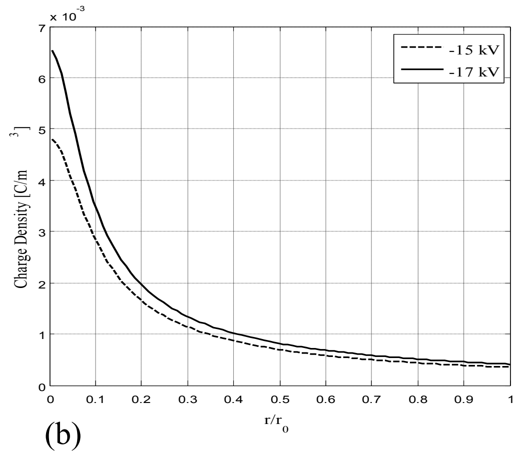

Figure 6.5. Charge density distribution along the radial direction for applied voltages of (a) -8 kV and -10 kV (b) -15 kV and -17 kV for the engine at high load and $T = 210^{o}$ C

Table 6.3. Electrical parameters of wire-cylinder ESP (engine load is high and $T = 210^{o}$ C)

Applied Voltage	E_{CE} **(kV/m)**	E_{ps} **(kV/m)**	E_p **(kV/m)**	ρ_i **(μC/m³)**	***I*** **(μA)**	***Power*** **(W)**
-8 kV	302	440	9400	-730	190	1.5
-10 kV	381	555	9400	-1580	410	4.1
-15 kV	770	833	9400	-4800	1200	18.0
-17 kV	900	870	9400	-6550	1700	28.9

6.3.2 3-D EHD flow patterns

The EHD secondary flow generated due to electrostatic body forces on the air molecules was investigated in this model. It was found that in a perfectly concentric configuration of the electrode, the secondary flow does not exist due to symmetry of the geometry, where the electric body force is balanced by the pressure force along the radial direction, which was proven in [84]. Therefore, a slightly eccentric configuration was considered by displacing the corona wire a small radial distance. In this case the average electric body force on the sides of the electrode are imbalanced and the air molecules along the eccentricity direction experience stronger average body force and are driven away from the electrode to form a jet. Assuming 1% electrode eccentricity in the $z > 0$ direction, a corona-induced jet is developed along the eccentricity direction with two spiral vortices on either sides of the jet, where the vortex on the right rotates counter clockwise, and the vortex on the left rotates clockwise, as shown in Figure 6.6a and Figure 6.6b. Theses vortices occupy almost the whole area of the circular cross section.

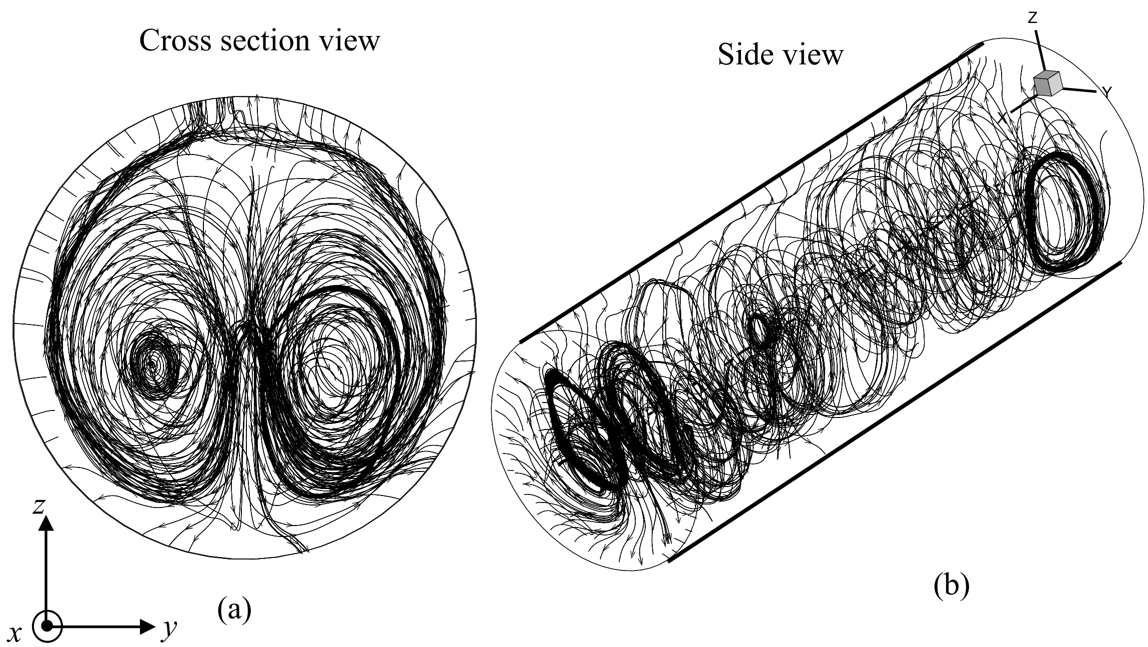

Figure 6.6. EHD secondary flow streamlines for 1% offset of corona discharge electrode from the center of the ESP channel (a) cross section view (b) side view.

6.3.3 Submicron particles charging, trajectories and deposition

Once the continuous phase (airflow) was calculated taking into account the external electrostatic body forces in Eq. (3-7), inert submicron particles were introduced to the system and their trajectories, charging and deposition was tracked. Both field and diffusion charging mechanisms, Eq. (3-30), were considered for charging the injected particles. Since the concentration of the submicron particles was very small, the effect of particle charge in the Poisson equation, Eq. (3-32), was neglected. Particle motion equations, Eq. (3-18), were solved considering the Stokes' drag law, Eq. (3-26), for calculating the drag forces. The

Cunningham slip correction factor, C_c, was computed from Eq.(3-27) for the engine at zero load and high load conditions and under different operating temperatures, as shown in Figure 6.7a and Figure 6.7b.

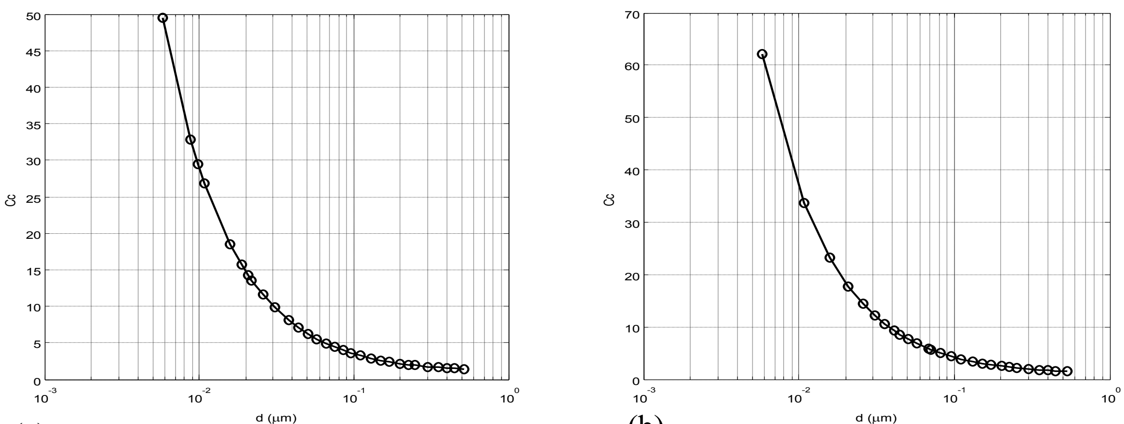

Figure 6.7. Cunningham slip correction factor versus exhaust particle diameter (a) zero engine load and $T = 110^{o}$ C (b) high engine load and $T = 210^{o}$ C

6.3.3.1 Zero engine load and $T = 110^{o}$ C

Particle charge to mass ratio and deposition rate along the ESP channel length for the particle sizes of 30 nm, 100 nm, 200 nm and 500 nm are shown in Figure 6.8 - Figure 6.11 respectively, assuming diferent inlet velocities of 0.6 m/s, 1.0 m/s and 1.5 m/s, zero engine load and -10 kV excitation voltage applied to the corona wire. For the 30 nm particles the Cunningham slip correction factor, shown in Figure 6.7a, has the highest value, thus the drag forces on these particles are minimal. Despite of the negligible effect of electrostatic forces acting on these particles, a high deposition rate in the upstream direction of the channel can be seen (Figure 6.8b). Figure 6.8a shows that after increasing the inlet velocity the particles travel faster in the ESP channel and the charge to mass ratio decreases. The same trend can be observed for larger particles of 100, 200 and 500 nm (Figure 6.9 -Figure 6.11). The charge to mass ratio of particles increases as the particles traverse the channel. However, due to a higher amount of charge accumulated by larger particles in the same time, they obtain the saturated charge quicker and the velocity effect on charge to mass ratio, Figure 6.11a, becomes negligible. The particle deposition rates in Figure 6.8b- Figure 6.11b demonstrate some fluctuations along the channel which is due to the stochastic movement of these particles in the channel. In the simulations, the discrete random walk model (DRW) was activated in FLUENT taking care of particle dispersion in the turbulent flow. Therefore, particle trajectories are subjected to turbulence dispersion which is effective in all directions as well as drag forces in the flow direction and electrostatic forces in wall normal direction.

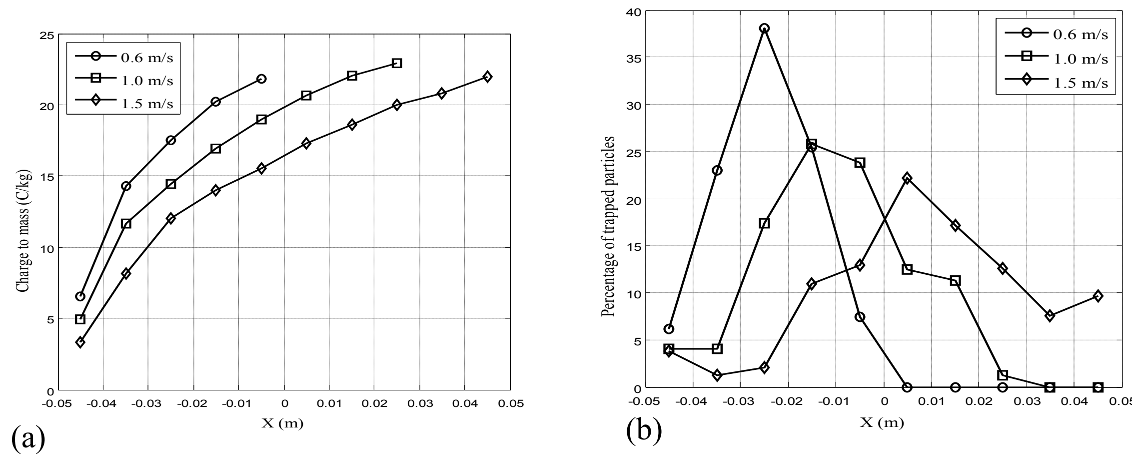

Figure 6.8. (a) Charge to mass ratio and (b) percentage of trapped particles along the ESP channel for 30 nm particles under three inlet velocities (applied voltage is -10 kV, channel length is 100 mm, and temperature is 110^o C)

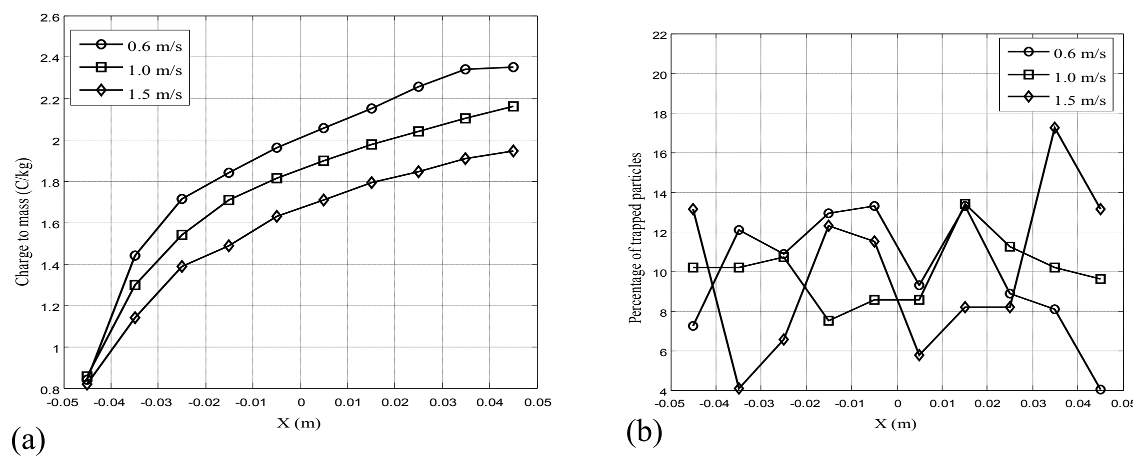

Figure 6.9. (a) Charge to mass ratio and (b) percentage of trapped particles along the ESP channel for 100 nm particles under three inlet velocities (applied voltage is -10 kV, channel length is 100 mm, and temperature is 110^{o}C)

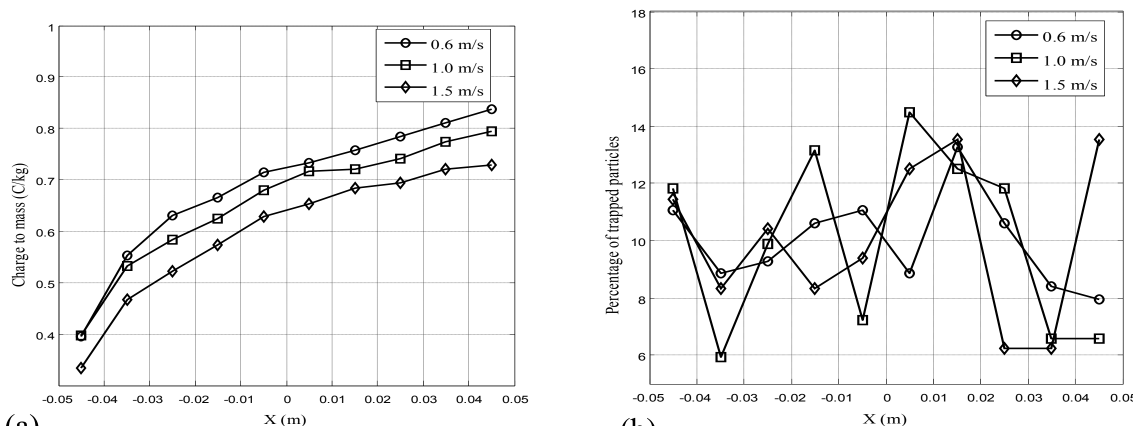

Figure 6.10. (a) Charge to mass ratio and (b) percentage of trapped particles along the ESP channel for 200 nm particles under three inlet velocities (applied voltage is -10 kV, channel length is 100 mm, and temperature is 110^{o}C)

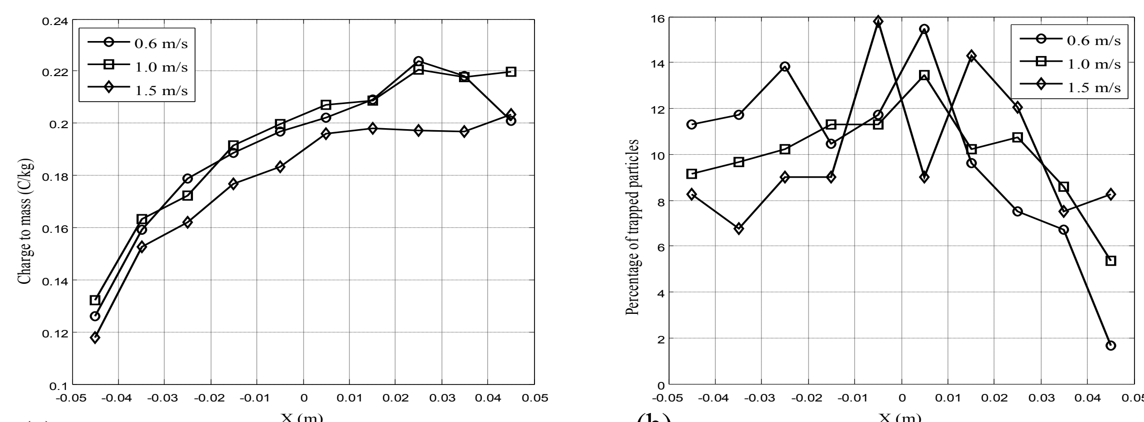

Figure 6.11. (a) Charge to mass ratio and (b) percentage of trapped particles along the ESP channel for 500 nm particles under three inlet velocities (applied voltage is -10 kV, channel length is 100 mm, and temperature is 110^{o} C)

6.3.3.2 High engine load and $T = 210^{o}$C

Particle charge to mass ratio and deposition rate along the ESP channel length for the particle sizes of 40 nm, 100 nm, 300 nm and 500 nm are shown in Figure 6.12 - Figure 6.15, respectively, assuming different inlet velocities of 0.6 m/s, 1.0 m/s and 1.5 m/s, high engine load and -10 kV excitation voltage applied to the corona wire.

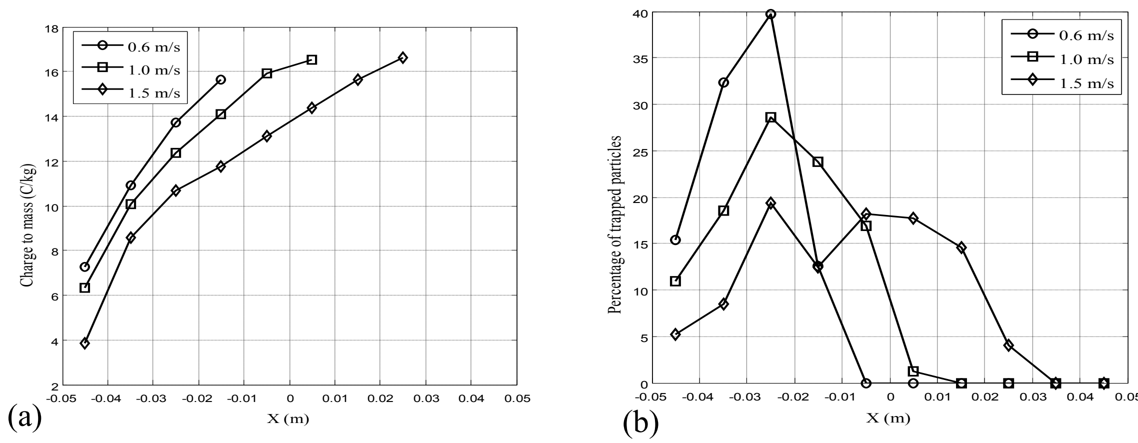

Figure 6.12. (a) Charge to mass ratio and (b) percentage of trapped particles along the ESP channel for 40 nm particles under three inlet velocities (applied voltage is -10 kV, channel length is 100 mm, and temperature is 210^{o} C)

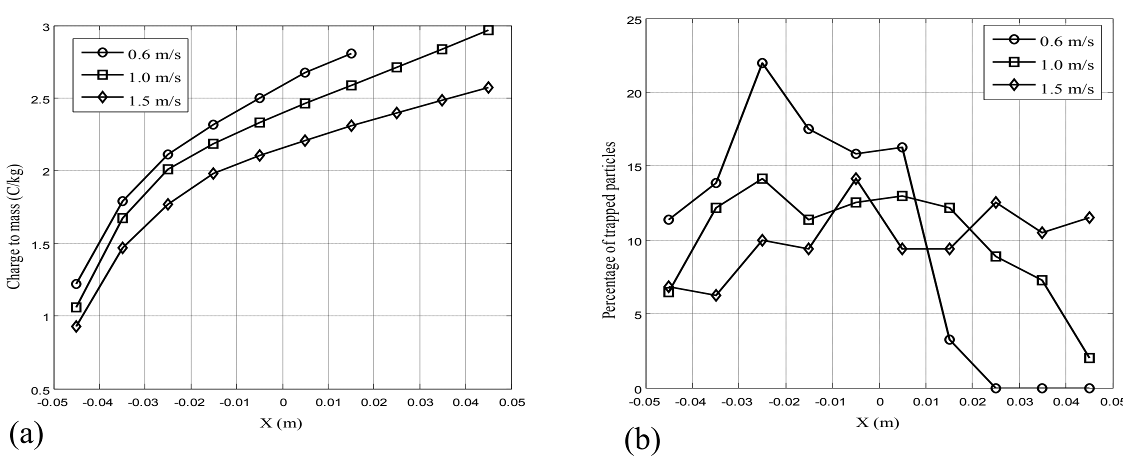

Figure 6.13. (a) Charge to mass ratio and (b) percentage of trapped particles along the ESP channel for 100 nm particles three inlet velocities (applied voltage is -10 kV, channel length is 100 mm, and temperature is 210^{o} C)

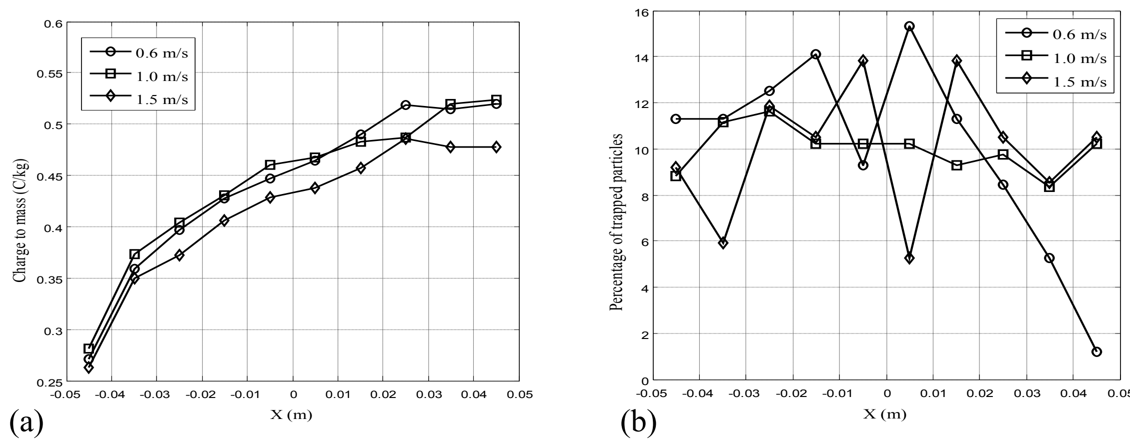

Figure 6.14. (a) Charge to mass ratio and (b) percentage of trapped particles along the ESP channel for 300 nm particles under three inlet velocities (applied voltage is -10 kV, channel length is 100 mm, and temperature is 210^{o} C)

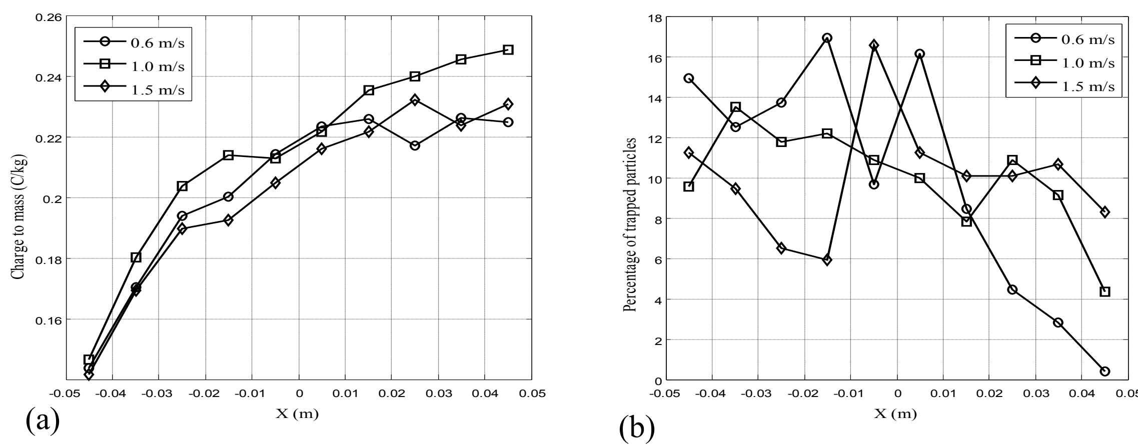

Figure 6.15. (a) Charge to mass ratio and (b) percentage of trapped particles along the ESP channel for 500 nm particles under three inlet velocities (applied voltage is -10 kV, channel length is 100 mm, and temperature is 210^{o} C)

6.3.4 Migration velocity and particle residence time

6.3.4.1 Zero engine load and *T*= 110^{o} C

Figure 6.16a and Figure 6.16b compare the particle migration velocity obtained from the simulation with the theoretical migration velocity under different voltages applied to the corona wire, three different inlet velocities of 0.6, 1.0 and 1.5 m/s and engine at zero load condition. The theoretical migration velocity was calculated using Eq. (3-36), where the saturation charge on each particle size was estimated using Cochet charging model [95], Eq. (3-33). It is clear that the migration velocity obtained from the numerical model is larger than the theoretical values for all particle sizes. Therefore, it is most likely that the saturation charge estimated by Cochet charging model is smaller than the actual values of the calculated charge on particles. In our simulation model, particles smaller than 20 nm obtain no charge or at most one electron charge as they traverse the whole length of the ESP channel and their trajectories are only affected by airflow drag forces, thus, practically these particle could not be trapped by the ESP. Therefore, the numerical results in this chapter are only valid for particles larger than 20 nm. According to these figures, the migration velocity increases by increasing the voltage applied to the corona wire electrode. For a specific voltage applied to the corona wire the migration velocity for each particle size is approximately the same for inlet velocities of 0.6, 1.0 and 1.5 m/s. It means that at this range of inlet velocities, particles still have enough time to obtain the saturated charge in the channel. However, it is expected that at a specific inlet velocity, the migration velocity starts to drop dramatically due to decrease in particle residence time in the channel.

In addition, Figure 6.16a and Figure 6.16b, show that particle migration velocity has a minimum around 200-300 nm particle diameter. This can be theoretically explained as follows:

For particles larger than 300 nm, when field charging is dominant, the particle saturation charge and the theoretical particle migration velocity is [43]:

$$
\begin{aligned}
Q_p(d_p) &= Q_s = \frac{3\varepsilon_r}{\varepsilon_r + 2}\pi\varepsilon_0 d_p^2 \left|\vec{E}_{CE}\right| \\
\varpi_{th} &= \frac{Q_s}{3\pi\mu d_p}\left|\vec{E}_{CE}\right| = \frac{\varepsilon_0\varepsilon_r}{\mu(\varepsilon_r + 2)} d_p \left|\vec{E}_{CE}\right|^2
\end{aligned}
\qquad (6\text{-}4)
$$

In this case, the migration velocity is proportional to the particle diameter, and the square of the field strength. Therefore, particle migration velocity increases by increasing the particle diameter. For particles smaller than 200 nm, the correction factor C_c, necessary to account for viscosity and the diffusion charging, is dominant. The particle saturation charge from diffusion charging and the corresponding migration velocity is [43]:

$$Q_p(d_p) = Q_s = 6.2\frac{2\pi\varepsilon_0 d_p k_B T}{e}$$

$$\varpi_{th} = \frac{C_c(\lambda)Q_s}{3\pi\mu d_p}\left|\vec{E}_{CE}\right| = 6.2\frac{2\pi\varepsilon_0 d_p k_B T}{3\pi\mu d_p e}\left|\vec{E}_{CE}\right|C_c(\lambda) = \frac{4\varepsilon_0 k_B}{\mu e}T\left|\vec{E}_{CE}\right|C_c(\lambda) \tag{6-5}$$

In this case the migration velocity is proportional to the temperature, electric field strength and the Cunningham slip correction factor. To simplify the equations, for both cases the electric field strength near the collecting plates, $\left|\vec{E}_{CE}\right|$, can be roughly estimated by pseudo-homogeneous electric field strength , $\left|\vec{E}_{ps}\right|$.

Figure 6.17a - Figure 6.17d compare the particle residence time of deposited particles for four applied voltages of -8 kV, -10 kV, -15 kV and -17 kV, for inlet velocities of 0.6 m/s, 1.0 m/s and 1.5 m/s, respectively. In general, the particle residence time for each particle size decreases by increasing the excitation voltage *i.e.* these particles are trapped earlier in the channel due to higher amount of charge obtained by them in a specific period of time and stronger electrostatic forces. For larger applied voltages with higher ionic charge density in the channel, the residence time of each particle size is the same for the three inlet velocities, as shown in Figure 6.17c and Figure 6.17d. However, for lower excitation voltages the particle residence time decreases by increasing the inlet velocities, as shown in Figure 6.17a and Figure 6.17b. It is also clear that the graphs for particle residence time have a maximum around 200-300 nm particle diameter for all excitation voltages and inlet velocities.

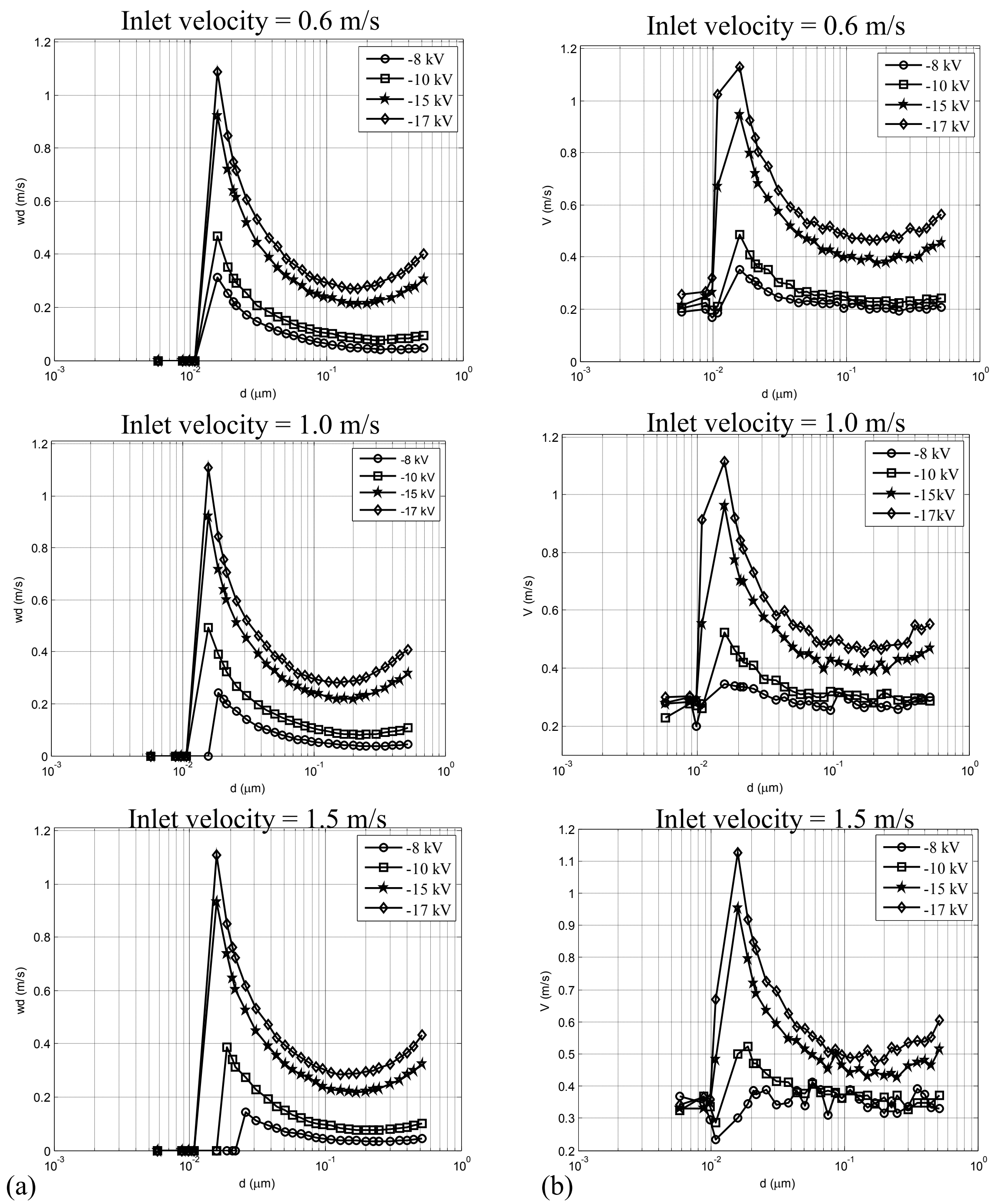

Figure 6.16. (a) Theoretical migration velocity calculated from Cochet particle charging model (b) particle migration velocity obtained from simulation for different applied voltages, channel length of 100 mm and inlet velocities of 0.6 m/s, 1 m/s and 1.5 m/s

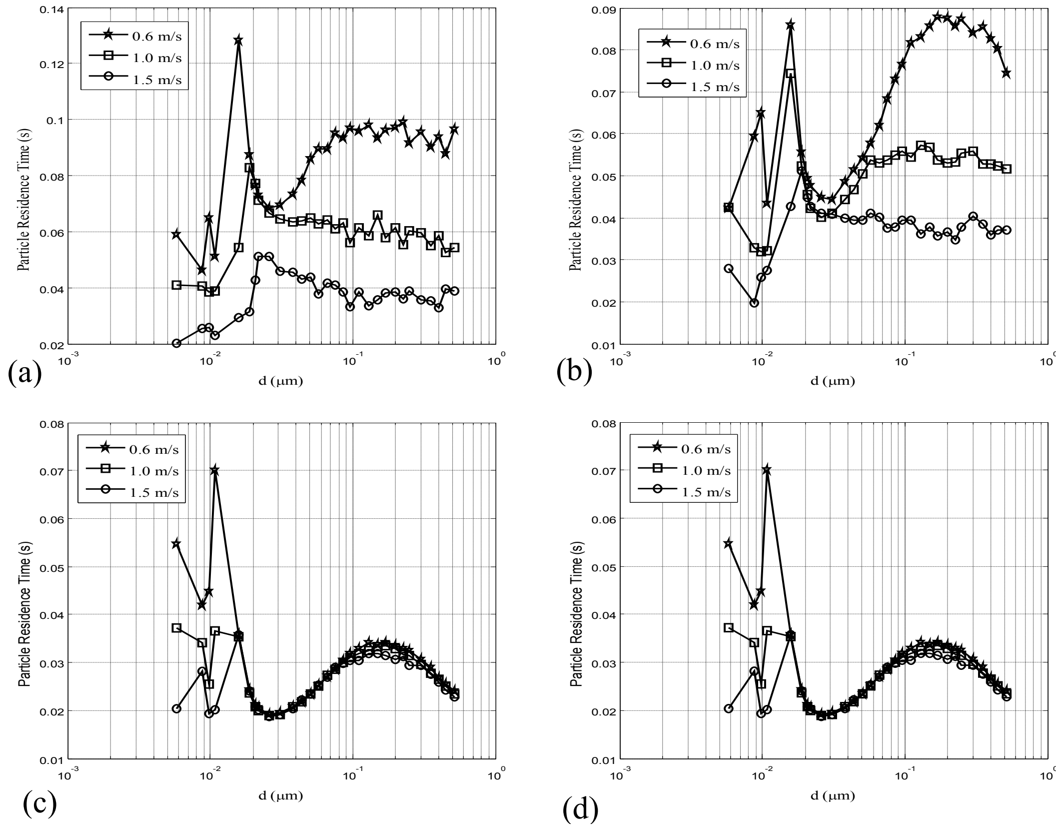

Figure 6.17. Particle residence time of deposited particles versus exhaust particle diameter for three inlet velocities, channel length of 100 mm and different applied voltages of (a) -8 kV, (b) -10 kV, (c) -15 kV and (d) -17 kV.

6.3.4.2 High engine load and $T = 210^{o}$ C

Figure 6.18a and Figure 6.18b compare the particle migration velocity obtained from the simulation with the theoretical migration velocity under different voltages applied to the corona wire, three different inlet velocities of 0.6, 1.0 and 1.5 m/s and engine at high load condition. Figure 6.19a - Figure 6.19d compare the particle residence time of deposited particles for four applied voltages of -8 kV, -10 kV, -15 kV and -17 kV for inlet velocities of 0.6 m/s, 1.0 m/s and 1.5 m/s, respectively.

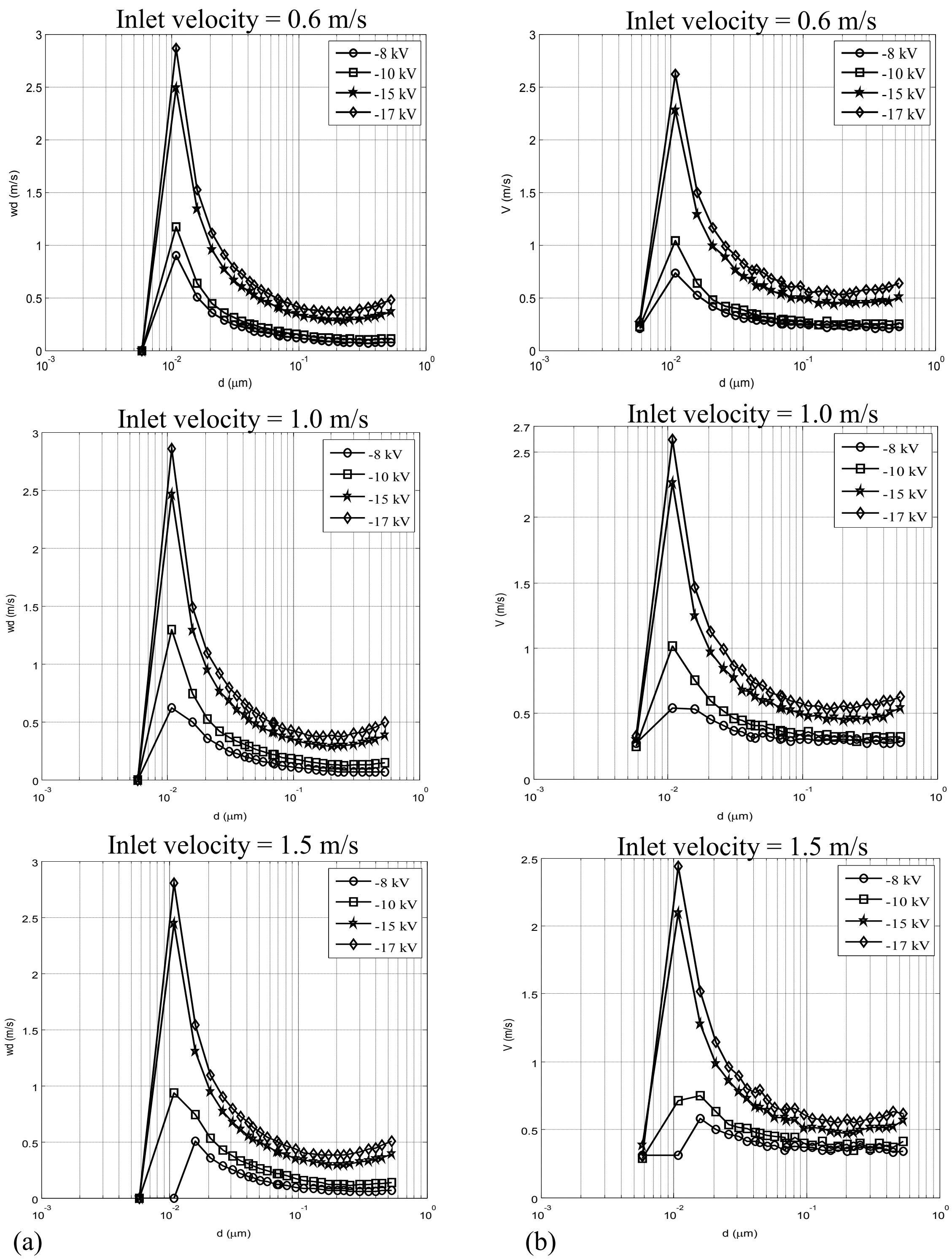

Figure 6.18. (a) Theoretical migration velocity calculated from Cochet particle charging model (b) particle migration velocity obtained from simulation for different applied voltages, channel length of 100 mm and inlet velocities of 0.6 m/s, 1 m/s and 1.5 m/s

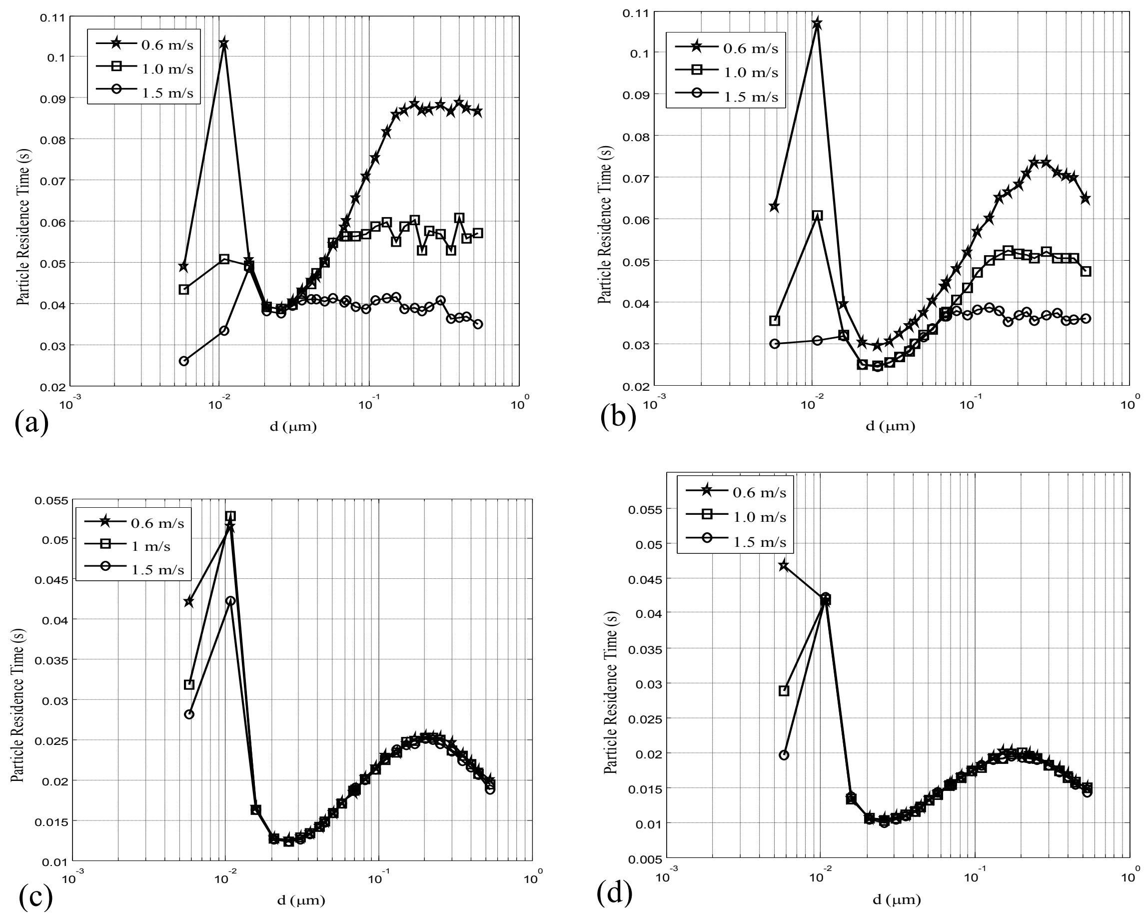

Figure 6.19. Particle residence time of deposited particles versus exhaust particle diameter for three inlet velocities, channel length of 100 mm and different applied voltages of (a) -8 kV, (b) -10 kV, (c) -15 kV and (d) -17 kV.

6.3.5 ESP performance on removal of submicron particles

6.3.5.1 Zero engine load and $T = 110^{o}$ C

Figure 6.20a - Figure 6.20d show the corresponding fractional efficiency of different particle sizes for the applied voltages of -8 kV, -10 kV, -15 kV and -17 kV and inlet velocities of 0.6, 1.0 and 1.5 m/s for engine at zero load condition. For excitation voltages of -8 kV and -10 kV the fractional efficiency has a minimum around 200-300 nm particle diameter and the fractional efficiency decreases by increasing the inlet velocity from 0.6 m/s to 1.5 m/s, as shown in Figure 6.20a - Figure 6.20b. This can be explained by looking at the particle migration velocities graphs (Figure 6.16b) and the relation between the particle migration velocity and fractional collection efficiency in Deutsch equation Eq. (3-35)). However, for -15 kV and -17 kV excitation voltages the fractional efficiency for all particle sizes are more than 95%, as shown in Figure 6.20c - Figure 6.20d.

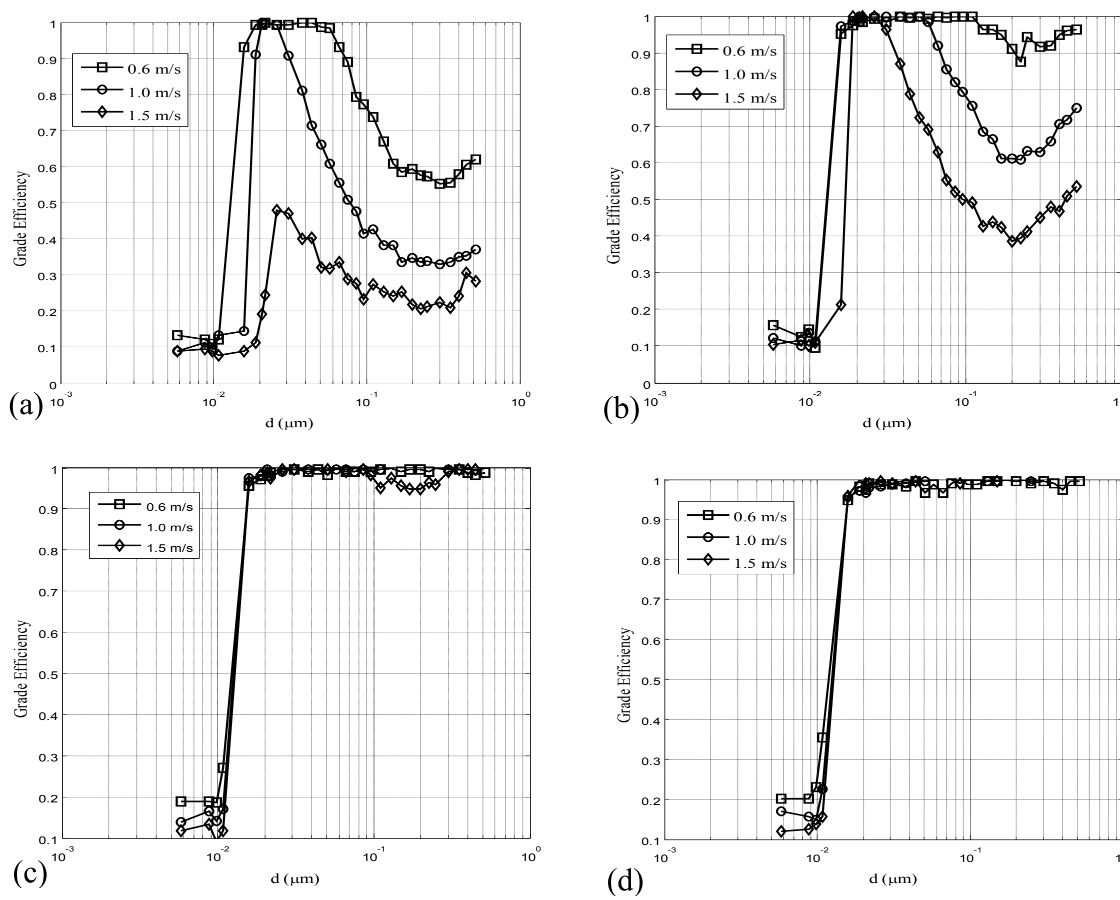

Figure 6.20. Fractional efficiency of ESP for three inlet velocities, channel length of 100 mm and different applied voltages of (a) -8 kV, (b) -10 kV, (c) -15 kV and (d) -17 kV.

The total mass collection efficiencies versus particle residence time for the four applied voltages and engine at zero load condition are shown in Figure 6.21. The total mass collection efficiency increases by increasing the gas residence time (lower inlet velocity) and increasing the excitation voltages. These results are summarized in Table 6.4.

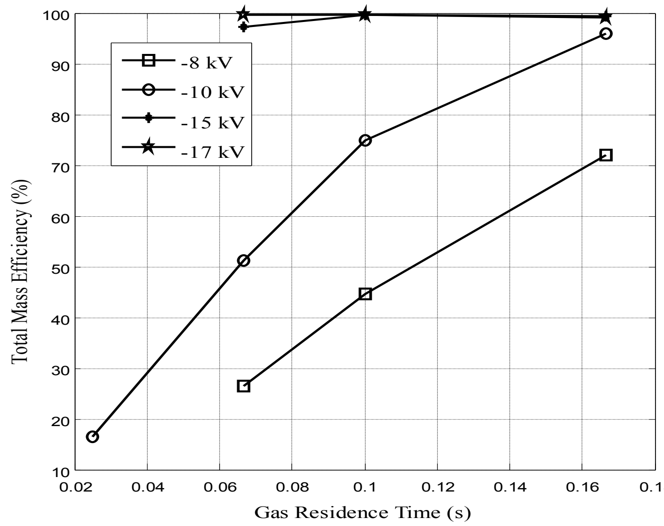

Figure 6.21. Total mass collection efficiency versus exhaust gas residence time for different applied voltages and 100 mm long ESP channel

Table 6.4. Total mass collection efficiency of ESP (L = 100 mm and T = 110^o C)

Applied voltage	**Total mass collection efficiency**			
	0.6 m/s	**1 m/s**	**1.5 m/s**	**4 m/s**
-8 kV	72.0%	44.5%	26.4%	-
-10 kV	96.0%	74.9%	51.2%	16.3%
-15 kV	99.2%	99.6%	97.3%	-
-17 kV	99.0%	99.6%	99.6%	-

6.3.5.2 High engine load and T= 210^{o} C

Figure 6.22a - Figure 6.22d show the corresponding fractional efficiency for the applied voltages of -8 kV, -10 kV, -15 kV and -17 kV and inlet velocities of 0.6, 1.0 and 1.5 m/s for engine at high load condition.

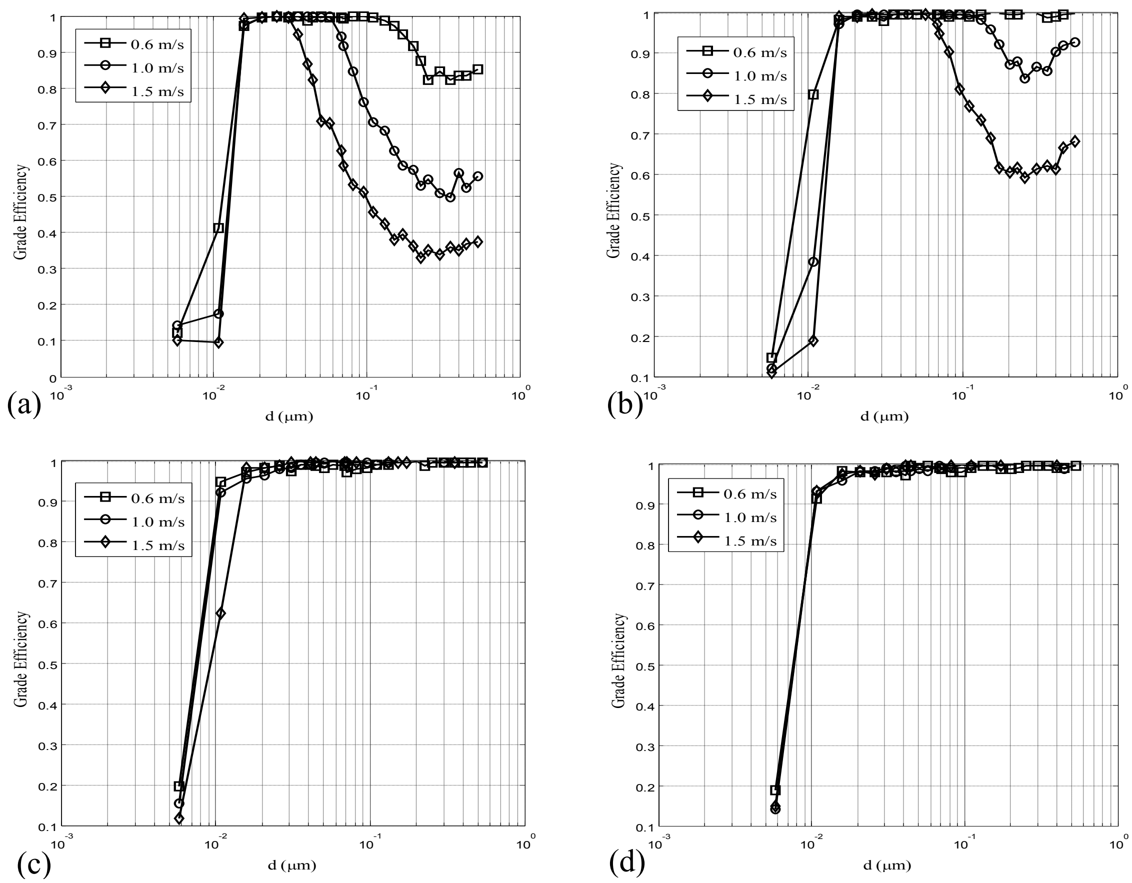

Figure 6.22. Fractional efficiency of ESP for three inlet velocities at inlet, channel length of 100 mm and different applied voltages of (a) -8 kV, (b) -10 kV, (c) -15 kV and (d) -17 kV.

The total mass collection efficiencies versus particle residence time for the four applied voltages and engine at high load condition are shown in Figure 6.23. These results are summarized in Table 6.5.

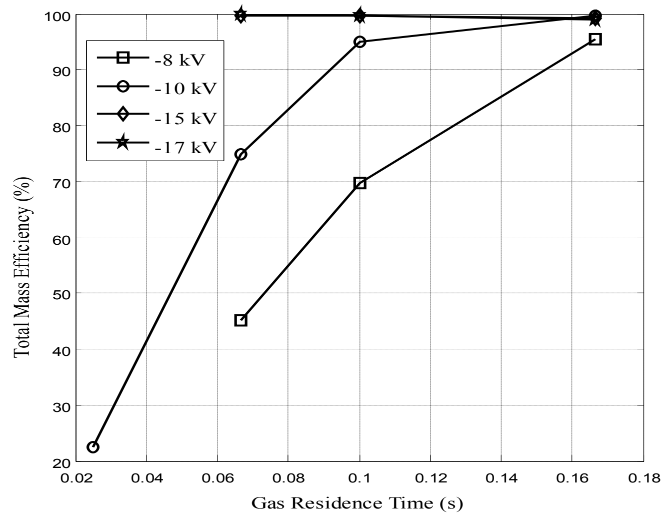

Figure 6.23. Total mass collection efficiency versus exhaust gas residence time for different applied voltages and 100 mm long ESP channel

Table 6.5. Total mass collection efficiency (L = 100 mm and T= 210^{o} C)

Applied voltage	Total mass collection efficiency			
	0.6 m/s	**1 m/s**	**1.5 m/s**	**4 m/s**
-8 kV	95.5%	69.6%	45.2%	-
-10 kV	99.6%	95.0%	74.8%	22.4%
-15 kV	99.1%	99.7%	99.7%	-
-17 kV	99.0%	99.7%	99.8%	-

6.3.5.3 Different channel lengths

Figure 6.24a and Figure 6.24b show the particle residence time and fractional efficiencies versus exhaust particle diameter for channel lengths in the range of 50-300 mm, with engine at low load condition and -10 kV voltage applied to the corona wire. It is clear that the residence time and fractional efficiency of particles increases by increasing the channel length and for 300 mm long channel almost all particles are trapped. Figure 6.25a and Figure 6.25b show the corresponding graphs for engine at high load condition. The total mass collection efficiency for different channel length and engine working at low load and high load conditions are summarized in Table 6.6.

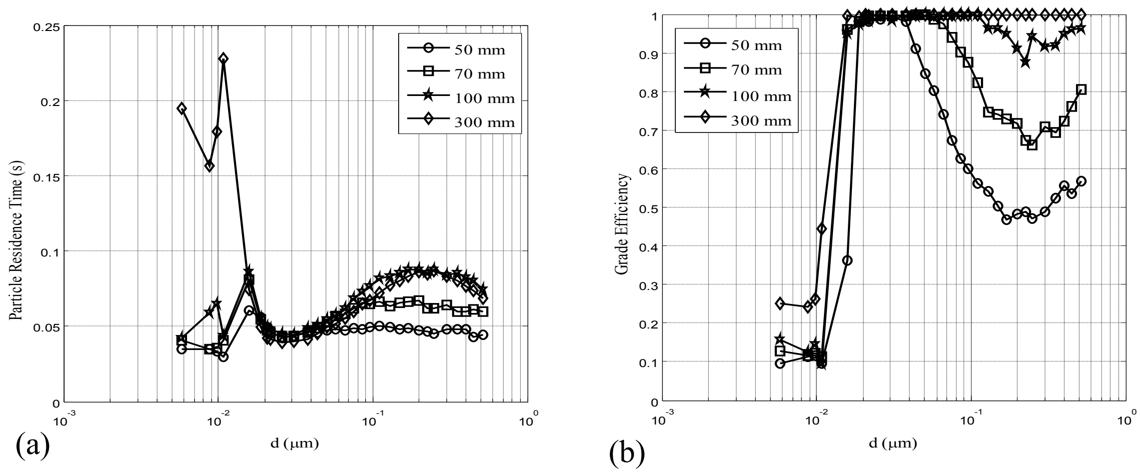

Figure 6.24. (a) Particle residence time and (b) fractional efficiency versus exhaust particle diameter for four different length of the ESP channel (applied voltage is -10 kV, inlet velocity is 0.6 m/s and engine is at low load condition)

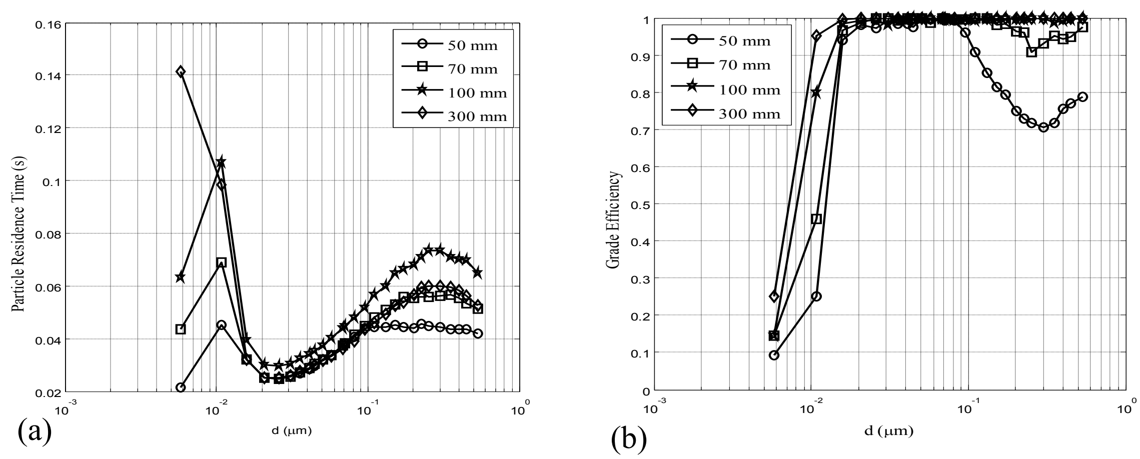

Figure 6.25. (a) Particle residence time and (b) fractional efficiency versus exhaust particle diameter for four different length of the ESP channel (applied voltage is -10 kV, inlet velocity is 0.6 m/s and engine is at high load condition)

Table 6.6. Total mass collection efficiency for different channel length (inlet velocity is 0.6 m/s, applied voltage is -10 kV)

Channel Length	Zero-Load	High-Load
50 mm	60.0%	86.0%
70 mm	81.2%	98.2%
100 mm	96.0%	99.6%
300 mm	99.8%	100%

6.4 Summary

A one-stage laboratory scale wire-cylinder ESP for collecting submicron diesel particulates was simulated. The analytical solution of Poisson and current continuity equations were coupled with the numerical solution of exhaust airflow Navier-Stokes equations using FLUENT software. It was shown that the EHD secondary flow is only generated in the channel when the corona wire is slightly off-center. Two particle size distributions were assumed considering zero and high engine load at the inlet. For different particle sizes, particle charge to mass ratio and deposition rate along the ESP channel were compared for different inlet velocities. It was shown that by increasing the particle residence time *i.e.* decreasing the inlet velocity, the particle charge to mass ratio increases and the particle removal efficiency increases. Particle migration velocities were obtained for different applied voltages and showed higher values comparing with the theoretical formula. Total mass collection efficiency for different channel lengths and the fractional efficiencies of all particle sizes were also obtained. It was shown that the collection efficiency graphs versus diesel particle diameter have a minimum around 200-300 nm for lower excitation voltages. However, for higher excitation voltage and lower gas velocities at inlet, the collection efficiency for all particle sizes is above 95%.

7. SUMMARY and RECOMMENDATIONS FOR FUTURE STUDY

7.1 Summary

In this thesis, a hybrid numerical technique was proposed for simulating the corona discharge phenomena, the generated EHD secondary flow, and particle charging and motion in a one-stage single-electrode ESP. The algorithm was based on three different numerical techniques: FEM, FCT and FVM. The first two were used to calculate the ionic charge density and electric potential distributions in the ESP channel by solving the Poisson and current continuity equations. Advantage was taken of both methods to achieve accurate simulation results in reasonable computing time. A non-uniform discretization of the domain was considered, where the elements in the vicinity of the discharge electrode were much finer than in the areas close to the collecting walls. Due to large memory allocation requirements the calculations were carried out using the SHARCNET supercomputing clusters. It is believed that, the proposed algorithm is the most advanced technique used so far for modeling the electrical characteristics inside an ESP. FVM was employed in the FLUENT commercial software for the airflow simulation. In many cases, the simulation results were compared with the existing experimental data to verify the reliability of the numerical model.

The 3-D characteristics of the EHD flow patterns were studied in single-stage rectangular ESPs, assuming a smooth corona wire with uniform discharge current along the wire and also spiked corona discharge electrodes with non-uniform distribution of discharge current along the electrodes. The EHD flow body force was inserted into FLUENT by using the UDFs, which link the corona discharge and the airflow algorithms together. The detailed distributions of all essential parameters for the electric and flow field were predicted. The effect of corona discharge electrode geometry and applied voltage on the corona discharge characteristics and EHD flow pattern was discussed. Particle charging and motion were investigated in different ESP models using DPM in FLUENT. The Lagrangian approach employing the DRW model for particle dispersion permitted examination of deposition in the ESP channel. The mutual interaction between three fields: electrostatic, airflow and particle dynamic was taken into account throughout the whole thesis. The collection efficiency of submicron and ultrafine particles was predicted with good accuracy for spiked electrode-plate and wire-cylinder ESP geometries. It was shown that, for the same voltage applied to the corona electrode, the spike-type discharge electrode with spikes on two sides improves collection efficiency of submicron particles in the range of 0.25-1.5 μm, when compared to the wire electrode and spiked electrode with spikes on only one side of the electrode. However, it should be recognized that the electric power consumption in an ESP with spikes on both sides in this case is almost double that in the ESP with spikes on one side of the discharge electrode only. Therefore, assuming identical corona discharge current, the best discharge electrode configuration would have spikes on one side only and directed in the upstream direction. The influence of electrode geometry, EHD flow and particle concentration on precipitation performance was studied in detail. It was found that the collection efficiency deceases by increasing the particle concentration at the inlet due to corona discharge suppression. A 20 times increase in the particle mass flow rate at inlet, caused the corona discharge current to decrease by 45%. Finally, the wire-cylinder ESP with uniform corona discharge along the wire was simulated to predict the collection efficiency of submicron conductive diesel exhaust particulates. Particle migration velocities for different inlet velocities and applied voltages were evaluated and the fractional efficiencies were obtained for all particle sizes. It was found that by increasing the applied voltage, length of the ESP channel and gas residence time the collection efficiency increase up to 95% for all particle sizes. The proposed mathematical model for simulating the whole precipitation process in this thesis was also applicable for modeling practical pilot scale wet ESPs with complex corona discharge electrodes in industrial application.

7.2 Recommendations for future study

It is believed that the research reported in this thesis answers some fundamental questions about EHD flow and different parameters effect on particle collection efficiency in ESPs with complicated discharge electrode geometries. However, there are a number of issues which deserves further investigations:

1. **Modify the current computer program for numerical calculations of the electrical characteristics inside the ESP, to be applicable for efficient parallel processing.** Some pure numerical simulations of precipitation performance are suggested in the

literature using Direct Numerical Simulation (DNS) [17,118-121], Monte-Carlo simulation [44], or SIMPLE algorithm [9-11]. However, these numerical methods are usually applicable at fairly low Reynolds numbers, and sufficient spatial and temporal resolution is essential to obtain accurate results, which demands supercomputers with massively parallel processing. The numerical approach carried out in this study also has some numerical restrictions on the number of nodes and elements obtained from discretization due to large matrices created in the 3-D numerical technique used for calculating the electrical parameters. This computer program needs to be modified to be applicable for parallel processing in SHARCNET supercomputing clusters. In this study, the flow field is computed using the k-ε model for turbulence in the commercial FLUENT 6.2 software considering the EHD flow effects. Despite some intrinsic deficiency of the models adopted in FLUENT, as mentioned by Soldati in [118], it is perfectly applicable to an industrial problem with complicated discharge electrode configuration, where it would be hard to perform DNS simulation. Besides, FLUENT software has the capability to operate in parallel mode for large geometries with some specific rules for implementing UDFs in this mode.

2. **Estimate the *I-V* characteristics for more complicated corona electrode geometries.** To estimate the ionic charge density distribution on the corona electrode surface for smooth corona wire discharge electrode with uniform distribution, the Kaptzov hypothesis is applicable. However, for more complicated electrode geometries it is necessary to know the *I-V* curve. In this thesis, the corona discharge current obtained from experimental data was used to estimate the non uniform ionic charge density on the spiked electrode surface. The analytical solution of Poisson and current continuity equations are only available for wire-cylinder ESP configuration, discussed in Chapter 6. Therefore, for more complicated discharge electrode geometries a new methodology should be utilized to evaluate the *I-V* characteristic applicable for single-stage ESPs.

3. **Investigate the effect of electrical resistivity of particles on the collection efficiency.** Particles with a low electrical resistivity have lower collection efficiency due to re-entrainment after deposition. In industrial applications wESPs are recommended to overcome this problem. However, calculating the effects of back corona phenomenon

on ESP performance in the case of particles with high electrical resistivity needs more investigation. Back-corona discharge is triggered by the electrical breakdown of the dust layer that occurs due to the high dust resistivity and high ionic current across the dust layer. Back-corona discharge creates positive ions that tend to neutralize incoming negatively polarized particles, and reduces the electric field near the collecting electrode, thus dramatically impairing dust collection. The prediction of collection efficiency assuming back-corona discharge is usually based on semi-empirical approaches. In order to implement the back-corona discharge further modification in the ESP model should address the bipolar composition of discharge current as well as the bipolar charging mechanism of dust particles.

4. **Optimize the ESP design or use hybrid devices to improve submicron and ultrafine particle removal.** Although, the overall mass based collection efficiency of ESPs are over 99%, the collection efficiency of submicron particles can be in the range of 60-80% or even lower. In fact, the collection of particles smaller than 30 nm is below 50% due to a majority of particles being uncharged. For increasing the submicron and ultrafine particles collection efficiency to meet new emission regulations some methods can be used such as: surface charge enhancement by new charging methods or improved corona charging with pre-chargers, mechanical or chemical agglomeration of particles and combinations of other technology (hybrid devices) such as a thermal precipitator, electret filters, wet-electrostatic precipitators and vortex, cyclone or scrubbers, and new ESP designs including new geometries and optimization of existing ones.

5. **Optimize the ESP design for practical cases such as diesel exhaust particulates removal with respect to capital and operating cost and also installation and maintenance expenses.** The wire-cylinder ESP configuration studied in Chapter 6 could be readily used for an effective control of diesel exhaust particulates from a stationary diesel emission source at the optimum gas residence time. The ESP could also be scaled up for treating higher volumetric exhaust flow rate emitted from larger diesel engines. However, from a practical point of view to really apply this type of technology to such stationary diesel equipment or to diesel vehicles, several practical aspects should be taken into account in order to optimize the performance of the ESP

with respect to its capital and operating cost, and also ease of maintenance and handling. It was shown that the ESP collection efficiency improves significantly at higher corona discharge power. However, a high applied voltage requires an increase of the ESP diameter in order to prevent the initiation of an arc between the electrodes. Therefore, the ESP becomes larger and takes up more space but shorter in length assuming that the specific collection area is fixed, hence resulting in a higher installation cost. The ESP operating cost also goes up due to higher corona power utilization. A large-diameter ESP may not be practical for a diesel vehicle application because of the size restriction, while it may be more appropriate for the stationary diesel emission sources. It was also shown that the ESP performance could be enhanced by increasing the length of the ESP without changing its diameter. Longer ESP results in higher collection surface area proportional to a longer gas residence time being available inside the ESP for higher DPM emission removal. For bigger diesel engines, higher exhaust volumetric flow rate is generated, thereby requiring a longer ESP, thus, the total length of the ESP which includes other design margins, such as water distribution system in wESP, insulator, etc, might be too long which may not be suitable for mobile diesel engines.

REFERENCES

[1] J. S. Chang, A. J. Kelly and J. M. Crowley, *Handbook of Electrostatic processes*, Marcel Dekker Inc., NewYork, 1995.

[2] K. R. Parker, *Applied Electrostatic Precipitation,* Chapman & Hall, West Midland, UK, 1997.

[3] J.L. Davis and J.F. Hoburg, "Wire-duct precipitator field and charge computation using finite element and characteristics method", *J. Electrostat.*, vol. 14, pp. 187-199, 1983.

[4] A.A. Elmoursi and G.S. Peter Castle, "Modeling of corona characteristics in a wire-duct precipitator using the charge simulation technique", *IEEE Trans. Ind. Appl.*, vol. IA–23, no. 1, pp. 95–102, 1987.

[5] J. H. Davidson, P. J. McKinney and P. Linnebur, "Three-dimensional (3-D) model of electric field and space charge in the barbed plate-to-plate precipitator", *IEEE Trans. Ind. Appl.*, vol. 32, no. 4, pp. 858-866, 1996.

[6] Z.M. Al-Hamouz, "A combined algorithm based on finite elements and a modified method of characteristics for the analysis of the corona in wire-duct electrostatic precipitators", *IEEE Trans. Ind. Appl.*, vol. 38, no 1, pp. 43-49, 2002.

[7] Y.N. Chun, J.-S. Chang, A.A. Berezin and J. Mizeraczyk, "Numerical modeling of near corona wire electrohydrodynamics flow in a wire-plate electrostatic precipitator", *IEEE Trans. Dielectr. Electr. Insul.*, vol. 14, no. 1, pp. 119-124, 2007.

[8] L. Zhao and K. Adamiak, "Numerical simulation of the electrohydrodynamic flow in a single wire-plate electrostatic precipitator", *IEEE Trans. Ind. Appl.*, vol. 44, no. 3, pp. 683-691, 2008.

[9] T. Yamamoto, M. Okuda and M. Okubo, "Three-dimensional ionic wind and electrohydrodynamics of tuft/point corona electrostatic precipitator", *IEEE Trans. Ind. Appl.*, vol. 39, no. 6, pp. 1602-1607, 2003.

[10] T. Yamamoto, Y. Morita, H. Fujishima and M. Okubo, "Three-dimensional EHD simulation for point corona electrostatic precipitator based on laminar and turbulent models", *J. Electrostat.*, vol. 64, no. 7-9, pp. 628-633, 2006.

[11] T. Yamamoto, "Effects of turbulence and electrohydrodynamics on the performance of electrostatic precipitator", *J. Electrostat.*, vol. 2, pp. 11-22, 1989.

[12] W. J. Liang and T.H. Lean, "The characteristics of ionic wind and its effect on electrostatic precipitators", *J. Aerosol Sci.,* vol. 20, pp. 330-344, 1994.

[13] D. Brocilo, J. Podlinski, J. Dekowski, J. Mizeraczyk, K. Urashima and J.S. Chang, "Electrohydrodynamic flow patterns in a wide spacing spike-plate electrostatic precipitators under negative coronas", *Proc. of the 5th Int. Conf. on Appl. Electrostat.*, Shanghai, China, pp. 100-103, Nov. 2004.

[14] G. A. Kallio and D. E. Stock, "Interaction of electrostatic and fluid dynamic fields in wire-plate electrostatic precipitator", *J. Fluid Mech.*, vol. 240, no. 7, pp. 133-166, 1992.

[15] H.–J. Schmid, S. Stolz and H. Buggisch, "On the modeling of the electro-hydrodynamic flow field in electrostatic precipitators", *J. Flow Turbul. Combust.*, vol. 68, pp. 63-89, 2002.

[16] U. Kogelschatz, W. Egli and E.A. Gerteisen, "Advanced computational tools for electrostatic precipitators", *ABB Rev. 4*, pp. 33-42, 1999.

[17] A. Soldati, "On the effects of electro-hydrodynamic flows and turbulence on aerosol transport and collection in wire-plate electrostatic precipitators", *J. Aerosol Sci.*, vol. 31, pp. 293-305, 2000.

[18] H. Fujishima, Y. Ueda, K. Tomimatsu and T. Yamamoto, "Electrohydrodynamics of spiked electrode electrostatic precipitators", *J. Electrostat.*, vol. 62, pp. 291-308, 2004.

[19] G. Skodras, S.P. Kaldis, D. Sofialidis, O. Faltsi, P. Grammelis and G.P. Sakellaropoulos, "Particle removal via electrostatic precipitators-CFD simulation", *Fuel Process. Technol.*, vol. 87, pp. 623-631, 2006.

[20] J. Podlinski, A. Niewulis, J. Mizeraczyk and P. Atten, "ESP performance for various dust densities", *J. Electrostat.*, vol. 66, pp. 246-253, 2008.

[21] K. Adamiak and P. Atten, "Numerical simulation of the 2-D gas flow modified by the action of charged fine particles in a single-wire ESP", *IEEE Trans. on Dielectr. Electr. Insul.*, vol. 16, pp. 608-614, 2009.

[22] M. Jedrusik, J. B. Gajewski and A.J. Swierczok, "Effect of the particle diameter and corona electrode geometry on the particle migration velocity in electrostatic precipitator", *J. Electrostat*., vol. 51-52, pp. 245-251, 2001.

[23] C. Riehle, "Mass flux and effective migration velocity in electrostatic precipitators", *Powder Technol.*, vol. 86, no. 1, pp. 95-102, 1996.

[24] D. Brocilo, J. Podlinski, J.S. Chang, J. Mizeraczyk and R.D. Findlay, "Electrode geometry effects on the collection efficiency of submicron and ultra fine dust particles in spike-plate electrostatic precipitators", *J. Phys.: Conf. Ser.*, vol. 142, no. 1, pp. 1-6, 2008.

[25] J. Podlinski, A. Niewulis and J. Mizeraczyk, "Electrohydrodynamic flow and particle collection efficiency of a spike-plate type electrostatic precipitator", *J. Electrostat.*, vol. 67, pp. 99-104, 2009.

[26] J. Podlinski, A. Niewulis, V. Shapova and J. Mizeraczyk, "Electrohydrodynamic flow and particle collection efficiency in a one-sided spike-plate type electrostatic precipitator", *7th Conf. of the French Society of Electrostat. (SFE2010)*, Montpellier, France, Aug-Sep. 2010.

[27] P.L. Levin and J.F. Hoburg, "Donor cell-finite element descriptions of wire-duct precipitator fields, charges, and efficiencies", *IEEE Trans. Ind. Appl.*, vol. 26, pp. 662-670, 1990.

[28] J. Anagnostopoulos and G. Bergeles, "Corona discharge simulation in wire-duct electrostatic precipitator", *J. Electrostat.*, vol. 54, pp. 129–147, 2002.

[29] J. H. Davidson, P. J. McKinney and P. Linnebur, "Three-dimensional (3-D) model of electric field and space charge in the barbed plate-to-plate precipitator", *IEEE Trans. Ind. Appl*., vol. 32, no. 4, pp. 858-866, 1996.

[30] H. Fujishima, Y. Morita, M. Okubo and T. Yamamoto, "Numerical simulation of three-dimensional electro-hydrodynamics of spiked-electrode electrostatic precipitator", *IEEE Trans. on Diel. and Electr. Insul.*, vol. 13, no. 1, pp. 160-167, 2006.

[31] L. M. Dumitran, P. Atten and D. Blanchard, "Numerical simulation of fine particles charging and collection in an electrostatic precipitator with regular barbed electrodes", *Inst. Phys. Conf. Ser.*, no. 178, pp. 199-205, 2003.

[32] J.H. Davidson, "EHD flow visualization in the wire-plate and barbed plate electrostatic precipitator", *IEEE Trans. Ind. Appl.*, vol. 27, no. 1, pp. 154-160, 1991.

[33] T. Ullum, P. S. Larsen, O. Ozcan, "Three-dimensional flow and turbulence structure in electrostatic precipitator by stereo PIV", *Exp. Fluids*, vol. 36, pp. 91-99, 2004.

[34] T. Yamamoto and H. R. Velkoff, "Electrohydrodynamics in an electrostatic precipitator", *J. Fluid Mech.*, vol. 108, pp. 1-18, 1981.

[35] G. A. Kallio, D. E. Stock, "Flow visualization inside a wire-plate electrostatic precipitator", *IEEE Trans Ind. Appl.*, vol. 26, no. 3, pp. 503-514, 1990.

[36] J. H. Davidson and P. J. McKinney, "EHD flow visualization in the wire-plate and barbed plate electrostatic precipitator", *IEEE Trans. Ind. Appl.*, vol. 27, no. 1, pp. 154-160, 1991.

[37] T. Ullum and P.S. Larsen, "Swirling flow structures in electrostatic precipitator", *J. Flow Turbul. Combust.*, vol. 73, no. 3-4, pp. 259-275, 2004.

[38] P. S. Larsen and E. M. Christensen, "Secondary flow and turbulence in electrostatic precipitators", *3rd Int. Symp. on Appl. of Laser Anemometry to Fluid Mech.*, Lisbon, pp. 361-374, 1988.

[39] J. H. Davidson and P. J. McKinney, "Turbulent mixing in a barbed plate-to-plate electrostatic precipitator", *Atmos. Environ.*, vol. 23, no. 10, pp. 2093-2107, 1989.

[40] J. Podliński, R. Barbucha and J. Mizeraczyk, "EHD flow patterns in narrow and wide ESPs measured by 3D PIV method," *Proc. 5eme Conf. Societe Francaise Electrostatique*, Grenoble, pp. 53-56, 2006.

[41] A. Niewulis, J. Podlinski and J. Mizeraczyk, "Electrohydrodynamic flow patterns in a narrow electrostatic precipitator with longitudinal or transverse wire electrode," *J. Electrostat.*, vol. 67, pp. 123-127, 2009.

[42] J. Podlinski, M. Kocik R. Barbucha, A. Niewulis, J. Mizeraczyk and A. Mizuno, "3D PIV measurements of the EHD flow patterns in a narrow electrostatic precipitator with wire-plate or wire-flocking electrodes," *Czechoslovak J. of Phys.*, vol. 56, suppl. B, pp. 1009-1016, 2006.

[43] A. Mizuno, "Electrostatic precipitation", *IEEE Trans. Dielectr. Electr. Insul.*, vol. 7, pp. 615-624, 2000.

[44] H. Lei, L.-Z. Wang and Z.-N. Wu, "EHD turbulent flow and Monte-Carlo simulation for particle charging and tracing in a wire-plate electrostatic precipitator", *J. Electrostat.*, vol. 66, pp. 130-141, 2008.

[45] Z. Long and Q. Yao, "Evaluation of various particle charging models for simulating particle dynamics in electrostatic precipitators", *J. Aerosol. Sci.*, vol. 41, pp. 702-718, 2010.

[46] P. A. Lawless, "Particle charging bounds, symmetry relations and an analytic charging rate model for the continuum regime", *J. Aerosol Sci.*, vol. 27, no. 2, pp. 191-215, 1996.

[47] A.A. Varonos, J.S. Anagnostopoulos and G.C. Bergeles, "Prediction of the cleaning efficiency of an electrostatic precipitator", *J. Electrostat.*, vol. 55, no. 111, 2002.

[48] K.S.P. Nikas, A.A. Varonos and G.C. Bergeles, "Numerical simulation of the flow and the collection mechanisms inside a laboratory scale electrostatic precipitator", *J. Electrostat.*, vol. 63, no. 423, 2005.

[49] H.J. Schmid and L. Vogel, "On the modeling of the particle dynamics in electrohydrodynamics flow fields: I. Comparison of Eulerian and Lagrangian modeling approach", *Powder Technol.*, vol. 135 & 136, pp. 118-135, 2003.

[50] H.J. Schmid, "On the modeling of the particle dynamics in electrohydrodynamics flow fields: II. Influences of inhomogeneities on electrostatic precipitation", *Powder Technol.*, vol. 135 & 136, pp. 136-149, 2003.

[51] J.H. Goo and J.W. Lee, "Stochastic simulation of particle charging and collection characteristics for a wire-plate electrostatic precipitator of short length", *J. Aerosol. Sci.*, vol. 28, no. 5, pp. 875-893, 1997.

[52] C. Lu and H. Huang, "A sectional model to predict performance of a plate-wire electrostatic precipitator for collecting polydisperse particles", *J. Aerosol.Sci.*, vol. 29, no. 3, pp. 295-308, 1998.

[53] S.H. Kim and K.W. Lee, "Experimental study of electrostatic precipitator performance and comparison with existing theoretical prediction models", *J. Electrostat*., vol. 48, pp. 3-25, 1999.

[54] S.H. Kim, H.S. Park and K.W. Lee, "Theoretical model of electrostatic precipitator performance for collecting polydisperse particles", *J. Electrostat*., vol. 50, pp.177-190, 2001.

[55] S.W. Nóbregal, M.C.R. Falaguasta and J.R. Coury, "A study of a wire-plate electrostatic precipitator operating in the removal of polydispersed particles", *Brazilian J. Chem. Eng*., vol. 21, no. 2, pp. 275-284, 2004.

[56] T. Ivancsy and J.M. Suda, "Behavior of polydisperse dust in electrostatic precipitators", *J. Electrostat*., vol. 63, pp. 923-927, 2005.

[57] B.S. Choi and C.A.J. Fletcher, "Turbulent particle dispersion in an electrostatic precipitator", *Appl. Math. Modell*., vol. 22, pp. 1009-1021, 1998.

[58] Y. Koizumi, M. Kawamura, F. Tochikubo and T. Watanabe, "Estimation of agglomeration coefficient of bipolar-charged aerosol particles", *J. Electrostat*., vol. 48, pp. 93-101, 2000.

[59] J. H. Byeon, J. Hwang, J. H. Park, K.-Y. Yoon, B.J. Ko, S.H. Kang and J. H. Ji, "Collection of submicron particles by an electrostatic precipitator using a dielectric barrier discharge", *J. Aerosol. Sci.*, vol. 37, pp. 1618-1628, 2006.

[60] B. Dramane, N. Zouzou, E. Moreau and G. Touchard, "Electrostatic precipitation in wire-to-cylinder configuration: Effect of the high voltage power supply waveform", *J. Electrostat*., vol. 67, pp. 117-122, 2009.

[61] N. Zouzou, B. Dramane, E. Moreau and G. Touchard, "Correlation between the EHD flow and the collection efficiency of an ESP", *Proc. of Joint Conf. on Electrostat.*, Boston, Jun 2009.

[62] J. Zhu, X. Zhang, W. Chen, Y. Shi and K. Yan, "Electrostatic precipitation of fine particles with a bipolar pre-charger", *J. Electrostat*., vol. 68, pp. 174-178, 2010.

[63] J.-H. Kim, H.-S. Lee, H.-H. Kim and A. Ogata, "Electrospray with electrostatic precipitator enhances fine particles", *J. Electrostat*. , vol. 68, pp. 305-310, 2010.

[64] W.-Y. Lin, L.-C. Wang, Y.-F. Wang, H.-W. Lid and G.-P. Chang-Chien, "Removal characteristics of PCDD/Fs by the dual bag filter system of a fly ash treatment plant", *J. Hazard. Mater.*, vol. 153, no. 3, pp. 1015-1022, 2008.

[65] G. Koglbauer and W. Gigacher, "Removing dust from process gases with optimized cyclone systems", *ZKG International*, vol. 63, no. 10, pp. 46-52, 2010.

[66] S. Zarei, E. Jamshidi and A. Afshar Ebrahimi, "PVC dust removal from the air by a new dynamical scrubber", *Chem. Eng. Process*, vol. 49, no. 11, pp. 1193-1198, 2010.

[67] A. Niewulis, J. Podlinski, M. Kocik, R. Barbucha, J. Mizeraczyk and A. Mizuno, "EHD flow measured by 3D PIV in a narrow electrostatic precipitator with longitudinal-to-flow wire electrode and smooth or flocking grounded plane electrode", *J. Electrostat.*, vol. 65, pp. 728–734, 2007.

[68] A. Niewulis, J. Podlinski, V. Shapovall and J. Mizeraczyk, "Collection efficiency in narrow electrostatic precipitators with a longitudinal or transverse wire electrode", *7th Conf. of the French Society of Electrostat. (SFE2010)*, Montpellier, France, Aug-Sep. 2010.

[69] J. M. Desantes, X. Margot, A. Gil and E. Fuentes, "Computational study on the deposition of ultrafine particles from diesel exhaust aerosol", *J. Aerosol Sci.*, vol. 37, pp. 1750–1769, 2006.

[70] P. Saiyasitpanich, T. C. Keener, M. Lu, S.-J. Khang and D.E. Evans, "Collection of ultrafine diesel particulate matter (DPM) in cylindrical single-stage wet electrostatic precipitators", *Environ. Sci. Technol.*, vol. 40, pp. 7890-7895, 2006.

[71] P. Saiyasitpanich, T. C. Keener, S.-J. Khang and M. Lu, "Removal of diesel particulate matter (DPM) in a tubular wet electrostatic precipitator", *J. Electrostat.*, vol. 65, pp. 618-624, 2007.

[72] C. Wadenpohl and F. Loffler, "Electrostatic agglomeration and centrifugal separation of diesel soot particles", *Chem. Eng. Process.*, vol. 33, pp. 371–377, 1994.

[73] R. Boichot, A. Bernis and E. Gonze, "Treatment of diesel particles using an electrostatic agglomerator under negative DC corona: a modeling and experimental study", *IEEE Trans. Plasma Sci.*, vol. 35, no. 3, pp. 675–692, 2007.

[74] R. Boichot, A. Bernis and E. Gonze, “Agglomeration of diesel particles by an electrostatic agglomerator under positive DC voltage: Experimental study”, *J. Electrostat*., vol. 66, pp. 235–245, 2008.

[75] B.-J Sung, A. Aly, S.-H. Lee, K. Takashima, S. Kastura and A. Mizuno, “Fine-particle collection using an electrostatic precipitator equipped with an electrostatic flocking filter as the collection electrode”, *Plasma Process Polym.*, vol 3, pp. 661-667, 2006.

[76] S. Sato, M. Kimura, T. Aki, I. Koyamoto, K. Takashima, S. Katsura and A. Mizuno, “A removal system of diesel particulate using electrostatic precipitator with discharge plasma,” *Proc. IEEE 40th IAS Annual Meeting*, Kowloon, Hong Kong, vol. 3, pp. 2203-2206, Oct. 2005.

[77] H. Hayashi, Y. Takasaki, K. Kawahara, T. Takenaka, K. Takashima and A. Mizuno, “Electrostatic charging and precipitation of diesel soot”, *IEEE Trans. Ind. Appl*., vol. 47, no. 1, pp. 331-335, 2011.

[78] Y. Zhuang, Y. J. Kim, T. G. Lee and P. Biswas, “Experimental and theoretical studies of ultra-fine particle behavior in electrostatic precipitators”, *J. Electrostat*., vol. 48, pp. 245-260, 2000.

[79] A. Marquard, M. Kasper, J. Meyer and G. Kasper, “Nanoparticle charging efficiencies and related charging conditions in a wire-tube ESP at DC energization”, *J. Electrostat.*, vol. 63, pp. 693-698, 2005.

[80] A. Tilmatine, R. Gouri, F. Miloua, N. Kadous, K. Medles and L. Dascalescu, “Optimisation of the intermittent operation of a wire-cylinder electrostatic precipitator”, *J. Phys.: Conf. Ser.*, vol. 142, pp. 12-19, 2008.

[81] T. Kuroki, M. Ishidate, M. Okubo and T. Yamamoto,” Charge-to-mass ratio and dendrite structure of diesel particulate matter charged by corona discharge”, *CARBON*, vol. 48, pp. 184 –190, 2010.

[82] Z. Nimg, C. S. Cheung and S. X. Liu, “Experimental investigation of the effect of exhaust gas cooling on diesel particulates”, *J. Aerosol. Sci*., vol. 35, pp. 333-345, 2004.

[83] W. Deutsch, “Bewegung und ladung der elektrizitatstrager im zylinderkondensator”, *Annal. Phys.*, vol. 68, pp. 335-344, 1922.

[84] R. Baghaei Lakeh and M. Molki, “Patterns of airflow in circular tubes caused by a corona jet with concentric and eccentric wire electrodes”, *J. Fluids Eng.*, vol. 132, 2010, DOI: 10.1115/1.4002008.

[85] C. J. Chen, Shenq-Yuh Jaw, *Fundamentals of turbulence modeling*, Taylor & Francis, 1998.

[86] D. Pnueli and C. Gutfinger, *Fluid Mechanics*, Cambridge University press, 1992.

[87] *Fluent 6.2 User’s Guide*, Fluent Inc.

[88] F.M. White, *Fluid Mechanics*, 4rd Ed., McGraw-Hill, 1999.

[89] S.A. Morsi and A.J. Alexander, “An investigation of particle trajectories in two-phase flow systems”, *J. Fluid Mech.*, vol. 55, no. 2, pp. 193-208, 1972.

[90] A. Haider and O. Levenspiel, “Drag coefficient and terminal velocity of spherical and non-spherical particles”, *Powder Technol.,* vol. 58, pp. 63-70, 1989.

[91] H. Ounis, G. Ahmadi and J. B. McLaughlin, “Brownian diffusion of submicrometer particles in the viscous sublayer”, *J. Colloid Interface Sci.,* vol. 143, no. 1, pp. 266-277, 1991.

[92] S. G. Jennings, ”The mean free path in air”, *J. Aerosol Sci*., vol. 19, no. 2, pp. 159-166, 1988.

[93] J.O. Hirschfelder, C.F. Curtiss and R.B. Bird, *Molecular Theory of Gases and Liquids*, John Wiley & Sons, Inc., New York, 1954.

[94] H. Ounis and G. Ahmadi, “A comparison of Brownian and turbulent diffusion”, *J. Aerosol Sci.,* vol. 13, pp. 47-53, 1990.

[95] R. L. Cochet, “Charge des fines particles (Submicroniques) etudes theoretiques-controles recents spectre de particules”, *Coll. Int. la Physique des Forces Electrostatiques et Leurs Application*, *Cent. Nat. Rech. Sci.,* no. 102, pp. 331-338, 1961.

[96] W. Deutsch, “Bewegung und ladung der elektrizitatstrager im zylinderkondensator” *Annal. Phys.*, vol. 68, pp. 335-344, 1922.

[97] D. C. Cooper and F. C. Alley, *Air Pollution Control: A Design Approach*, 3rd Ed., Waveland Press, Inc, Illinois, 2002.

[98] L. M. Dumitran, P. Atten and D. Blanchard, "Drift velocity of fine particles estimated from fractional efficiency measurements in a laboratory-scale electrostatic precipitator", *8th Intl. Conf. Electrostatic precipitation*, Birmingham, Alabama, May 2001.

[99] K. R. Parker, *Electrostatic precipitation*, Chapman & Hall, 1997, pp. 25-86.

[100] S. Oglesby and G. B. Nichols, *Electrostatic precipitation, Pollution Engineering and Technology*, vol. 8, Marcel Dekker Inc., New York, 1978, pp. 31-64.

[101] H.J. White, *Industrial electrostatic precipitation*, Addison-Wesley, Pergamon Press, 1963, pp. 74-125.

[102] W. Peukert and C. Wadenpohl, "Industrial separation of fine particles with difficult dust properties", *Powder Technol.*, vol. 118, pp. 136-148, 2001.

[103] C. Riehle, *PhD thesis*, University of Karlsruhe, 1922.

[104] H.-J. Schmid, *PhD thesis*, University of Karlsruhe, 1998.

[105] K. Adamiak and P. Atten, "Simulation of corona discharge in point-plane configuration", *J. Electrostat.*, vol. 61, pp. 85-98, 2004.

[106] K. Adamiak, J. Zhang and L. Zhao, "Finite element versus hubrid BEM-FEM techniques for the electric corona simulation", *The Electrotechnical Review*, no. 10, pp. 753-756, 2003

[107] A.M. Meroth, T. Gerber, C. D. Munz, P.L. Levin and A.J. Schwab, "Numerical solution of nonstationary charge coupled problems", *J. Electrostat.*, vol. 45, pp. 177-198, 1999.

[108] W.-G. Min, H.-S. Kim, S.-H. Lee and S.-Y. Hahn, "An investigation of FEM-FCT method for streamer corona simulation", *IEEE Trans. Magn.*, vol. 36, no. 4, pp. 1280-1284, 2000.

[109] G.E. Georghiou, R. Morrow and A.C. Metaxas, "A two- dimensional, finite-element, flux-corrected transport algorithm for the solution of gas discharge problems", *J. Phys. D: Appl. Phys.*, vol. 33, pp. 2453-2466, 2000.

[110] D. Kuzmin, M. Moller and S. Turek, “High-resolution FEM–FCT schemes for multidimensional conservation laws”, *J. Comput. Methods Appl. Mech. Eng.*, vol. 193, pp. 4915–4946, 2004.

[111] S. V. Patankar, *Numerical Heat Transfer and Fluid Flow,* Taylor & Francis, USA, 1980.

[112] G. Herdan, *Small particle statics*, 2nd Ed., Academic Press, New York, 1980.

[113] N. Farnoosh, K. Adamiak and G.S.P. Castle, ”3D numerical analysis of EHD turbulent flow and mono-disperse charged particle transport and collection in a wire-plate ESP”, *J. Electrostat.*, vol. 68, no. 6, pp. 513-522, 2010.

[114] N. Farnoosh, K. Adamiak and G.S.P. Castle, “3-D numerical simulation of particle concentration effect on a single-wire ESP performance for collecting poly-dispersed particles”, *IEEE Trans. Dielectr. Electr. Insul.*, vol. 18, no. 1, pp. 211-220, 2011.

[115] N. Farnoosh, K. Adamiak and G.S.P. Castle, “Three-dimensional analysis of electrohydrodynamic flow in a spiked electrode-plate electrostatic precipitator”, *J. Electrostat.*, vol. 69, pp. 419-428, 2011.

[116] N. Farnoosh, K. Adamiak and G.S.P. Castle,” Numerical calculations of submicron particle removal in a spike-plate electrostatic precipitator,” *IEEE Trans. Dielectr. Electr. Insul*, vol. 18, no. 5, pp. 1439-1452, 2011.

[117] W. Janischewskyj and G. Gela, “Finite element solution for electric fields of coronating dc transmission lines”, *IEEE Trans. Power Appar. Syst.*, vol. 98, pp. 1000-1012, 1979.

[118] A. Soldati, and S. Banerjee “Turbulence modification by large-scale organized electrohydrodynamic flows”, *Phys. Fluids*, vol. 10, no. 7, pp. 1742-1756, 1998.

[119] A. Soldati, ”Influence of large-scale streamwise vortical EHD flows on wall turbulence”, *Int. J. Heat Fluid Flow*, vol. 23, pp. 441-443, 2002.

[120] A. Soldati, P. Andreussi, and S. Banerjee, “Direct simulation of turbulent particle transport in electrostatic precipitators”, *AIChE J.*, vol. 39, no. 12, pp. 1910-1919, 1993.

[121] A. Soldati, M. Casal, P. Andreussi, and S. Banerjee, "Lagrangian simulation of turbulent particle dispersion in electrostatic precipitators", *AIChE J.*, vol. 43, no. 6, pp. 1403-1413, 1997.

Curriculum Vitae

Name:	Niloofar Farnoosh
Post-secondary Education and Degrees:	Shiraz University Shiraz, Iran 1999-2003 B. Sc.
	Amirkabir University of Technology (Tehran Polytechnique) Tehran, Iran 2004-2007 M. Sc.
	The University of Western Ontario London, Ontario, Canada 2008-2011 Ph.D.
Honours and Awards:	MITACS Accelerate Fellowship London, Canada, Jul. - Oct. 2011.
	2nd prize award in Electrostatic Society of America (ESA) Conference Cleveland, USA, 2011, Charlotte, USA, 2010.
	Western Engineering Travel Grant London, Canada, 2010, 2011.

Honours and Awards (continued):	Western Engineering Graduate Entrance Scholarship (WEGES) London, Canada, 2008.

Related Work Experience	MITACS Research Intern Turbosonic Inc. Jul.-Oct. 2011.
	Research Assistant The University of Western Ontario 2008-2011.
	Teaching Assistant The University of Western Ontario 2008-2011

Publications: (Journal Papers)

[1] N. Farnoosh, K.Adamiak and G.S.P. Castle," Numerical calculations of submicron particle removal in a spike-plate electrostatic precipitator," *IEEE Trans. Dielectr. Electr. Insul*, vol. 18, no. 5, pp. 1439-1452, 2011.

[2] N. Farnoosh, K. Adamiak and G.S.P. Castle, "Three-dimensional analysis of electrohydrodynamic flow in a spiked electrode-plate electrostatic precipitator*," J. Electrostat*., vol. 69, pp. 419-428, 2011.

[3] N. Farnoosh, K. Adamiak and G.S.P. Castle, “3D numerical simulation of particle concentration effect on a single-wire ESP performance for collecting poly-dispersed particles,” *IEEE Trans. Dielectr. Electr. Insul.*, vol. 18, no. 1, pp. 211-220, 2011.

[4] N. Farnoosh, K. Adamiak and G.S.P. Castle,” 3D numerical analysis of EHD turbulent flow and mono-disperse charged particle transport and collection in a wire-plate ESP,” *J. Electrostat*., vol. 68, no. 6, pp. 513-522, 2010.

[5] N. Farnoosh, A. Shoory, R. Moini, and S. H. H. Sadeghi, “Analysis of thin-wire ground penetrating radar systems for buried target detection, using a hybrid MoM-FDTD technique,” *NDT&E International*, vol. 41, no. 4, pp. 265-272, 2008.

Publications: (Conference Papers)

[1] N. Farnoosh, K. Adamiak, G.S.P. Castle, “3D numerical study of wire-cylinder precipitator for collecting ultrafine particles from diesel exhaust,” *IEEE IAS Annual Meeting*, Orlando, FL., USA, Oct. 2011.

[2] N. Farnoosh, K. Adamiak and G.S.P. Castle, “Performance of spiked electrode-plate precipitator for collecting submicron dust particles,” *Proc. ESA Annual Meeting on Electrostatics*, Cleveland, OH, USA, Jun. 2011.

[3] N. Farnoosh, K. Adamiak and G.S.P. Castle, “3D numerical simulation of fine particle collection efficiency in cylindrical wire-plate and spiked-plate ESPs”, *12th Int. Conf. of Electrostatic Precipitation (ICESP)*, Nuremberg, Germany, May 2011.

[4] N. Farnoosh, G.S.P. Castle and K. Adamiak “A 3D simulation of a single section ESP for dust particles removal*”, IEEE 24th Canadian Conf. Electr. Comp. Eng. (CCECE2011)*, Niagara Falls, May 2011.

[5] N. Farnoosh, K. Adamiak and G.S.P. Castle, “Numerical analysis of alternatively oriented spiked-electrode electrostatic precipitator,” *Cage Club Conf. on High Voltage Engineering and Applied Electrostatics*, London, Canada, Aug. 2010.

[6] N. Farnoosh, K. Adamiak and G.S.P. Castle, "3D numerical simulation of a single-wire ESP performance," *Proc. ESA Annual Meeting on Electrostatics*, Charlotte, NC, USA, Jun. 2010.

[7] N. Farnoosh, G.S.P. Castle and K. Adamiak, "Numerical simulation of electrohydrodynamic flow and particle transport in electrostatic precipitator," *Proc. of 2nd European Seminar on Coupled Problems*, Pilsen, Czech Rep., Jun.-Jul. 2010.

[8] N. Farnoosh, K. Adamiak and G.S.P. Castle," Three dimensional modeling of electrostatic precipitators using hybrid FEM-FCT method," *Cage Club Conf. on High Voltage Engineering and Applied Electrostatics*, Hamilton, Canada, Aug. 2009.

[9] N. Farnoosh, A. Shoory, R. Moini, and S. H. H. Sadeghi, "Ground penetrating radar modeling using a hybrid MoM-FDTD technique," *Third Int. Conf. on Electromagnetic Near-Field Characterization & Imaging (ICONIC)*, St. Louis, MO, USA, Jun. 2007.

[10] N. Farnoosh, A. Shoory, R. Moini, and S. H. H. Sadeghi, "A hybrid MoM-FDTD ground penetrating radar modeling technique to detect multiple buried objects," *Proc. of the Int. Symp. on Signal Processing and its Applications (ISSPA)*, UAE, Oct. 2006.